Thermopower Modulation by Surface Interactions, and Memristive Behaviour in Self-Assembled Monolayers

Charlie Loic Wells

Physics Department

Lancaster University

A thesis submitted for the degree of

Doctor of Philosophy

May, 2026

Thermopower Modulation by Surface Interactions, and Memristive Behaviour in Self-Assembled Monolayers

Charlie Loic Wells, MPhys.

Physics Department, Lancaster University

A thesis submitted for the degree of *Doctor of Philosophy*. May, 2026.

Abstract

Molecular electronics is a versatile field, capable of tackling some of the most important and pressing issues in modern society. This thesis focusses on two main aspects: thermopower and memristive behaviour. A thermoelectric material is able to generate a voltage from a heat gradient across itself. Organic thermoelectric molecules have the potential to operate effectively at room temperature, which current inorganic thermoelectric technology cannot. Such a shift in operating temperature opens up many potential applications, with the ability to recycle waste heat into electricity from ordinary devices or even body heat.

This thesis focusses on how surface interactions and the quality of the surface can impact the potential thermopower of an organic molecule. Thermoelectric molecules have designs optimised for improved thermopower, but here it is shown that the conditions surrounding the molecule also play an important factor. Self-assembled monolayers (SAMs) are grown on gold substrates. It is shown that improved surface quality improves the consistency of the molecular junction formed, as well as a slight improvement in the conductance of the junction. This effect can be enhanced with a molecular template layer to form a multilayered structure. Here, such a film is grown with a combination of thermal evaporation and solution self-assembly. Additionally, it is shown that electrically similar molecules with extra surface contacts can dramatically change the thermoelectric properties, changing the polarity of Seebeck coefficient from negative to positive.

A memristive material is one which can reversibly switch between conductance states and retain the set state without external power. Memristive molecules act as a form of non-volatile memory and enable the possibility of new computer architectures which can greatly increase the efficiency of computing. SAMs of an edge-fused porphyrin dimer are grown onto gold substrates. 50% of the measured samples showed potential memristive effects in the form of hysteresis between the trace and retrace during current-voltage (I-V) sweeps. This effect was greatly enhanced with graphene capping the molecular films. The graphene provides a top layer which stabilises the junction and increases the quantity of molecules involved in transmission. It may also facilitate the memristive switching effect by virtue of its shallow work function.

Acknowledgements

I would like to thank my supervisors Ben Robinson and Sam Jarvis for all of the support and opportunities. They turned me from not wanting to do a PhD after my Masters into now wanting to do a Post-Doc.

I would also like to thank Alessio, Edward, Becky and Sam Harley for teaching me how to use all the equipment and bringing me up to speed so quickly in my first year. And of course the current lab group: Elisabeth, James, Richa, Cerys, Ellie, Pramita and still Sam Harley. You make the lab an enjoyable place and I appreciate all the emotional and technical support.

Thank you to my friends who, throughout undergrad and beyond, have stuck by me through all the ups and downs. Louise, Harry, Jakub, Scott, Luke, Ben, Lizzie, Alex, Amaia, G, Ell, Elo, Tom and Jason just to name a few.

Thank you to Louise, without whom this thesis would probably never have been finished. And of course thank you to my parents and grandparents for their lifetime of support and getting me this far.

Declaration

This thesis is my original work and has not been submitted, in whole or in part, for a degree at this or any other university. Nor does it contain, to the best of my knowledge and belief, any material published or written by another person, except as acknowledged in the text.

Contents

Chapter 1

Introduction

Richard Feynman's 1959 talk "There's Plenty of Room at the Bottom" speaks of a world in which atoms can be manipulated to encode information [1]. He speaks of assembling such structures by evaporation, a method to be known as molecular beam epitaxy first demonstrated in 1966 by Joyce and Bradley [2, 3], and reading such small information with advanced microscopes, the likes of which would be realised in 1981 with the invention of the scanning tunnelling microscope (STM) [4] and in 1986 with the invention of the atomic force microscope (AFM) [5]. He speaks of tiny computers, with wires of tens or hundreds of atoms in diameter. In 1974, Aviram and Ratner proposed the molecular rectifier: a single organic molecule comprised of an acceptor region, a donor region and a σ-bridge between them, which together allow the molecule to act as a diode [6]. This is considered the birth of molecular electronics and when a true bottom-up approach could be considered for the creation of electrical circuits. The projects in this thesis focus on self-assembled monolayers (SAMs) of molecules on gold electrodes. This is the messy middle ground as concepts are scaled-up from simple single molecule break-junctions before eventual implementation into devices.

Climate change is an increasingly important issue in the public eye, with a growing urgency to act. It has been reported that the total human-caused global surface temperature increase from 1900 to 2019 is 1.1 °C, and the current target is to stay under 1.5 °C. With around 79% of global greenhouse emissions coming from the energy, industry, transport and building sectors in 2019 [7], there is much room to cut down on the consumption of unsustainable energy usage. There are many possible methods of responding to the crisis, one is to develop new technologies capable of providing novel solutions. Thermoelectric materials are one such technology currently being developed. The aim is to focus on energy harvesting and recycling. A thermoelectric material is one that generates a voltage from a heat gradient across the material. This is the Seebeck effect. The idea is to use such materials to exploit the Seebeck effect to allow heat which would otherwise be wasted to

the surrounding environment to be recycled back into electricity. Bulk inorganic thermoelectric materials have been well studied since the 1950s [8], with more recent famous examples being the power source of Curiosity [9] and Perseverance [10], the latest Mars rovers. They use a SiGe alloy as a thermoelectric material to convert heat produced from a plutonium-238 radioactive source into electricity for the rover. The performance of a thermoelectric material is judged from the figure of merit, as will be discussed in Section 2.4. In order for these bulk inorganic materials to reach acceptable efficiencies, high temperatures on the order of 1000 K are typically needed [11].

Organic molecular films provide a flexible, light-weight, inexpensive, non-toxic alternative [12]. Organic molecules have an intrinsically low thermal conductance, and tunable charge transport properties from control over quantum interference effects, as is discussed in Section 2.3. This tunablility has the potential to find high Seebeck coefficients and electrical conductances at room temperature, which combined with their low thermal conductance could lead to a competitive figure of merit. There is much potential in such a flexible material operating effectively at room temperature. Waste heat could be recycled from ordinary devices such as mobile phones, for example, or body heat used to power worn devices.

The other main topic of this thesis is molecular memristors. A memristor is a material which can reversibly switch between at least two conductance states and can 'remember' the current state without external power, therefore making it a non-volatile form of memory. The details of memristors and their mechanisms are discussed in Section 2.6. In this thesis, organic molecules are investigated as potential memristors. Organic molecules here have similar advantages to their thermoelectric counterparts: their tunablility through chemical design and implementation allow for precise control over desired properties, in this case the switching speed, ON/OFF ratio and energy of operation.

One exciting application of memristive materials is implementation into a crossbar architecture in computer chips, which allow for in-memory computation. A crossbar is composed of a top set of parallel wires, known as word lines, and a bottom set of wires, known as bit lines, which are perpendicular to the top set. This forms a grid if looked at from above. The intersecting grid points are bridged with memristive materials, which can store information based off their conductive state. An arrangement like this can in principle perform vector-matrix multiplication with a single operation [13]. An incoming voltage vector is sent across the word lines, which causes current to flow through the memristive bridge sites to the bit lines where it can be measured. Each intersection has a current determined by Ohm's law, $I = GV$, and all the currents are summed along their respective bit lines. This has multiplied a vector V_{in} of size $n \times 1$ by a stored conductance matrix G of size $n \times n$ to produce an output current vector I_{out} in a single operation. Matrix-matrix multiplication therefore scales as $\mathrm{O}(n)$, as opposed to conventional digital computer which scales as $\mathrm{O}(n^3)$. 70-90% of the computational workload of common neural networks consists of matrix multiplication and accumulate (MAC) operations [14]. Crossbar architectures could therefore dramatically lower the workload and power consumption of new emerging artificial intelligence technologies. Sharma *et. al.* have already demonstrated a proof of concept [15]. They used their memristive molecules in a crossbar architecture to recreate the 'Pillars of Creation' image using data from the JWST repository. They achieved it in 26,256 operations, whereas a digital computer would require over 10^8.

Chapter 2

Background

2.1 Molecular Orbitals

Just as an atom has atomic orbitals describing the quantised energy levels of an orbiting electron, molecules can be treated as a system of interacting atomic orbitals from the constituent atoms that create quantised energy levels for the electrons within the entire molecule. These are called molecular orbitals. To illustrate this concept, consider the case of the simplest molecule, H_2. H_2 is comprised of two hydrogen atoms, each with a single proton as the nucleus and a single electron in the 1s atomic orbital of hydrogen.

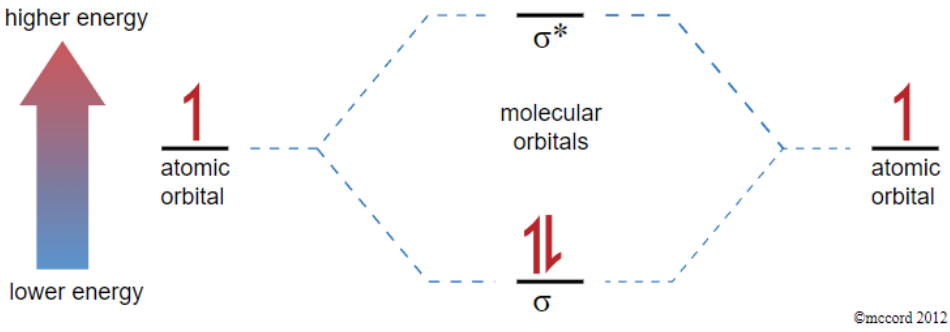

Figure 2.1: Energy level diagram showing the atomic orbitals of two hydrogen atoms, one on the left and one on the right. The half arrows represent electrons of different spin. The energy levels in the centre are the resultant molecular orbitals for a H_2 molecule. Image from [16].

In the system of two hydrogen atoms, the only parameter that can be changed to alter the energy of the system is the distance between the atoms. As this distance changes, the interaction between the atomic orbitals also changes resulting in different outcomes for the molecular orbitals. At a certain distance, the case will be such as in Figure 2.1 where one of the molecular orbitals is of a lower energy than the two separate atomic orbitals. This means it is energetically favourable for the atoms to be close together at this distance, where the electrons can be inside the molecular orbital rather than apart in their individual atomic orbitals. For the case of H_2 this happens when the atoms are at a distance of 74 pm apart [17]. This is an

example of a bonding orbital; constructive interference of the orbitals has occurred in such a way that energy would now have to be put into the system to separate the atoms, and thus a bond has formed between them. When this happens, the electron density in the overlap region increases. This is because constructive interference has occurred, so the probability of finding an electron in that region is increased.

σ-bonding is where the orbitals have overlapped end-to-end. For the case of a p-orbital for example, where two out-of-phase regions stem either side of the nucleus, a σ-bond would be created when the two in-phase regions from two p-orbitals completely overlap and constructively interfere, leaving the regions of the other phase on opposite ends of the bond [16]. In a σ-bond the electron density is always greatest in the area directly between the two nuclei. By contrast, π-bonding occurs when the orbitals stack parallel to each other. So for π-bonding of two p-orbitals, an area of the two regions of one phase would overlap, while an area of the two regions of the other phase also overlaps. In a π-bond, the electron density between the two nuclei is at a minimum, while instead the electron density at either side of the nuclei is increased. In the case of a carbon ring, six carbon atoms are bound together by a mixture of σ-bonds and π-bonds. The in-plane σ bonds are sp^2 hybrids, a combination of $2s$, $2p_x$ and $2p_y$ orbitals, to create a very strong covalent bond with an atomic separation of 142 pm [18]. This leaves the out-of-plane $2p_z$ orbitals which form a series of π-bonds around the ring. Expanding this to a 2D sheet of graphene, the π-bonding creates the idea of a delocalised sea of electrons either above or below the sheet. This is what gives graphene its extremely high metal-like in-plane conductance.

Anti-bonding orbitals occur from destructive interference between the atomic orbitals and result in a molecular orbital which has a higher energy level than the atomic orbitals, so it would be energetically favourable for the atoms to be apart and have the electrons sit in their respective atomic orbitals [19]. Anti-bonding

orbitals are denoted with a *. An example is given in Figure 2.1 where the higher molecular orbital is labelled σ^*. This tells us the orbital is created by destructive interference from the σ configuration and has a higher energy than the constituent atomic orbitals.

When dealing with a larger molecule, the number of molecular orbitals increases significantly. These molecular orbitals are filled from the electrons of the constituent atoms, starting from the lowest energy level and increasing. This leads to the concept of the two most chemically relevant molecular orbitals, the highest occupied molecular orbital (HOMO) and the lowest unoccupied molecular orbital (LUMO). The Fermi level corresponds to to a state which has a probability to be occupied of 0.5 [20], and is therefore in the HOMO-LUMO gap. The energies of the HOMO and LUMO are those at which electrons are most likely to exit or enter the molecule. The HOMO contains the highest energy electrons that can be donated and the LUMO represents the lowest energy state that electrons can be accepted.

If there is an electrode-molecule interface in equilibrium, the chemical potential of the molecule will align with the Fermi level of the electrode relative to vacuum. In initial contact, the molecule will accept or donate electrons, which shifts the HOMO and LUMO, as well as the chemical potential [21]. As this happens, an interface dipole is formed [22], creating a local electric field and shifting the vacuum level. This changes the effective work function of the electrode at the interface, further contributing to the alignment of the molecule chemical potential and electrode Fermi level [23]. If a potential difference, V, is applied then the work function and energy levels will change by an amount eV [24]. If this occurs such that the Fermi energy of the electrode is now higher than the LUMO, a current will flow with electrons at the electrode Fermi level moving to occupy the unoccupied states in the molecule at a lower energy. Conversely, if the electrode Fermi level drops below the HOMO, a current will flow in the opposite direction with electrons leaving the molecule

to occupy a lower energy state within the electrode. This is known as resonance transport and is discussed further in section 2.2. Resonance transport is useful for imaging molecules using STM methods as selecting the correct bias voltage to coincide with the HOMO or LUMO energies will maximise current flow and improve the image quality.

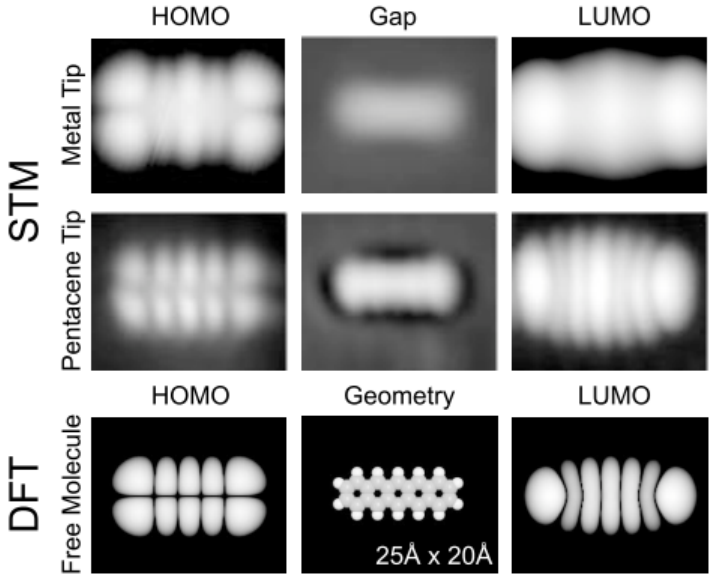

Figure 2.2: STM images showing the HOMO and LUMO patterns over a pentacene molecule. The image quality is greatly improved by picking up a pentacene molecule with the STM tip. The density functional theory (DFT) simulations for the HOMO and LUMO of pentacene are also shown for comparison. Image from [25].

The interference effect that creates molecular orbitals results in an interference pattern of the electron probability density over the molecule for individual molecular orbitals. These can be predicted using density-functional theory (DFT) simulations. STM has since been able to confirm these simulations by managing to image the molecular orbitals. For example, Repp *et al* [25] electrically decoupled pentacene molecules from a copper substrate using two layers of NaCl. Because of this, the molecular orbitals of the pentacene were not entangled with the copper substrate,

and since electrons could still tunnel through the thin NaCl layer, STM imaging could still be used. By adjusting the STM bias below the energy level of the HOMO and above the energy levels of the LUMO, the molecular orbital patterns of each were imaged as shown in Figure 2.2. The use of a functionalised probe by picking up a pentacene further increased image quality. The images show a clear agreement with the DFT simulations.

2.2 Electron Transport Through Single Molecular Junctions

A molecular junction consists of two electrodes, a source and a drain, connected by a molecule. An electron of energy, E, in the source electrode has a certain transmission probability, $T(E)$, to pass through the molecule to the drain electrode. This probability depends on the energy of the electron and the molecular orbitals of the molecule. An electron can be described as a De Broglie wave function, and when an electron enters the molecule through a certain atom, this wave function interacts with the molecular orbitals and forms a standing wave within the molecule. This creates anti-nodes and nodes through the molecule at points of constructive and destructive interference respectively [26, 27]. Molecular design can shift around the positions of the nodes and anti-nodes with the aim of altering its properties. For example, an anti-node on the exit point of the molecule to the drain electrode corresponds to a large transmission probability, $T(E_F)$, and hence greater conductance, σ, via the Landauer formula,

$$\sigma = G_0 T(E_F) \tag{2.1}$$

where the conductance quantum, $G_0 = 7.75 \times 10^{-5}\,\mathrm{S}$. This is derived in Section 2.4. The transmission probability is described as a function of energy of the electron. There are resonances when the electron energy coincides with the energy levels of the molecular orbitals. Resonant transport takes place on such a resonance as long

as there are large gaps in energy between molecular orbitals. Here, the transport probability can be given by the Breit-Wigner formula [28],

$$T(E) = \frac{\Gamma^2}{(E-\epsilon)^2 + \Gamma^2} \tag{2.2}$$

where Γ and ϵ are the full-width half-maximum and the central energy of the resonance peak respectively.

In practice, when a molecule is placed in between two electrodes, the molecular orbitals will adjust such that the Fermi energy of the electrode lies between the highest occupied molecular orbital (HOMO) and the lowest unoccupied molecular orbital (LUMO). This renders Equation 2.2 invalid for this case as the energy level spacing is no longer large with respect to the distance from a resonance to the Fermi level of the electrode. Electrons therefore undergo off-resonance transport through a molecular junction, where adjustments have to be made to Equation 2.2 to account for the influence of the other molecular orbitals.

2.3 Off-Resonance Transport

To properly represent the impact of multiple molecular orbitals on the transmission probability, the Breit-Wigner formula given in Equation 2.2 should be presented in the form

$$T(E) = c|g|^2 \tag{2.3}$$

where c is a constant determined by the contact strength to the electrodes and g is given by

$$g = \frac{A}{(E-\epsilon) + \mathrm{i}\Gamma} \tag{2.4}$$

where $\Gamma = cA^2$ and A represents the amplitude of the resonance at the contact points to the electrodes [29]. Additional resonances are accounted for additively

within the modulus of Equation 2.3. For example, a two-level system containing only a HOMO and a LUMO resonance would be expressed as

$$T(E) = c|g_{\mathrm{H}} + g_{\mathrm{L}}|^2 = c(|g_{\mathrm{H}}|^2 + |g_{\mathrm{L}}|^2 + g_{\mathrm{H}}g_{\mathrm{L}}^* + g_{\mathrm{H}}^* g_{\mathrm{L}}) \tag{2.5}$$

where g_{H} and g_{L} are the contributions of the HOMO and LUMO respectively. The terms $g_{\mathrm{H}}g_{\mathrm{L}}^*$ and $g_{\mathrm{H}}^* g_{\mathrm{L}}$ are of particular importance as they can be negative, implying the possibility of destructive interference between the HOMO and LUMO molecular orbitals which can create points on the molecule where the transmission probability falls to zero.

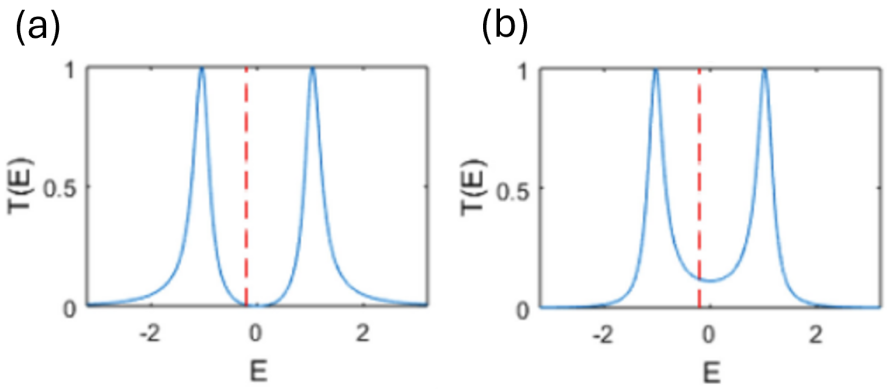

Figure 2.3: Examples of transmission probability distributions showing the HOMO-LUMO resonances. In each case the HOMO resonance is the left peak and the LUMO resonance is the right peak. The Fermi energy of the electrodes fall between the resonances shown by the dotted red line. Figure from [29].

Examples of what a transmission probability distribution might look like for a molecule with only two molecular orbitals are shown in Figure 2.3. Example (a) is being affected by destructive quantum interference from the interaction between the HOMO and LUMO cancelling out. This can be seen by the transmission probability reaching zero in the gap between the molecular orbitals. In contrast, example (b) undergoes constructive quantum interference and is always positive in the HOMO-LUMO gap.

In practice, molecules are more complicated as they have many more than just two molecular orbitals. Resonances will occur at the HOMO-1, HOMO-2, and so on, with the same for the LUMO side. Each of these molecular orbitals can contribute to the quantum interference effect and have a non-negligible impact on the result, regardless of how far that molecular orbital is from the electrode Fermi energy. This is where Green's functions are needed. All the molecular orbitals are taken into account to build a map of the quantum interference over the molecule. The amplitude of the Green's function at any point is proportional to the transmission probability of an electron tunnelling to that point from a given entry point. This is essentially a visualisation of the standing wave formed from the electron De Broglie wave function described at the start of Section 2.2. If the amplitude of the Green's function is large at the exit point of the molecule, an electron at a given entry point has a large probability of tunnelling through the molecule and therefore the transmission probability is high [29].

This is visualised in Figure 2.4 which shows the amplitude of the Green's function throughout two example molecules (anthracene and anthraquinone), given an entry point at atom j. For the example of exit at atom i, anthracene exhibits constructive quantum interference as there remains a sizeable amplitude of the wave function at that atom, represented by the purple coloured area. The addition of the two oxygen atoms in the anthraquinone, however, causes destructive quantum interference, as the different amplitude phases have cancelled out at atom i.

Markussen *et. al.* give an insight into how molecular design can influence and be used to predict whether constructive or destructive interference will occur within a given molecule [30]. Their graphical method involves tracing a single non-self-intersecting line along a conjugated π network between connected electrodes and counting the atoms which cannot be connected. These remaining atoms are paired

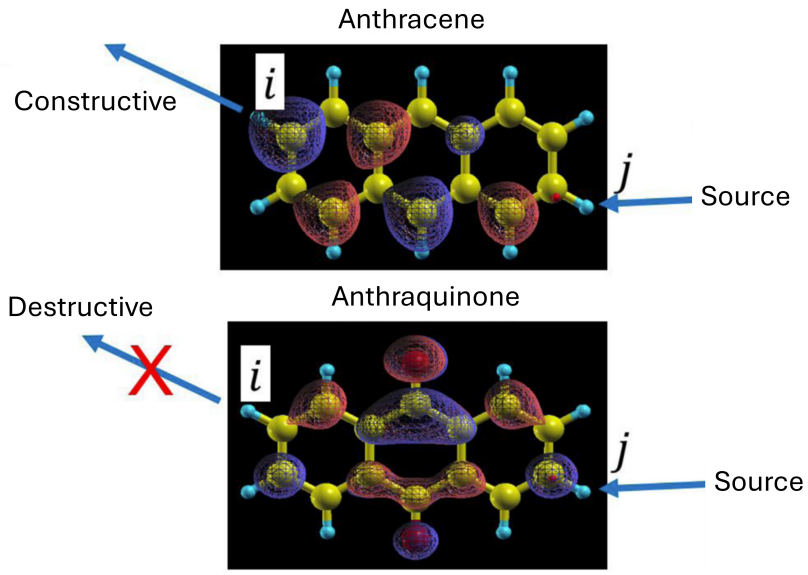

Figure 2.4: Greens function visualisation for an anthracene and anthraquinone molecule for an electron entering at atom j. Larger coloured areas around atoms represent a greater probability of electron transmission to that area on the molecule. The red and purple colours represent a positive and negative amplitudes of the wave function respectively. Image from [29].

up, and if there are any lone atoms remaining, destructive interference can occur. An example of the graphical method being applied to benzene in three different connection configurations is given in Figure 2.5.

The outcomes of these connectivities on benzene are well known [31] so can be used as a good illustration of the graphical method. In Figure 2.5, all of the atoms can be connected by the red line in the ortho configuration. The para configuration leaves two atoms, which can be paired, shown by the red circle. Constructive interference is therefore predicted to occur in these two configurations, as any alternate paths the electrons could take are in-phase. The meta configuration has a lone atom remaining, shown by the green dot. This represents an out-of-phase path which can destructively interfere at a connection and cause an anti-resonance. These are known as Mach-Zehnder resonances. Molecular design can therefore be used as a powerful tool to manipulate quantum interference effects for a desired

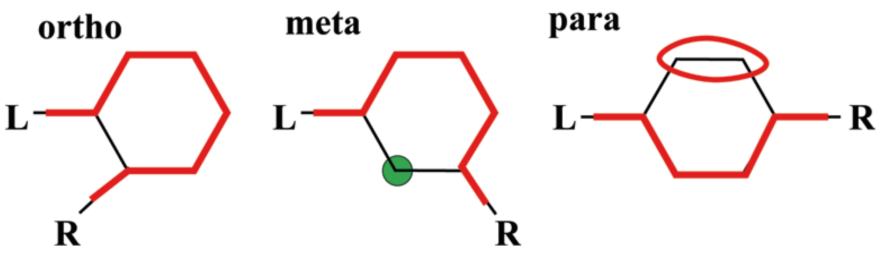

Figure 2.5: Applying the graphical method to benzene with ortho, meta and para connectivities. The red line joins the left and right connections, leaving either no atoms (ortho), one atom (meta) or two atoms (para) unconnected. Image from [30].

effect, be it to boost conductance or create anti-resonances useful for thermoelectric properties. This is discussed further in Section 2.5.

2.4 Molecular Thermoelectricity

Consider a molecular junction where the electrodes are held at different temperatures. The thermoelectric response is determined by the energy dependence of the transmission function close to the Fermi energy. The energy distribution of electrons in the hot electrode is broadened. If the junction is LUMO dominated, higher energy electrons transmit more efficiently through the molecule than the lower energy electrons in the cold electrode, since they lie closer to a resonance. In a HOMO dominated junction the transmission direction is reversed, instead with hole dominated transport. These both result in a build-up of charge and therefore a potential difference [32, 33]. This describes the Seebeck effect and is quantified by the Seebeck coefficient,

$$S = -\left(\frac{\Delta V}{\Delta T}\right)_{I=0} \tag{2.6}$$

where ΔV is the open circuit voltage generated by the temperature difference, ΔT, between the two electrodes. To consider the impact on the chemical potentials of the electrodes, consider the steady state situation where the current flow, J, is zero.

As the temperature of one electrode is raised, a current will form as electrons travel from the hot reservoir to the cold. For the overall current flow to be zero, a counter current is formed from the chemical potential in the cold reservoir being higher than that of the hot reservoir [34]. This leads to the expression for chemical potential in terms of the Seebeck coefficient and temperature difference [35].

$$\Delta\mu = |e|S\Delta T \tag{2.7}$$

The main conclusion from this equation is that for a negative Seebeck coefficient and electrons moving from a hot to cold reservoir, electrons are being transported from a lower chemical potential to a higher chemical potential. The efficiency of a thermoelectric material, in this case the molecule between the two electrodes, is therefore given by the work done against the potential difference per unit time divided by the heat extracted from the hot reservoir per unit time. The work done against the chemical potential difference is given by $J\Delta\mu$. Since μ can be written as eV, the work done can be expressed as $-I\Delta V$. The thermoelectric efficiency can therefore be written as

$$\eta = \frac{-I\Delta V}{\dot{Q}} \tag{2.8}$$

where $\dot{Q}$ is the rate of heat extracted from the hot reservoir [29]. To understand how the efficiency depends on the properties of the thermoelectric material, I and Q should be related to the electrical conductance, G, and the Seebeck coefficient, S, of the material.

In the linear response regime, I and Q are related to ΔV and ΔT by [29]

$$\begin{pmatrix} I \\ Q \end{pmatrix} = \frac{2}{h} \begin{pmatrix} e^2 L_0 & -\frac{|e|}{T} L_1 \\ -|e| L_1 & L_2 \end{pmatrix} \begin{pmatrix} \Delta V \\ \Delta T \end{pmatrix} \tag{2.9}$$

where

$$L_n = \int_{-\infty}^{\infty} (E - E_F)^n T(E) \left(-\frac{\partial f(E,T)}{\partial E} \right) dE \tag{2.10}$$

give the iterations of L_0, L_1 and L_2, $T(E)$ is the transmission probability, E_F and T are the average Fermi energy and the average temperatures between the two

reservoirs respectively, and $f(E,T) = \left[e^{\frac{E-E_F}{k_B T}} + 1\right]^{-1}$ [36, 37]. Now the properties of G and S can be introduced. The electrical conductance is defined as $G = \frac{I}{\Delta V}$ at $\Delta T = 0$ and the Seebeck coefficient is defined as $S = -\frac{\Delta V}{\Delta T}$ at $I = 0$. Using the Equations 2.9, the electrical conductance can be written as

$$G = \frac{2e^2}{h} L_0 \tag{2.11}$$

and the Seebeck coefficient can be written as [38, 39]

$$S = -\frac{L_1}{|e| T L_0} \tag{2.12}$$

Using these forms, the matrices in Equation 2.9 can be written in terms of G and S. By including an expression for the thermal conductance too, where the thermal conductance due to electrons is given by

$$\kappa_e = \frac{2}{h}\left(L_2 - \frac{L_1^2}{T L_0}\right) \tag{2.13}$$

the equation becomes

$$\begin{pmatrix} I \\ Q \end{pmatrix} = \begin{pmatrix} G & GS \\ GST & \kappa + GS^2T \end{pmatrix} \begin{pmatrix} \Delta V \\ \Delta T \end{pmatrix} \tag{2.14}$$

where κ is the addition of the thermal conductance due to electrons and the thermal conductance due to phonons [40]. Now the efficiency in Equation 2.8 can be rewritten in terms of G, S and κ to give

$$\eta = \frac{-\Delta V(G\Delta V + GS\Delta T)}{GST\Delta V + (\kappa + GS^2T)\Delta T} \tag{2.15}$$

The higher the thermoelectric efficiency of a sample, the better that sample will be at converting heat from a source to electricity, and therefore a more promising thermoelectric material for practical use. In order to know which material properties are of importance, Equation 2.15 should be differentiated with respect to ΔV and set to zero to find the maximum efficiency. This results in the expression for maximum efficiency [41, 42]

$$\eta_{max} = \frac{\Delta T}{T} \frac{\sqrt{1+ZT} - 1}{\sqrt{1+ZT} + 1} \tag{2.16}$$

where

$$ZT = \frac{GS^2T}{\kappa} \tag{2.17}$$

ZT is known as the figure of merit. Maximising ZT corresponds to a higher maximum efficiency and therefore a better thermoelectric material for practical use. When researching thermoelectric materials, from Equation 2.17 it can be seen that the electrical conductance and the Seebeck coefficient should be maximised, with the Seebeck coefficient having a greater impact. Also the thermal conductance, due to both phonons and electrons, should be minimised.

Finally, now the important properties have been identified, they can be related back to the transmission probability via Equation 2.10. In the low temperature limit where $T(E)$ varies on the scale of k_BT and linearly with E, Equation 2.10 yields the results of $L_0 \approx T(E_F)$, $L_1 \approx (eT)^2\alpha \left(\frac{dT(E)}{dE}\right)_{E=E_F}$, and $L_2 \approx (eT)^2\alpha T(E_F)$, where $\alpha = 2.44 \times 10^{-8}\,\mathrm{W\Omega K^{-2}}$ is the Lorentz number. Using Equation 2.11 results in the Landauer formula

$$G(E_F) \approx G_0 T(E_F) \tag{2.18}$$

where $G_0 = \frac{2e^2}{h} = 7.75 \times 10^{-5}$ S is the conductance quantum [43,44]. This shows the electrical conductance is proportional to the transmission probability at the Fermi level. Equation 2.12 results in the Mott formula

$$S(E_F) \approx -\alpha|e|T \left(\frac{d\,lnT(E)}{dE}\right)_{E=E_F} \tag{2.19}$$

which shows the Seebeck coefficient is proportional to the rate of change of the transmission probability at the Fermi energy [45, 46]. Equation 2.13 results in the Wiedemann-Franz law

$$\kappa_e \approx \alpha T G \tag{2.20}$$

which shows that the thermal conductance due to electrons is proportional to the electrical conductance [47, 48]. This presents a conflict in Equation 2.17 where in order to improve ZT, G should be maximised and κ_e should be minimised. However as Equation 2.20 shows, the two are proportional. The thermal conductance due to

phonons should therefore be focussed on and minimised instead. There is an inherent mismatch between the discrete vibrational modes of a molecule to pass phonons and those of a metallic electrode [32], but design of the molecular junction can further limit these modes, greatly restricting the thermal conductance due to phonons. This can be done with choice of anchor group [49], choice of metallic electrodes [50] or the addition of pendant groups which can restrict vibrational modes [51] or induce destructive interference effects [52,53]. Alternatively, a molecule with a particularly large conductance would also make κ_e large via Equation 2.20. This would render κ_p insignificant, so $\kappa \approx \kappa_e$, therefore minimising the denominator of Equation 2.17 with respect to the numerator [54].

2.5 Resonance Manipulation to Boost ZT

Now the key parameters affecting the figure of merit are properly defined, a more detailed discussion about the types of resonances and how they can be used to increase ZT can be had. The Seebeck coefficient is the most impactful parameter on the overall figure of merit, from equation 2.17. In order to boost the Seebeck coefficient of a molecule, quantum interference effects can be exploited. From equation 2.19, the Seebeck coefficient is proportional to the gradient of the transmission curve at the Fermi energy. Manipulating quantum interference effects to create large gradients at the Fermi energy is the key to unlocking high Seebeck coefficients in molecules. This is typically done by creating or exploiting resonances or anti-resonances, points at which the transmission curve spikes or crashes rapidly, causing a sharp gradient around it.

2.5.1 Breit-Wigner Resonances

As previously discussed, a Breit-Wigner resonance occurs from the De Broglie wave function interacting with the molecular orbitals and forms a standing wave across the molecule, giving rise to the HOMO and LUMO. The simplest case of a Breit-

Wigner resonance is given in equation 2.2, where the resonances are far apart so do not interact with the transmission at a given energy. However, as previously discussed, this is not realistic for a molecular junction where a more complex series of terms is required, which can then be collapsed into Green's functions. The Fermi energy typically lies in the HOMO-LUMO gap in a molecular junction, limiting the transport through the resonances. This does not, however, mean these resonances cannot be exploited. Mechanical gating can be used to change the molecule-electrode bonds by physically stretching or compressing the molecule by precise control of one of the electrodes. This alters the coupling to the electrode by changing bonding angle and separation of the molecule-electrode interface, or changing the geometry of the molecule, both of which can shift the positions of the HOMO and LUMO [55, 56]. This allows the resonances to be tuned to positions where the Fermi energy may rest closer to the peak, boosting the conductance and Seebeck coefficient.

2.5.2 Mach-Zehnder Resonances

Mach-Zehnder resonances were previously discussed in Section 2.3. These describe resonances and anti-resonances formed from coherent waves from different paths interacting with either constructive or destructive interference. The simplest example of this is a Benzene connected in ortho, para and meta configurations as shown in Figure 2.5, where the meta configuration exhibits destructive interference. This can be quickly spotted from the graphical method where a single atom is left after connecting the two leads [30]. Delving into how this works, consider the 1D dispersion relation for the tight-binding model

$$E = \epsilon_0 - 2\gamma \cos(k) \tag{2.21}$$

where k is wave vector, γ is the hopping element and ϵ_0 is the on-site energy [57]. The hopping element describes the coupling between neighbouring atomic sites and the on-site energy is the band centre energy. This means that for a 1D chain, electrons can occupy energies in a continuous distribution from $\epsilon_0 - 2\gamma$ to $\epsilon_0 + 2\gamma$.

Rearranging Equation 2.21 for k gives

$$k(E) = \cos^{-1}\left(\frac{\epsilon_0 - E}{2\gamma}\right) \tag{2.22}$$

which can be used to find the phase difference between multiple paths. At the centre of the HOMO-LUMO gap, $E = \epsilon_0$ which gives $k = \frac{\pi}{2}$ from 2.22. Now, the transmission probability $T(E)$ is related to the difference in lengths between two paths as

$$T(E) \propto |t(E)|^2 = |1 + e^{ikL}|^2 \tag{2.23}$$

where $t(E)$ is the transmission amplitude and L is the difference in length between the two paths from counting the number of atoms [58]. This is realised by normalising one path and adding to the relative phase of the other for the total transmission amplitude of the combination. In the case of the para configuration, the lengths of the possible paths are equivalent, giving $e^{ik0} = 1$, so the paths undergo constructive interference. For the meta configuration, the difference in length is two atoms, giving $e^{i2k} = e^{i\pi} = -1$. Destructive interference therefore occurs, causing an anti-resonance at the centre energy of the HOMO-LUMO gap. Figure 2.6 shows an example of two molecules exhibiting Mach-Zehnder anti-resonances. The tight-binding model (red dashed line) shows an exact symmetrical and central anti-resonance, since tight-binding approximations were used to give Equation 2.23. However, similar trends are also reproduced with the DFT calculations, supporting the graphical method suggested by Markussen et. al. [30].

2.5.3 Fano Resonances

The third type is a Fano resonance. This is a very sharp resonance and anti-resonance which can be within the HOMO-LUMO gap. Fano resonances occur from a bound state being coupled to a continuum of states. This can be achieved in a molecule by the inclusion of a pendant group coupled to the backbone of the molecule. Since the molecule is connected to a metallic electrode there is a continuum of states through the backbone, whereas the pendant group will have a

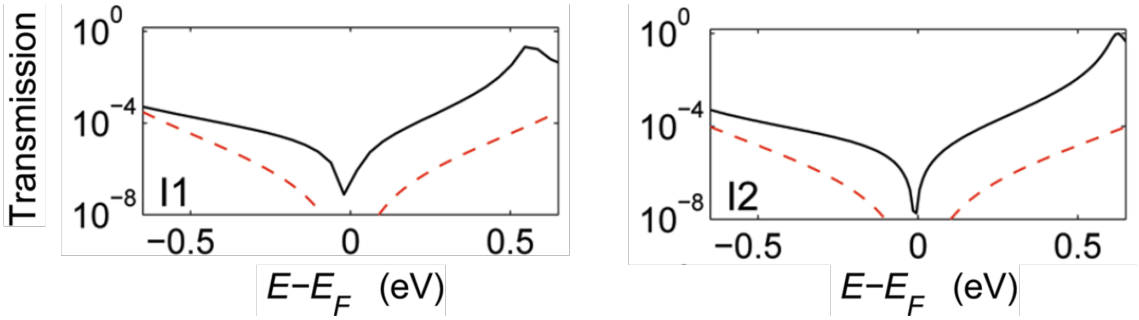

Figure 2.6: Example of a Mach-Zehnder resonances. The red dashed lines are the results using the tight-binding model. The black lines are from first principles DFT transport calculations using thiol anchors on Au(111). Images from [30].

bound orbital of energy ϵ_p [59]. This alters the Breit-Wigner formula in Equation 2.2 to account for the additional bound state of the pendant group

$$T(E) = \frac{\Gamma^2}{\left(E - \epsilon_n - \frac{\alpha^2}{(E-\epsilon_p)}\right)^2 + \Gamma^2} \tag{2.24}$$

where ϵ_n is the centre energy of the Breit-Wigner resonance and α is the hopping matrix representing the coupling between the pendant and the backbone [58, 60]. From Equation 2.24 it can be seen that the transmission is destroyed as the energy coincides with the pendant orbital energy, $E = \epsilon_p$. This is the Fano anti-resonance. However, an additional resonance is also formed. From Equation 2.24, there is a maximum at $(E - \epsilon_n)(E - \epsilon_p) - \alpha^2 = 0$. This is a quadratic equation with two solutions. There is a solution close to $E \approx \epsilon_n$ which relates to the Breit-Wigner resonance, and another solution close to $E \approx \epsilon_p$ is the Fano resonance, which is always next to the Fano anti-resonance. This leads to a very distinctive shape that can be seen in Figure 2.7.

Fano resonances are unique because they are independent of the electrode coupling, since the pendant orbital energy is the only influencing factor. Also, as a result of the very particular energy the anti-resonance occurs at, they are especially sharp. If a Fano resonance coincides with the Fermi energy, it would therefore result in a huge boost in the Seebeck coefficient from the particularly large gradient of the transmission function at that point [61].

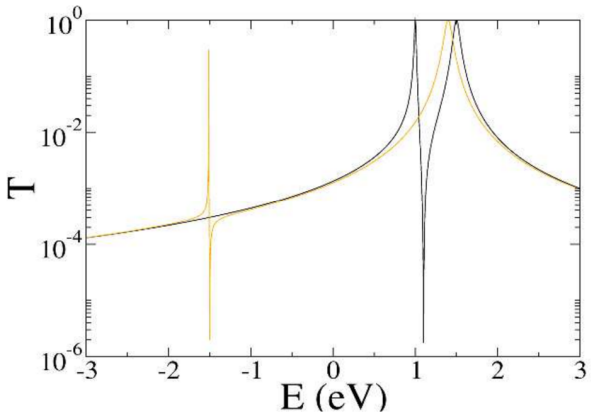

Figure 2.7: Example of a Fano resonance and the characteristic pair of resonance and anti-resonance. The Breit-Wigner resonance is set to $\epsilon_n = 1.5$eV. The pendant orbital energies are set to $\epsilon_p = -1.5$eV (yellow) and $\epsilon_p = 0.9$eV (black). Image from [58].

2.6 Memristive Behaviour

A molecule exhibits memristive behaviour if it can reversibly switch between two conductance states. This can occur by adjusting an external electric field to trigger a switching effect. The new conductance state must then be retained without any external power, be able to be read in a non-destructive manner, and be able to revert back to the original conductance state [62]. This lets a memristive molecule act as non-volatile memory. This memory can be read, erased and rewritten, as opposed to write-once read-many times (WORM) memory [63] like a CD. Current non-volatile memory uses a metal-oxide-semiconductor field-effect transistor (MOSFET) with a floating gate which can hold charge without external power [64]. This is how a USB drive would store data. All of these use top-down fabrication, which is reaching its limit on how small a reliable device can feasibly be made. This is where organic molecules have an advantage with bottom-up assembly. For a memristor to be used in an effective high performance memory device, it needs to exhibit a fast switching speed and a high ON/OFF ratio. The ON/OFF ratio is the ratio between the molecule's high conductance (ON) state and low conductance (OFF) state. In

addition, it should have a competitive efficiency, governed by the memristive figure of merit: number of tera-operations per second per Watt (TOPS/W) [65]. Expressing in terms of energy ϵ and time t gives

$$\frac{\text{OPS}}{\text{W}} = \frac{1/t}{\epsilon/t} = \frac{1}{\epsilon} = \text{OPE} \tag{2.25}$$

where OPE is operations per unit energy [66]. The TOPS/W of a memristor is therefore independent of time and power. Commonly used CMOS chips are of the range 10-20 TOPS/W [65], but devices far exceeding that are currently being developed. For example, Soliman et. al. quote 885.4 TOPS/W for their ferroelectric field-effect transistor (FeFET) [67], and IMEC demonstrated a chip that could perform up to 2900 TOPS/W [68]. There are few reported TOPS/W for devices containing organic memristors to compare to, however, Goswami et. al. do calculate switching energies for changes in redox states in their device. There are multiple available redox states which can be switched between in the molecules, and they quote 30fJ for a (11) state to change to a (00) state, and 0.2fJ for a (31) to (11) change [69]. Using these in Equation 2.25 gives 33 TOPS/W for a 30fJ switch and 5000 TOPS/W for a 0.2fJ switch. This shows TOPS/W values competitive or even surpassing the current best inorganic devices. Switch speeds of $<$ 5ns have also been reported for these organic memristors, with no signs of deterioration after 10^{10} cycles [70].

Results of Goswami et.al show an example of how memristive behaviour can look in a molecule. In their 2021 paper "Decision trees within a molecular memristor" [71] they use an [Fe(L^-)L2](PF6) complex, where L = 2-(phenylazo)pyridine. These are three 2-(phenylazo)pyridine ligands coordinated to an iron metal centre. The hexafluorophosphate is a counterion which balances charge throughout the molecule. In their bias sweeps, they find five different molecular redox states, producing an unusual but highly reproducible I-V plot that can be seen in Figure 2.8.

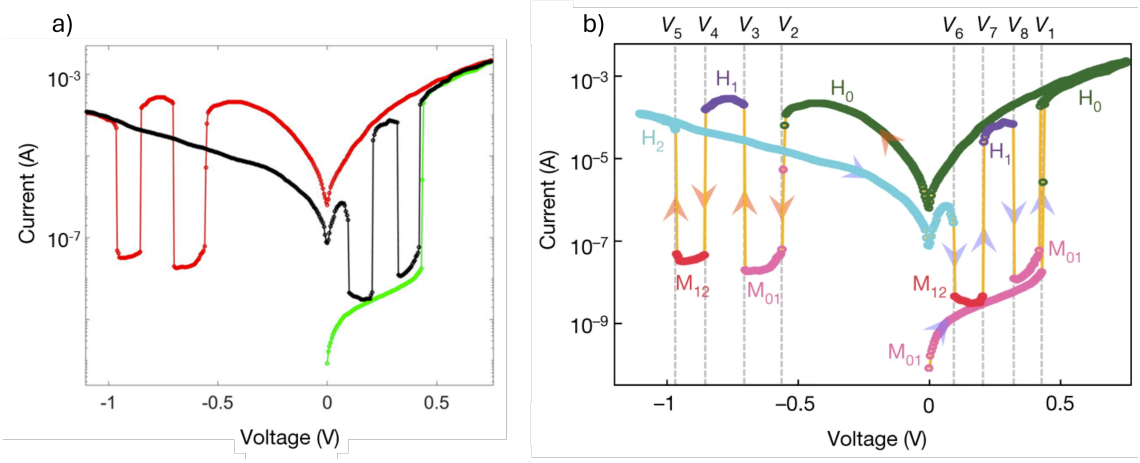

Figure 2.8: Example IV traces produced from the works of Goswami et.al. a) shows a simple colour coded look at how the IV trace is formed. The bias sweep starts at 0 on the green line, the reverse sweep follows the red line, and then the forward sweep follows the black line. b) shows the same but with colour coded redox states. Each segment is broken up and assigned a redox state which are determined from in situ Raman spectra. Image from [71].

Of note, the current values are taken on a logarithmic scale. Therefore the absolute values of current are used, hence the current always appears positive. The assignments of the redox states are based on the reduction of the ligands. H_0, H_1 and H_2 are where all three ligands homogenously have their LUMO's unoccupied, singly occupied and doubly occupied respectively. M_{01} and M_{12} are a mixture of ligands being unoccupied and singly occupied, and singly and doubly occupied respectively. The H redox states are the high conductance (ON) states, and the M redox states are the low conductance (OFF) states, with 4 orders of magnitude between them as can be seen in Figure 2.8.

There are multiple mechanisms by which an organic molecule can be designed to switch, the redox state manipulation demonstrated in the Goswami et.al. example being one of them. The following subsections will outline common mechanisms being used in current molecular memristive systems, and how they are able to change the

conductance state of an molecule.

2.6.1 Redox Reaction

Including redox active elements in a molecular complex is a method of holding non-volatile memory. Provided the redox states are stable so information is not lost, a redox reaction can be induced by an external electric field, by which an electron is either added to an acceptor (reduction) or subtracted from a donor (oxidation). In the Goswami et. al. example, the ligands surrounding the iron centre were the redox active components, rather than the iron itself. This allowed even more conductance states to be available as different combination of redox reactions occurred at different bias voltages. Other designs have been shown to work just using iron (or other metals) as the redox active component [72], or combining multiple redox active sites together to unlock a huge range of potential stable conductance states. Zhang et. al. combined trinuclear copper and triphenylamine, two distinct redox active sites which had a synergistic effect that reduced the redox barrier to switch between the states of both. This is likely from electrons being shared between the sites in a covalent organic network, which aided the electrons entering or exiting either individual redox site [73]. The result of this was 128 distinct and stable conductance sites which could be observed with negative voltage pulses.

Redox active molecules tend to have frontier orbitals close in energy to the Fermi levels of typical electrode choices like gold or platinum [74]. When a redox reaction takes place, these frontier orbitals can shift dramatically, which can drastically change the conductance of the molecular junction. Since the Fermi energy begins near-resonance, shifts in the resonances produce an amplified conductance change. As redox reactions take place, the mechanism for electron transport can change too, depending on the molecule-electrode coupling. If the coupling is strong, charge carriers interact weakly with the molecule, treating it like a potential barrier and the usual coherent transport, which has been previously described, occurs. If the

coupling is weak and a localised redox state is formed, then incoherent transport can increase. This is where Marcus hopping occurs, and electrons individually occupy the localised state before passing through [75]. As the electron localises, reorganisation occurs, the molecule relaxes and geometry shifts to accommodate. This destroys the quantum phase of the electron, and is therefore incoherent transport. The electron then moves on and the localised state becomes occupied by the next electron. This process is much slower than coherent transport so the conductance is greatly reduced.

However, Marcus hopping can also increase conductance. Take an example where a molecule starts with poor conductance, if the Fermi energy begins far from a HOMO or LUMO resonance or the molecule is particularly long, such that it is hindered by the exponential decay with length in the coherent tunnelling regime

$$G \propto e^{-\beta L} \tag{2.26}$$

where L is length and β is a molecule dependant tunnelling decay constant [76, 77]. Now, if a localised redox orbital is present close to the Fermi energy, this will facilitate transmission since the small energy transmission to the localised orbital is much easier than bridging the entire HOMO-LUMO gap. Marcus hopping dominates, and despite the slower process, less energy is required and a higher conductance is achieved compared to the initial poor tunnelling [78]. The stability of the redox states, and the dramatic shifts in conductance they can cause, makes redox active molecules a good candidate for memristive devices.

2.6.2 Charge Transfer

Unlike redox reactions losing and gaining electrons to and from external sources, charge transfer is where the electron distribution shifts within the molecule or molecular system. This is done using a donor-acceptor combination, where either a molecule is created with donor-acceptor components [79] or a covalent organic

framework is created using a mixture of donor and acceptor molecules [80]. With the application of an electric field, the charge distribution will shift as electrons move from the donors to the acceptors. This creates D^+A^- pairs which aid in stabilising the excited state with Coulomb interactions. As the pairs are formed, an internal dipole is created from the localised charge. This shifts the molecular orbital energies [81], in a similar way to how an external field would. Shifting the frontier orbitals closer or further from the Fermi energy of the electrodes is what changes the conductance, and is the dominant mechanism by which the conductance changes in a charge transfer system. In addition to this, the molecule relaxes around the new charge distribution with minor reorganisation, much smaller than what would be seen in a redox reaction. This does, however, still create a polaron, a localised electronic state that accompanies the lattice relaxation. This can be used as a hopping site in a similar way to previously discussed with Marcus hopping through a redox site, it can increase conductance if the localised state appears close to the Fermi energy, or decrease it if there is a strong localisation and slow hopping dominates [82].

The excited state remains stable, even after the external field is removed. This is due to a combination of the attraction between D^+ and A^-caused by Coulomb interaction, lowering the energy of the charge transfer state, and Marcus inverted region effect which slows the back transfer [83]. The Marcus inverted region effect is counter-intuitive, and causes a reaction rate to reduce the greater the driving force behind it. Take the thermodynamic driving force, ΔG^0, to be

$$\Delta G^0 = G_{\text{final}} - G_{\text{initial}} \tag{2.27}$$

where G_{final} is the Gibbs free energy of the final excited charge transfer state and G_{initial} is the Gibbs free energy of the initial charge distribution state. Marcus regions are dependant on how ΔG^0 relates to the reorganisation energy, λ. The Marcus normal region occurs when $-\lambda < \Delta G^0 < 0$, and the rate of reaction increases with the driving force (as ΔG^0 gets more negative). Once $\Delta G^0 < -\lambda$, the Marcus

inverted region occurs and now the reaction rate slows as the magnitude of ΔG^0 gets larger [84]. Since in charge transfer mechanisms the reorganisation is small, λ is small, ΔG^0 therefore passes $-\lambda$ easier. In addition, the energy of the final state is lowered from the Coulomb interaction as the D^+A^- pairs are formed, lowering G_{final}, further increasing ΔG^0 and therefore slowing the back transfer of electrons, maintaining the charge transfer state for longer, even without an external field.

The charge transfer process can be reversed with the application of an electric field in the opposite direction. The charge transfer process is very fast, much faster than redox switching since far less reorganisation occurs. It also has a low activation energy, so devices can use low switching energies to operate and the possibility of very high switching rates [85]. The trade off is that since the reorganisation is small, the orbital energy shifts are not as large as in a redox reaction, creating less dramatic conductance changes. Charge transfer memristors therefore tend to have lower ON/OFF ratios, typically on the order of 10^2 to 10^3 [86, 87], as opposed to 10^4 or higher in redox memristors [71].

2.6.3 Charge Trapping

Charge traps are localised energy states that can hold electrons for an extended period of time. These often arise from defects such as variations from molecular structure defects or molecular packing irregularities, but can also be intentionally created from molecular design by introducing predictable trap sites with donors and acceptors [88]. When an external electric field is applied, these trap sites are filled, and remain filled after the external power is removed. Electrons can then be de-trapped with the application of an opposite electric field. The conductance is heavily influenced by whether the trap states are filled or not. A molecule may be using the trap states as intermediate hopping sites to aid conduction, and filling those sites would increase potential barrier an electron would have to overcome in a single jump, like discussed in Section 2.6.1. However, the opposite effect can sometimes

be observed. In a disordered network, such as graphene oxide, conductance is dominated from hopping between localised states [89]. In this case, the trap sites act as a Coulomb blockade that restricts the hopping between sites. If these trap sites are filled, the local potential is screened and conductance between the localised states increases. This can be used to make a device on its own in the case of graphene oxide, however for organic molecules this is far more inconsistent since they often result from random defects. Instead, traps can be used alongside another mechanism, such as charge transfer, to improve the memory retention or access multiple stable states.

2.6.4 Ion Migration

Ions are often present in redox memristors, such as the example discussed in Section 2.6 where a PF_6^- is used as a counterion to locally balance charge on the molecule in the various redox states. However, ion migration along a molecule can also be used as the prime driver of the conductance switch in a memristive device. This can happen in a few ways, one of the more popular mechanisms is by the formation of conductive filaments, a pathway formed from ions between the electrodes stimulated by an external electric field. This massively increases conductance as a highly conductive metal ion pathway now connects the electrodes. This filament is stable and dissolves with the application of an opposite electric field, making it a suitable memristive method [90]. This can be used in both inorganic and organic memristive devices. Inorganic devices typically use an oxide material containing oxygen vacancies throughout, usually concentrated around grain boundaries where the crystallinity is imperfect. With the application of an electric field, metal ions move to fill these vacancies and grow into nano-clusters. As they grow the clusters can connect, and form a conductive filament which spreads between electrodes and boosts conductance [91]. In organic devices a film of organic molecules connects the two electrodes, one of which must be made of an active material like copper or silver. Under an electric field, ions are released from the active electrode and can migrate through the free volume of the organic film until it reaches the other electrode and

a conductive filament is formed between them. This can be controlled with the use of cross-linking molecules which can vastly decrease the free volume available, leading to more controlled filament formation and increasing the repeatability and reliability of the conductance in the ON state [92]. Ion migration can also be used to change the conductance in doped organic layers. PEDOT:PSS is a highly conductive organic polymer, where the $PEDOT^+$ is synthetically oxidised and the PSS^- is used as a counterion to balance charge. This makes it highly conductive since there are delocalised charge carrying holes along the polymer backbone and easy hopping between polymers. Under an electric field, ions such as H^+ from an adsorbed water layer migrate to neutralise the PEDOT and PSS, effectively electrochemically dedoping the polymer network and massively lowering the conductivity [93, 94].

Chapter 3

Materials and Methods

3.1 X-ray Photoelectron Spectroscopy (XPS)

X-ray photoelectron spectroscopy (XPS) is a powerful surface-sensitive spectroscopy method which can provide both qualitative and quantitative data on the chemical environments present at the surface of a material. Operating under ultra high vacuum (UHV), the XPS uses the photoelectric effect to determine information about the elements present and their bonding situations within the top few nanometers of a given sample. This is an often essential analysis which gives unique details about purity, assembly and structure of a sample.

3.1.1 Working Principles

XPS uses monochromatic X-rays targeted at a material to release photoelectrons from the surface via the photoelectric effect. The energy of these photoelectrons can then be used to determine the binding energies of the electrons within the material, giving information about the element that electron was from and details on bonding situations the element may be in. A schematic of the working process of an XPS unit is shown in Figure 3.1. To begin, a tungsten filament is heated electrically via resistive Joule heating, which releases electrons from the filament due to thermionic excitation [95]. These electrons are accelerated with a high voltage towards an anode, often made of aluminium. This preferentially ionises the core K electrons in the aluminium anode due to the high energy of the incoming electron [96]. As the atom relaxes, an electron from a higher energy level drops down to fill the vacancy. This produces a photon at a very well defined energy. For aluminium, this is dominated by electrons from the next band up, L, dropping to fill the K vacancy, producing K_α x-rays with 1486.6 eV [97]. Additional x-rays are also produced, from different electrons being ionised, electrons from different bands filling the core vacancy, and a continuos range of background Bremsstrahlung x-rays from electrons losing energy in the anode [98]. These can be filtered out with the use of a quartz monochromator, which can be tuned to reflect only the desired K_α photons to be directed towards

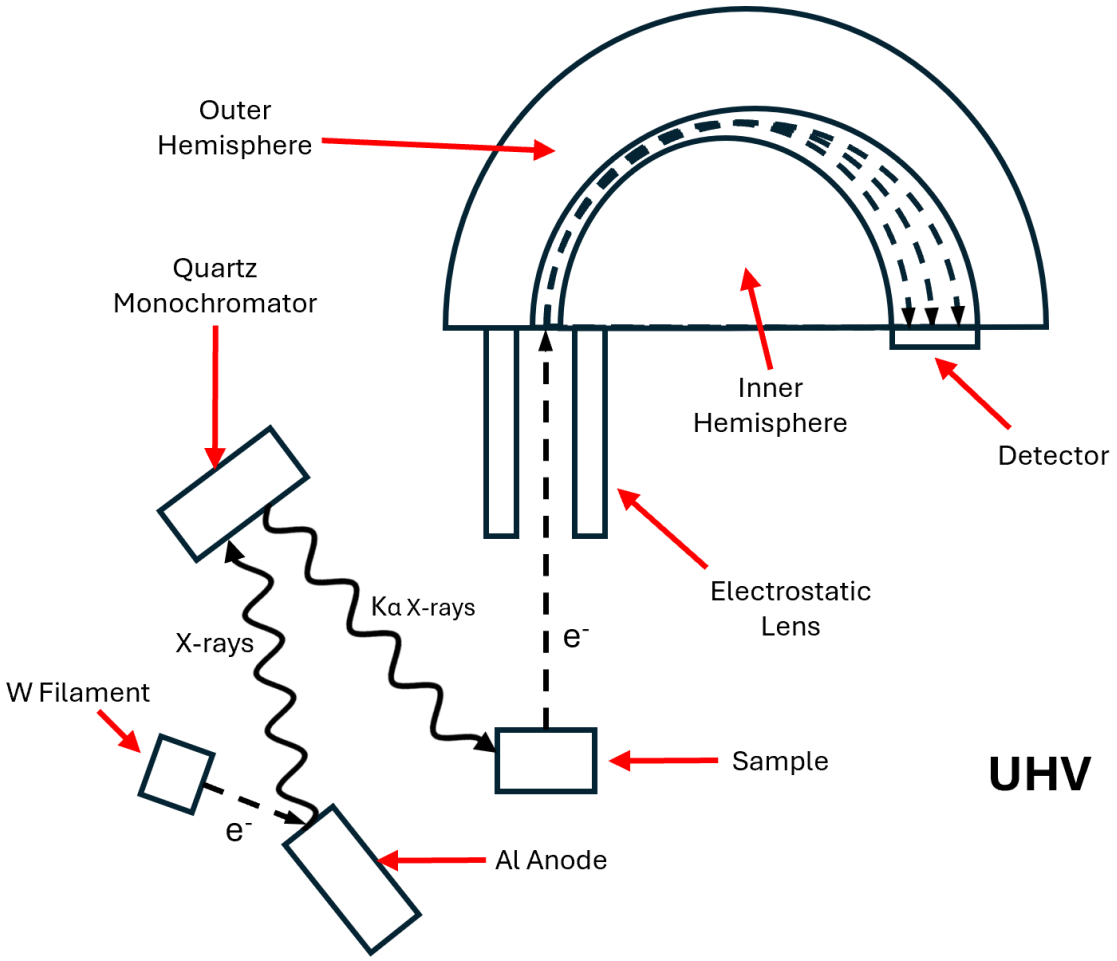

Figure 3.1: Schematic of the major components needed for standard spectra capture in an XPS unit. The mechanism outlined with the diagram takes place, in its entirety, in ultra high vacuum (UHV).

the material surface [99].

These x-rays deeply penetrate into the material, causing photoemission to occur up to several micrometers under the surface. However, most of these photoelectrons undergo inelastic scattering within the material and cannot escape. The intensity, I, of unscattered electrons with depth z into a material is given by the exponential dependence for photoelectron attenuation

$$I(z) \propto e^{\frac{z}{\lambda}} \tag{3.1}$$

where λ is the inelastic mean free path of the electron [100]. Although λ is material dependant, there is a universal dependence on electron energy, shown in Figure 3.2, which can be used to estimate λ for a given electron energy.

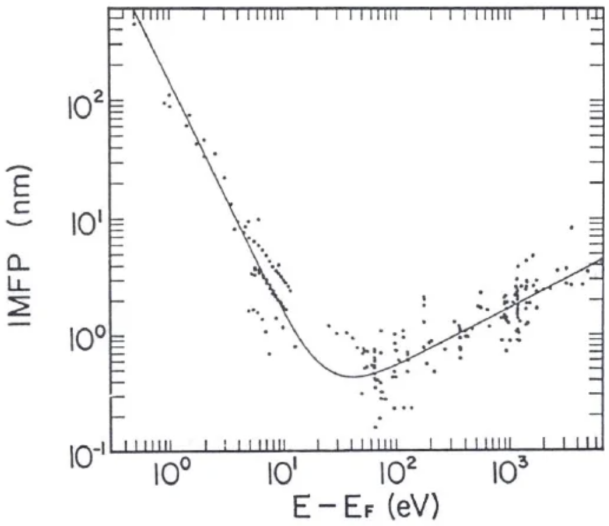

Figure 3.2: Universal dependence of inelastic mean free path (IMFP), λ, on electron energy, averaged over various materials. Image from [101].

As can be seen from the plot in Figure 3.2, λ is typically 2-3 nm for the range of kinetic energies an electron might have after being ionised by an aluminium K_α photon [102]. From Equation 3.1, over 95% of the electrons that escape the surface are within the top 3λ of the material. This is 6-9 nm from typical energies used in an XPS, and is therefore a surface-sensitive technique. Photoelectrons which are emitted from the surface without undergoing any inelastic scattering will have kinetic energy, E_k, given by

$$E_k = E_{ph} - E_B - \phi_s \tag{3.2}$$

where E_{ph} is the energy of the incoming photon, E_B is the binding energy of the electron, and ϕ_s is the work function of the sample.

3.1.2 The Electron Analyser

Emitted photoelectrons travel up through a series of electrostatic lenses which funnel the electrons into a beam and decelerates them by a fixed amount before entering the hemispherical analyser. The analyser is comprised of an inner and outer hemisphere with an electric field between them. A predetermined pass energy is set, where the analyser only allows electrons of that energy to pass through. Electrons of the correct energy arc with the correct radius to reach the detector, deviations from this radius will result in the electron colliding with either the inner or outer hemisphere. The resolution, ΔE, of the analyser is determined by

$$\Delta E = E_p \left(\frac{w}{2R_p} + \alpha^2 \right) \tag{3.3}$$

where E_p is the pass energy, w is the slit width into the analyser, R_p is the average radius and α is the acceptance angle [103]. Since the slit width, radius and acceptance angle are all fixed by instrument design, the pass energy set directly determines the resolution [104]. Physically, a higher pass energy results in smaller radius changes of an arcing electron of energy E, where $E = E_p + \Delta E$ [105]. This allows a greater range of energies to complete the correct radius and be accepted by the detector. A higher pass energy therefore increases the counts but reduces resolution.

As the XPS takes spectra, it sweeps the accepted energy for electrons. It does this by changing the counter field used to decelerate the electrons in the electrostatic lenses. For example if the pass energy of the analyser is $E_p = 20\,\text{eV}$, and the sweep is at a point where electrons of kinetic energy 1 keV are being detected, the lenses provide a retarding potential of 980 V against the flow of electrons, reducing their kinetic energy by 980 eV as they move against the electric field. Electrons of the initial correct energy would then have 20 eV kinetic energy as they enter the analyser and are allowed through to the detector. By sweeping the range of possible photoelectron energies from a given monochromatic x-ray source, a spectrum of binding energies

ejected from the sample is built up.

When calculating the binding energies, an important adjustment should be made to Equation 3.2 since the energies measured by the analyser will have an offset equal to the difference in work function, $\Delta\phi$, and Fermi energy, ΔE_F, between the sample and analyser.

$$E_B = E_{ph} - E_k - \phi_s - \Delta\phi - \Delta E_F \tag{3.4}$$

The sample and analyser should be electrically connected. This forces the Fermi energy of the sample to match that of the analyser as they reach thermal equilibrium, so $\Delta E_F = 0$ [106]. Since $\Delta\phi = \phi_a - \phi_s$ where ϕ_a is the work function of the analyser, Equation 3.4 becomes

$$E_B = E_{ph} - E_k - \phi_a \tag{3.5}$$

where ϕ_a and E_{ph} are known, E_k is measured, and so the binding energy B can be calculated. Systematic offsets may be applied to the calculated binding energies. This can happen in insulating samples where there is not a good electrical connection between the sample and the insulator, so the Fermi energies do not properly align and ΔE_F becomes non-zero. This can also lead to peak broadening as the sample is dynamically charged during measurements as electrons are not easily refilled from the bulk sample holder. A charge neutraliser electron gun can be used to aid this issue, but usually does not fully solve the problem. These offset issues can be accounted for by shifting the output spectrum in accordance to a reference peak of known value. In this thesis, all XPS data shown is shifted to match the C 1s peak at 284.8 eV [107].

3.1.3 Peak Splitting and Shifting

When fitting XPS data, it is important to realise the factors which can shift or split the peaks so the data can be fitted and interpreted correctly. Spin-orbit coupling splits peaks with orbital angular momentum, $l > 0$. The total angular momentum,

the j quantum number given by $j = |l \pm \frac{1}{2}|$, splits the energy levels into multiple states with degeneracy $2j + 1$. In the example of an S 2p orbital, the p orbital corresponds to $l = 1$ and therefore splits into states of S $2p_{3/2}$ and S $2p_{1/2}$. The relative area of the created doublets is given by the degeneracy of the states, so the area ratio of S $2p_{3/2}$ to $2p_{1/2}$ is 2:1. The shift between the two spin-orbit states is a well defined 1.2 eV [108]. This significantly aids fitting by forcing strict parameters and results in a distinct characteristic shape. The XPS of a study by Poppenberg *et. al.* is shown in Figure 3.3a as an example of sulphur peak fitting with these parameters [109].

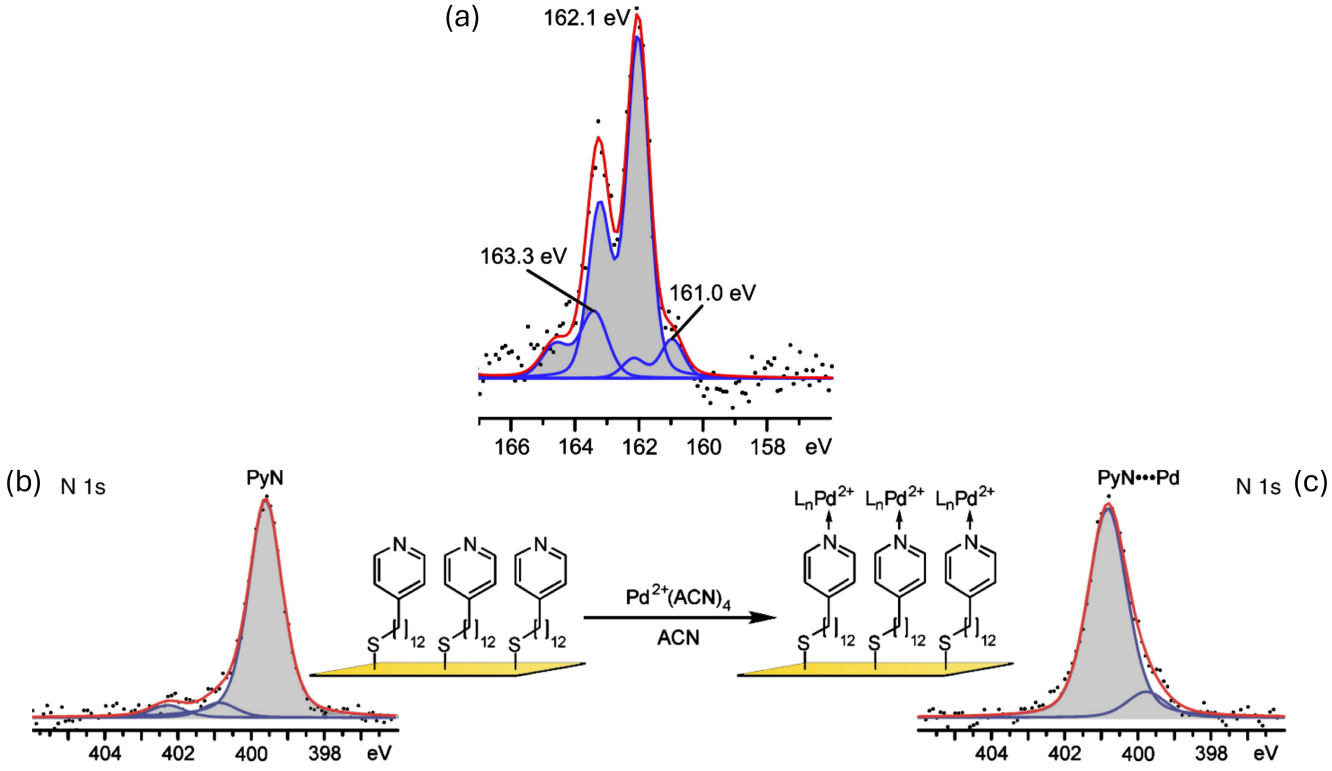

Figure 3.3: Example XPS (a) S 2p spectrum for a self-assembled monolayer (SAM) of 12-(pyridin-4-yl)-dodecane-1-thiol (PDT) on a gold substrate. The sulphur doublets are fitted with the same colour using a 1.2 eV shift and 1:2 area ratio [110, 111]. (b) N 1s spectrum for the same SAM and (c) the SAM with pyridines coordinated to a top Pd layer. Images from [109].

Poppenberg *et. al.* assign the 163.3 eV peak to unbound thiols and the 162.1 eV peak to S-Au bonds. They also acknowledge the peak at 161.0 eV to be a different S-Au bonding situation. Similarly low S 2p binding energy peaks are observed in this thesis and are discussed in detail in Section 5.3.2. The shift in the doublets in sulphur spectra, such as Figure 3.3a, is due to the local binding environments which gives information on how the monolayer is assembled on the surface. As the anchor groups of the molecules bind to the metal surface, in this case sulphur to gold, various factors affect both the initial and final states which determine the measured binding energy of the electron.

The initial state is while the electron is part of the atom, before any photon interaction. Sulphur is more electronegative than gold [112], so in a bond the electron density is shifted towards the sulphur atom and away from the gold atoms. This gives it a partial negative charge and reduces the binding energy of core sulphur atoms from screening effects. The final state is after electron excitation from an incoming photon. In the case of measuring a S-Au bond with XPS, the binding energy shift is dominated by the final state effects. As the electron is being ejected, a hole is formed in its place. This hole ordinarily slows down the electron by Coulomb attraction because of its positive charge. However, in the case of hole formation close to a metallic surface, the electrons within the metal instantaneously redistribute to create an image charge, equal and opposite to that of the created hole. This image potential screens the hole, allowing the electron to escape with a higher kinetic energy. This reduction of the final state energy reduces the measured binding energy for a sulphur electron in a S-Au bond [113,114]. The initial and final state effects are combined, producing the shift in the binding energy from unbound thiols to thiolate-Au bonds seen in Figure 3.3a.

As well as thiols, Pyridyl is the other main anchor group used in molecules in this thesis. For the case of pyridyl coordination to a metal, the binding energy increases

with respect to the unbound variant. An example is shown in Figure 3.3b-c, where the binding energy of the large peak shifts upwards after the top pyridyl groups coordinate to a palladium top layer. Pyridyl coordinates to the metal via its lone pair, which point out from the aromatic ring orthogonally to the π-system. The lone pair is donated to the metal, resulting in a charge depletion of the nitrogen atom [115]. This reduces the screening of the N 1s core electrons, resulting in a greater measured binding energy from initial state effects. Similar positive shifts have been shown in studies of pyridyl coordination to bulk gold electrodes, where the final state screening effects still occur [116]. The initial state effect in this case is larger than the final state effect, resulting in a net positive shift in the binding energy for pyridyl coordination to metal.

In this thesis, XPS plots are shown with a binding energy on the X-axis, reversed due to the direct measurement being kinetic energy which reduces as binding energy increases. The y-axis is intensity in arbitrary units, since counts cannot be compared between measurements, only relative areas. The electron energy distribution around a given value is broadened in different ways. The excited electron state comes with a natural energy uncertainty arising from the short lifetime of the created hole. The natural linewidth of a given orbital follows a Lorentzian distribution. The spectrometer also adds broadening. This follows a Gaussian distribution and is dominated by the resolution of the analyser. Therefore, XPS peaks are fitted with a Voigt function, a mix of Lorentzian and Gaussian functions which can be tuned to give a greater weighting to one or the other [117]. All spectra in this thesis are fitted using Voigt functions on CASA XPS software.

3.2 Atomic Force Microscopy (AFM)

An atomic force microscope (AFM) allows the user to interact with the surface of a sample on the nanoscale. A sharp tip connected to a cantilever can be used to

obtain point measurements or produce a map of the surface by raster scanning over a given area. The height map produced is typically created by measuring tip-sample forces probed over the surface. However, by modifying the probe and changing aspects of the AFM setup, a wide range of different properties can be measured, making AFM a very versatile technique. In this thesis, a multimode AFM is used to characterise the topography and thickness of molecular films and measure their electric and thermoelectric properties, as described later in this chapter.

3.2.1 Working Principles

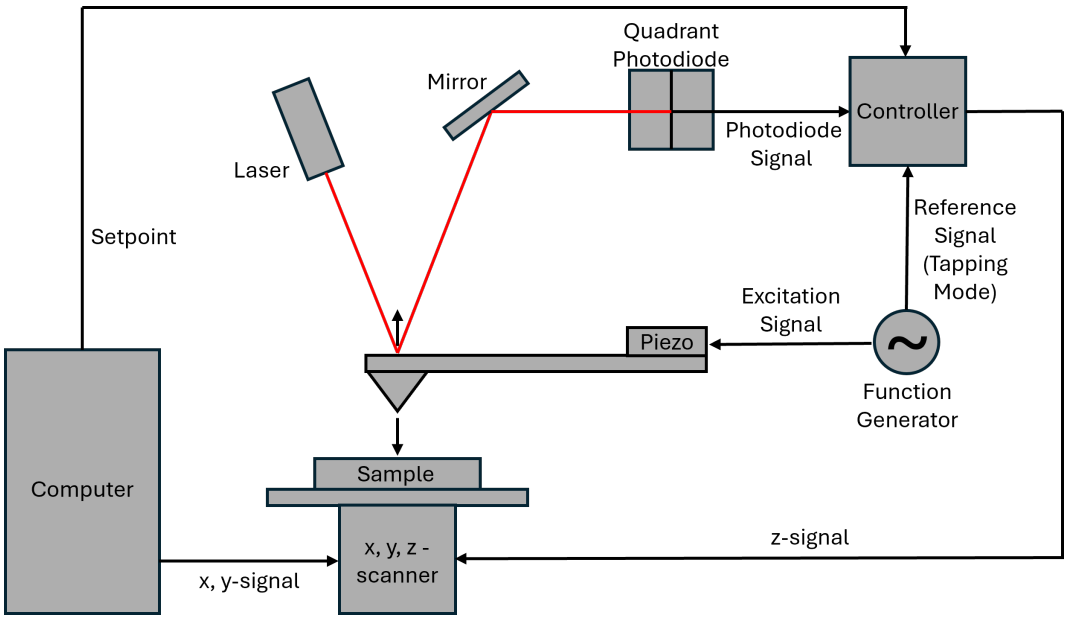

Figure 3.4: Schematic diagram of AFM operation including major components and signals used. The processes involved in the controller and how they differ for different modes are detailed in Section 3.2.3.

The basic principle of an AFM is shown in Figure 3.4. A tip which typically has a 10 nm radius, but can also be atomically sharp, is attached to the end of a cantilever beam. This cantilever can be driven at a particular frequency by a piezo depending on the intended mode of operation. The oscillation amplitude is measured using a laser which shines onto a reflective coating on the back of the

cantilever and is reflected onto a quadrant photodetector. As the tip approaches the surface of a sample, it experiences a combination of forces (detailed in Subsection 3.2.2) which results in some bending of the cantilever. These small movements result in a measurable shift in the laser position on the photodetector. The spot size of the laser is large compared to the photodetector squares such that all squares receive some light. A signal is produced from the photodetector calculated by the relative intensity on each of the squares, which is highly sensitive to the position and movement of the laser. The changes in deflection are used to detect surface changes, and react to them with a feedback loop. A variety of modes can be used, where in each case one parameter varied to keep another parameter constant at a pre-defined setpoint. Changes from the measured value to the setpoint are calculated, indicating the tip is sensing a change in the surface during a scan. A z-signal is then sent to the scanner to adjust the height and counteract the change. This feedback loop of reacting to surface changes allows for mapping as the adjustments are measured. The exact process is different for each AFM mode, the details of which will be discussed in Section 3.2.3.

3.2.2 Forces Involved in AFM

First we will discuss the long-range van der Waals attractive forces. This can occur through three different methods: dipole-dipole, dipole-induced dipole, and induced dipole-induced dipole interactions. The first occurs when two polar molecules interact with each other with Coulomb attraction. The second is where a polar molecule distorts the electron cloud of a nearby non-polar molecule, inducing a dipole and therefore causing attraction between them. The third, also known as London dispersion forces, occurs when the fluctuating electron cloud in a neutral molecule can create an instantaneous dipole which then induces a dipole in a neighbouring molecule. This induced dipole stabilises the original, creating a stable attracting force between them. Since this occurs between two neutral molecules, it is the most common effect of the three [118].

At close tip-sample separation, where the electron shells between the probe and surface begin to overlap, a strong repulsive effect dominates due to the Pauli exclusion principle [119]. Electrons cannot occupy the same quantum states, and since the number of low energy states is limited, some electrons are forced to occupy higher energy states. It is this change in potential energy that results in a repulsive force, which is very strong at small distances and so dominates over the attractive van der Walls when the tip gets too close to the surface. These two forces are the main contributors to a simplified AFM approach which excludes environmental factors. The combination of these interactions at a distance r is modelled by the Lennard-Jones potential, V_{LJ},

$$V_{LJ}(r) = 4\epsilon \left(\left[\frac{\sigma}{r}\right]^{12} - \left[\frac{\sigma}{r}\right]^{6} \right) \tag{3.6}$$

where ϵ is the depth of the potential well and σ is the zero-potential distance [120, 121]. The $\left[\frac{\sigma}{r}\right]^{12}$ term is the repulsion from Pauli exclusion, and the $\left[\frac{\sigma}{r}\right]^{6}$ term is the attraction from van der Waals. Equation 3.6 can be plotted to visualise the combination of the attractive and repulsive forces and produce the characteristic Lennard-Jones potential shape, shown in Figure 3.5.

As the tip approaches the surface, the van der Waals dominates and starts to increase rapidly, as can be seen in Figure 3.5. Once this exceeds the restoring force of the cantilever, the tip snaps into contact with the surface [122]. This effect is dramatically increased in the presence of water layers during ambient AFM. In ambient conditions, a water layer coats both the tip and the surface. Once these are in contact, they form a meniscus and capillary forces pull the tip towards the surface. This is stronger and occurs at a greater distance than a snap-in caused purely from van der Waals forces. As the tip is retracted from the surface, it remains in contact until the adhesive tip-sample interaction is overcome. In ambient

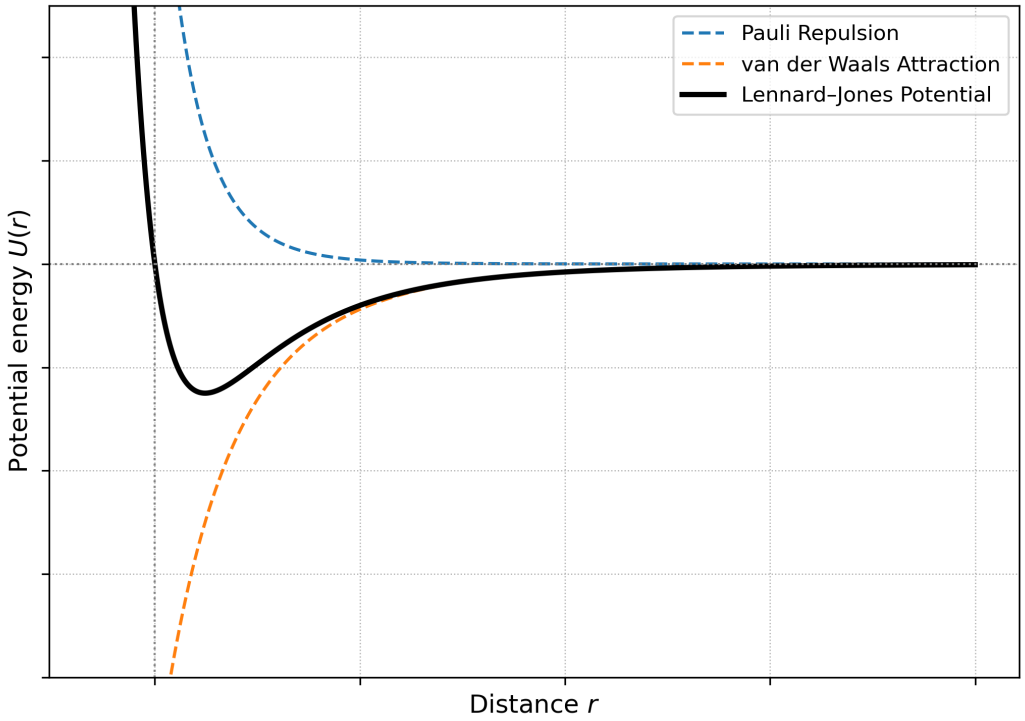

Figure 3.5: Plot of the Lennard-Jones potential, with the contributing factors of Pauli repulsion and van der Waals attraction also shown. The plot is produced from Equation 3.6, where σ is the where the Lennard-Jones potential crosses the x-axis. and ϵ is the lowest point of the dip.

conditions, this is dominated by capillary forces as the tip tries to break from the meniscus. However, other forces also contribute, such as electrostatic forces and any forces due to chemical bonds which may have been formed [123].

3.2.3 AFM Modes

3.2.3.1 Contact Mode

In contact mode, the tip does not oscillate and experiences a continuous interaction with the surface. A feedback loop is commonly implemented to achieve a constant force, where a user defined setpoint is maintained. The tip-sample force is determined using the laser deflection on the photodetector and is then converted

into a force, F, using Hooke's law

$$F = -kx \tag{3.7}$$

where k is the spring constant of the cantilever and x is the deflection [124]. For a given time t_0, the actual force is compared to the setpoint, creating an error signal $e(t_0)$. The PI (proportional-integral) controller uses this error signal to output a voltage, Z_V, which is applied to the z-piezo to adjust the height of the scanner [125]. The PI controller uses equation 3.8 to calculate the required output Z_V

$$Z_V = G_P e(t_0) + G_I \int_0^{t_0} e(t)\mathrm{dt} \tag{3.8}$$

where G_P and G_I are the proportional and integral gains respectively [126]. The proportional part of the response reacts to instantaneous changes on the surface, providing an immediate correction response. The integral part accumulates all of the error signals up to this point and compensates for them. This corrects systematic offsets, ensuring over time the average force measured is that of the setpoint. The continuous height adjustments from Z_V are recorded to produce a topographical map of the surface. This method can be destructive to both the sample surface and the tip. However, the destructivity of the method can also be exploited, as deforming molecular layers can give information about their height and structure.

3.2.3.2 Amplitude Modulation AFM

Contact mode operation can result in severe damage to samples, especially soft samples such as molecular thin films. This is due to the high lateral forces, in addition to the vertical forces, involved in operation. Sample damage can be mitigated by reducing the contact time to tapping within an oscillation cycle. The most common implementation of this technique is amplitude modulation (AM-AFM). In AM-AFM, the cantilever is oscillated at a frequency close to its resonance. The driving frequency does not change throughout measurement, and so the amplitude of oscillation changes with the change in interaction forces as the

tip approaches the surface. The excitation signal sent to drive the cantilever is also sent to a lock-in amplifier as a reference signal (see Figure 3.4). As the cantilever oscillates, the signal from the photodetector is sent to the lock-in amplifier too, where the amplitude and phase can be separated. It does this by multiplying the detector signal by the reference frequency sine and cosine, then passing the results through low-pass filters to remove the high-frequency terms [127]. The amplitude and phase can then be extracted from the results. The amplitude is compared to a predetermined setpoint from the computer to create an error signal. The PI uses this to adjust the tip-sample separation to restore the amplitude to setpoint [128].

in AM-AFM, the amplitude of oscillation is large (1-100 nm). This is large enough for the tip to contact the surface during the oscillation, where the amplitude will change by a measurable amount due to the considerable interaction force changes when in contact, described in Section 3.2.2. The phase can also be used as a separate imaging channel to give mechanical information, such as the adhesion and stiffness, about the sample [129].

3.2.3.3 Non-Contact AFM

True non-contact AFM (NC-AFM) uses frequency modulation (FM-AFM) to sense the surface without snapping into the surface. The cantilever is driven at its resonant frequency above the surface at a small amplitude. As the cantilever approaches the surface, the interaction forces change and the resonant frequency shifts. Two independent control loops use the photodetector signal. An amplitude detector measures the amplitude and then adjusts the drive force to keep the amplitude constant and small during scanning. A phase-locked loop (PLL) measures the phase, and then adjusts the driving frequency to keep the cantilever oscillating on resonance [130]. The required shift in frequency is the variable component which is compared to a setpoint to create an error signal. The PI adjusts the tip-sample separation to keep this shift in frequency at the predetermined setpoint which is set

on the computer.

FM-AFM is typically used in ultra-high vacuum (UHV) conditions. This is because the quality factor of the cantilever resonance, Q, is greatly increased due to the absence of environmental dampening, which greatly improves frequency resolution. Changes in resonant frequency are highly sensitive to changes in the interaction force, allowing for excellent resolution down to the atomic scale. Also, FM-AFM provides a good alternative to AM-AFM which cannot be used effectively in UHV. The high Q from a UHV environment results in slow amplitude changes, since the ring-down time constant, τ, is related to Q as $\tau \propto Q$ [131]. Such a poor amplitude response makes AM-AFM impractical for use in UHV and FM-AFM a far better choice.

3.2.3.4 Peak-Force AFM

Peak-force mode uses a sinusoidal drive to oscillate the cantilever well below resonance. The deflection of the cantilever is measured from the photodetector, and converted to force from Equation 3.7 as in contact mode operation. As the cantilever oscillates, force-distance curves are continuously measured. The peak force measured from these curves is compared to a setpoint value and, like the previous modes, the PI uses the error signal to adjust the tip-sample separation, keeping the maximum force measured for each force-distance oscillation constant. As the tip first engages on a surface, the measured peak force in an oscillation cycle increases as the tip-sample separation decreases. This iterative process continues until the peak force matches the setpoint, at which point the probe is engaged and begins scanning as described above. This is illustrated in Figure 3.6. A careful engage in this manor protects the tip and sample surface by ensuring forces never get too high, even during the initial engage.

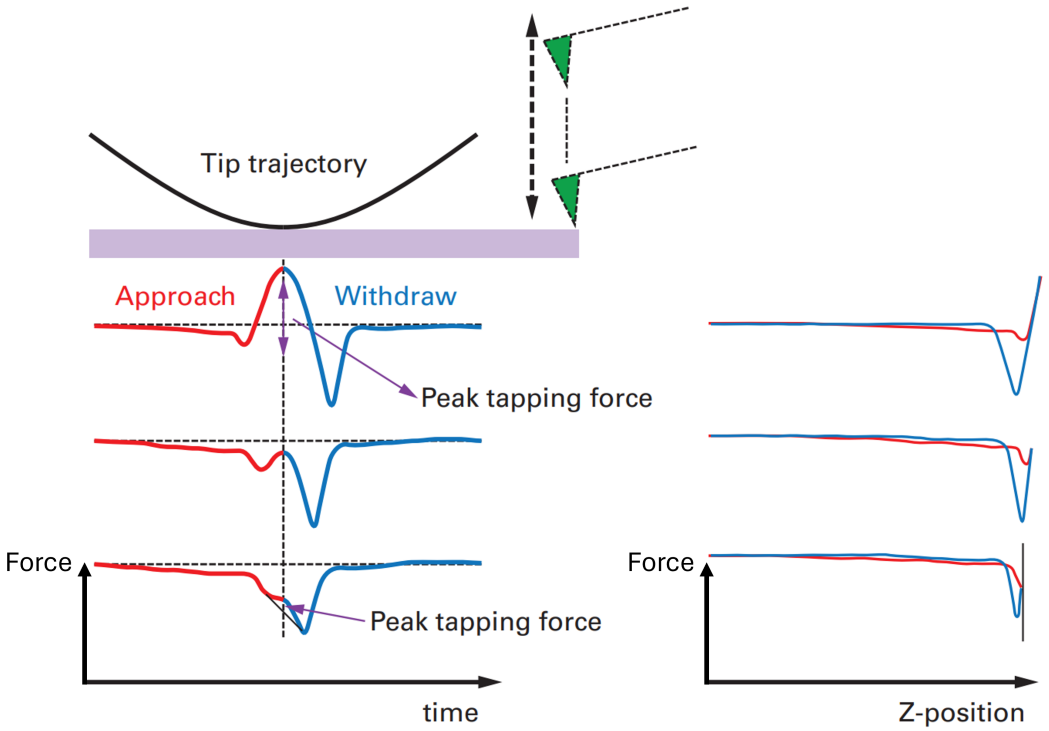

Figure 3.6: Illustration showing the motion of the probe in peak-force mode. A series of force-time (left) and force-distance (right) plots are shown for individual oscillation cycles as the tip approaches a surface and reaches a setpoint. For each oscillation, the red line is the approach and the blue line is the retraction. Image from [132].

The snap-in can be seen by the attractive spike on the red approach line in Figure 3.6. After this, the short range Pauli repulsion forces dominate, shown by the steep gradient into the repulsive regime. The strong distance dependence of the short range force is what can give peak-force mode exceptional lateral resolution. Additional properties of the surface can also be probed from examination of the force-distance plots. For example, the large attractive spike as the tip begins to withdraw gives a measure of the adhesion experienced by the tip to the surface. Peak-force gives precise control over the force exerted by the tip on the sample, and can be operated using setpoints as low as 50 pN. This minimises damage done to the surface and tip, which can be useful when dealing with delicate materials [132]. All

topographic AFM images presented in this thesis were captured using peak-force mode.

3.2.3.5 Conductive AFM

By coating the tip in a conductive material such as platinum, gold or graphene, electrical properties of the tip-sample junction can be measured. Additionally, manufacturing the tip out of a conductive material rather than coating a silicon probe greatly improves the lifetime as there is no coating to wear down through operation. The electrical measurements performed in this thesis use a platinum coated silicon tip (Budget Sensors Multi75E-G).

During conductive AFM (cAFM), the top of the sample should be electrically connected to the conductive stage, usually via a conductive clip. While the tip is in contact with the surface, a bias voltage is applied between the surface and the tip. The resulting current is measured via the AFM tip, allowing for the creation of current-voltage (I-V) traces as the bias voltage is swept [133]. In this thesis, conductance measurements were taken with the use of a Bruker TUNA module, which is a high-gain, low-noise transimpedance amplifier. This uses tunable gains to measure current ranges from hundreds of nA, down the the fA scale [134]. A transimpedance amplifier converts a small input current into a measurable voltage. An example circuit diagram is shown in Figure 3.7.

A transimpedance amplifier uses an operational amplifier, shown by the triangle in Figure 3.7, to measure the voltage difference between two inputs. The non-inverted input is connected to ground, while the inverted input is connected to the tip. A transimpedance amplifier utilises a negative feedback loop to keep the voltage difference to zero. The inverted input, and hence the tip, are therefore held at a virtual ground. As the small currents arrive at the inverted input, the voltage

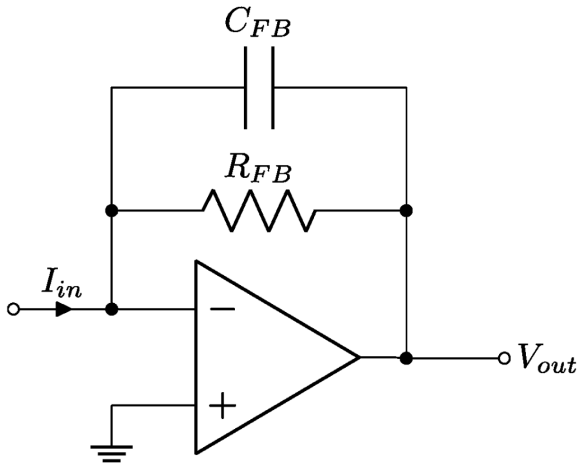

Figure 3.7: Example circuit diagram of a transimpedance amplifier. The minus sign represents the inverted input while the plus sign represents the non-inverted input. The non-inverted input is held at ground. Image from [135].

changes. The feedback loop triggers a counter-current to flow through a resistor, R_{FB}, to neutralise the current at the input and restore the voltage difference to zero. Since the transimpedance amplifier draws negligible current itself, it uses the initial current, channelling all of it back through R_{FB} to perfectly counter the current. The resistor has a very high resistance, and since all of the input current is channelled back through it, the output voltage $V_{out} = -I_{in}R_{FB}$ [136]. Note the result is negative, due to the measured current flowing in the opposite direction to the input current. This is why the input through this channel is known as "inverted input". The transimpedance amplifier has therefore successfully converted an input current into a voltage, and multiplied it by some large amount. The Bruker TUNA module has selectable gains, where the the resistance of R_{FB} can be altered to change the gain of the amplifier, from 10^7 V/A to 5×10^{10} V/A, allowing for a wide range of currents which can be measured. The output voltage can then be converted back into a current value since the resistance of R_{FB} is known. I-V traces of measured tip current against applied bias voltage can then be plotted.

Taking the gradient at each point of an I-V trace gives the differential conductance throughout the bias voltage sweep. Compiling hundreds or thousands of traces allows for a 2D histogram heat-map to be plotted. As an example, Wang *et. al.* explored how different terminal anchor groups with varying connectivity around an aromatic anthracene core affects electrical properties such as conductivity and the Seebeck coefficient [137]. Their results using over 200 I-V traces for each molecule in a self-assembled monolayer (SAM) are plotted as 2D histograms as described above.

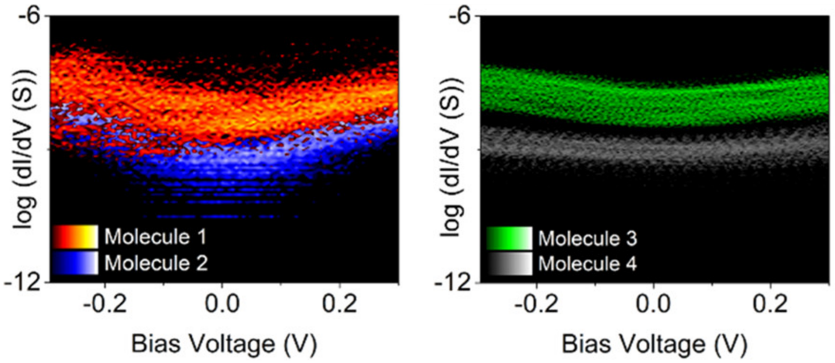

Figure 3.8: 2D histograms showing the conductances of four molecules with anthracene cores. Molecules 1 and 2 on the left have thioether terminal anchor groups with 9,10' and 1,5' connectivities respectively. Molecules 3 and 4 have thioacetate terminal anchor groups with 9,10' and 1,5' connectivities respectively. Image from [137].

The 2D histograms depicted in Figure 3.8 show the frequency and spread of calculated conductivities through the bias voltage sweep. A brighter colour corresponds to more frequently measured values. Taking values close to zero bias, values for G/G_0 can be calculated. The results are presented in Table 3.1. The results determined that molecule 1 had a bigger conductance than molecule 2 by a factor of 10.2, and molecule 3 had a bigger conductance than molecule 4 by a factor of 14.2. The difference in conductivity is clear in Figure 3.8 as the red and green bands (molecules 1 and 3) are distinctly higher than the the blue and grey bands

Molecule	G/G_0	Uncertainty	Theory G/G_0
Molecule 1	7.01×10^{-5}	9×10^{-6}	1.66×10^{-4}
Molecule 2	6.88×10^{-6}	1×10^{-6}	1.05×10^{-5}
Molecule 3	1.28×10^{-4}	5×10^{-6}	1.59×10^{-4}
Molecule 4	9.00×10^{-6}	3×10^{-6}	1.00×10^{-5}

Table 3.1: Table of results as an example interpretation of the 2D histograms shown in Figure 3.8. Results from [137].

(molecules 2 and 4). Additionally, the uncertainty in the values is easily visualised from the spread of these bands, with the red and green bands clearly being wider than the blue and grey bands, corresponding to a larger uncertainty. The results show that theoretical predictions of conductance scaling due to core connectivities causing constructive interference at room temperature can still be applied to a full SAM. The theoretical conductances, obtained from density functional theory (DFT) calculations, predicted an increase in conductivity between 9,10' and 1,5' connectivities by a factor of 16. The actual values of 10.2 and 14.2 are lower but of the same order of magnitude. In fact, each individual molecule has a lower measured conductance compared to the theoretical value, implying packing in a SAM hinders the conductance somewhat. This could be due to many factors, including the variety in adsorption geometries, difference in coupling strengths and inconsistent contact with the AFM probe. The molecules are investigated again in one of the projects in this thesis, as seen in Chapter 6.

3.2.3.6 Seebeck Measurements

Seebeck measurements, similar to conductance measurements, also use a conductive AFM tip. In this case, the measurement is of the thermovoltage generated between sample and the conductive tip due to a heat gradient between the two. The stage is placed on a Bruker heating element and is electrically isolated from the rest of the AFM using an insulating disk. The thermovoltage is measured using a high

impedance differential voltage amplifier. The tip is electrically connected to one input, while the sample is electrically connected to the other [116]. The high impedance input ensures negligible current is drawn, so a true thermovoltage can be measured, yielding an accurate Seebeck coefficient from Equation 2.6 which requires open-circuit measurements.

Once the tip is in contact with the surface and a molecular junction is formed, heat is applied to the substrate. This creates a heat gradient over the molecule and generates a thermovoltage dependant on the Seebeck coefficient of the molecule. As this happens, the tip can be assumed to remain at room temperature. The silicon of the tip has a very high thermal conductivity of $150\,\mathrm{W\,m^{-1}\,K^{-1}}$ [138] and is connected to a large thermal reservoir of the probe holder and body of the AFM [139]. Most of the heat transfer is due to conduction through air rather than through the molecule [140]. Since the surrounding air has a significantly lower thermal conductance than the silicon probe, heat is lost to the thermal reservoir faster than it is gained. The probe is therefore close to room temperature, with at least 95% of the temperature difference occurring across the molecule [116].

The generated thermovoltage is detected by the high impedance differential amplifier ($> 10^{12}\,\Omega$), which amplifies the signal to a measurable amount, similar to the TUNA module for conductance measurements. Whereas the TUNA module keeps a virtual ground at the inputs, this amplifier uses high impedance inputs to draw negligible current and keep the amplifier inputs effectively open-circuit. A similar negative feedback loop is used to restore the operational amplifier inputs to equal voltages, using a current from the supply rails and large resistors. Since the voltage drop over the resistor will be large, a large initial voltage is needed to create the small voltage required to balance the inputs. This large voltage is the amplified output, since it is proportional to the initial voltage difference over the junction multiplied by a known gain [141, 142].

Measurements are repeated at regular temperature intervals. A graph of thermovoltage against temperature can then be plotted. The gradient of this line gives the Seebeck coefficient of the measured molecule. An example can be seen in Figure 3.9.

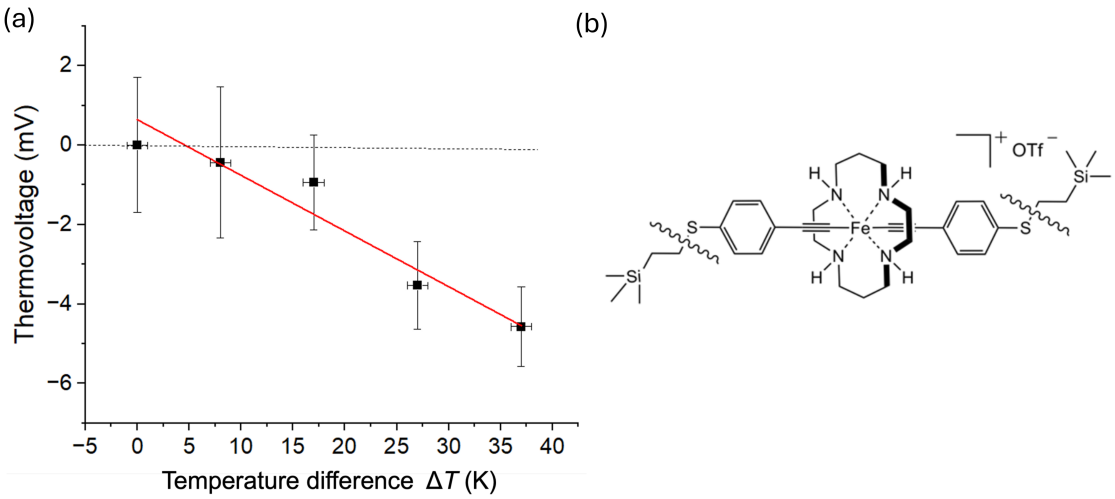

Figure 3.9: (a) Seebeck results from Santos Almeida *et.al.* Measured thermovoltage against change is temperature is plotted, allowing the Seebeck coefficient to be calculated from the gradient. The reported Seebeck coefficient for this plot is $145 \pm 23\,\mu$V/K. (b) Schematic of the molecule self-assembled on a gold substrate to produce the Seebeck results shown. Images from [143].

Santos Almeida *et. al.* performed Seebeck measurements using a platinum tip on a SAM of Fe centred tetraazacyclotetradecane with conjugated arylacetylide ligands on a gold substrate. Their results are shown in Figure 3.9, whereby they report a Seebeck coefficient of $145 \pm 23\,\mu$V/K [143], which appears to be the largest experimentally measured Seebeck coefficient for an organometallic molecular monolayer between two metal electrodes.

3.3 Molecular Self-Assembly

Molecules can self-assemble once adsorbed onto a surface to create an ordered mono-layer or multi-layers. Once adsorbed, competing molecule-surface, molecule-molecule and molecule-environment interactions are all taken into consideration as the molecules rearrange on the surface to minimise the free energy of the interface. This typically results in a metastable state, where the ordering occurs but is limited by kinetic barriers providing a local minimum [144]. There are multiple ways to deposit molecules on a surface, whereafter the molecules self-assemble into an ordered structure. The following sections will detail the processes of solution self-assembly and thermal sublimation.

3.3.1 Solution Self-Assembly

A solution of a certain concentration is created by dissolving a given molecule in a solvent. By placing a substrate into the solution for a period of time, the molecules in the solution will adsorb onto the surface and rearrange to an ordered structure, given the molecule is designed with an anchor group with an affinity for the substrate. This is the process of solution self-assembly, whereby a self-assembled monolayer (SAM) is created. A common choice is a thiol anchor and a gold substrate, due to the strong chemisorption of thiolate to gold [145].

It is well reported that the self-assembly process can be divided up into three distinct regimes in creating an ordered, packed monolayer [146–148]. The first stage is a rapid adsorption of the molecules in the solution to the surface. It follows the Langmuir adsorption model which assumes no molecule-molecule interactions. The model describes equal adsorption sites over the surface where each site can adsorb a single molecule, and molecules can desorb, as well as adsorb, from the surface [149]. The adsorption rate is dependant on the number of available sites, and is therefore

dependant on the fractional surface coverage, θ. The net adsorption rate is given by

$$\frac{d\theta}{dt} = k_a C(1-\theta) - k_d\theta \tag{3.9}$$

where C is the concentration of the adsorbate in solution, k_a and k_d are the adsorption and desorption rate constants respectively [150–152]. This process results in rapid surface coverage during the early stages of self-assembly. For example, long-chain alkanethiols in a standard 1 mMol concentration solution in ethanol reached 80-90% of their maximum thickness within a few minutes of gold submersion [153].

After most of the free adsorption sites are taken, the SAM growth diverges from the Langmuir model as the molecules already adsorbed to the surface begin to rearrange. During this stage, molecules can hop between sites, and even desorb then re-adsorb in better configurations. The molecule-molecule interactions can no longer be discarded as they begin to dominate the restructuring on the surface to promote better packing. This becomes very molecule dependant, with longer alkane chains causing stronger packing due to increased van der Waals interactions between molecules, for example [154, 155]. This process of defect healing and improved packing is very slow in comparison to the initial stage, typically taking hours [153, 156]. As well as the molecule-molecule interactions, the molecule-surface interactions impact the length of time this stage takes. Since a thiolate-gold bond is relatively strong, desorption events, essential for improved re-adsorption, are rarer than that which weaker anchor-surface bonds may exhibit. This increases the time needed for packing optimisation.

The final stage occurs after adsorption effects finish and the domains of the molecular islands have been formed. Molecules can still shift around the surface, but tend not to desorb and re-adsorb. This is especially true for strong thiolate-gold bonds, where the energy needed for diffusion across the surface is much less than desorption energy. Molecules can do this to hop between nearby free sites to improve their packing. In addition, tilt angles and orientation will begin to become uniform as neighbouring

molecules have time to interact and relax into the minimum energy configuration. In the specific case of thiol anchor groups, the thiolate-gold bonding predominantly occurs with gold adatoms as opposed to flat surface atoms [157]. These gold adatoms are highly mobile, so can shift to optimise surface free energy without the need for molecule hopping [158]. This process can take hours or days to fully optimise the SAM grown on the surface. It can, however, be helped with the application of heat, which can provide the additional energy needed to reorganise. This allows the kinetic barriers of the free energy that the interface may be limited by to be overcome, pushing the interface energy into another local minima of lower energy, physically resulting in further improved packing [159].

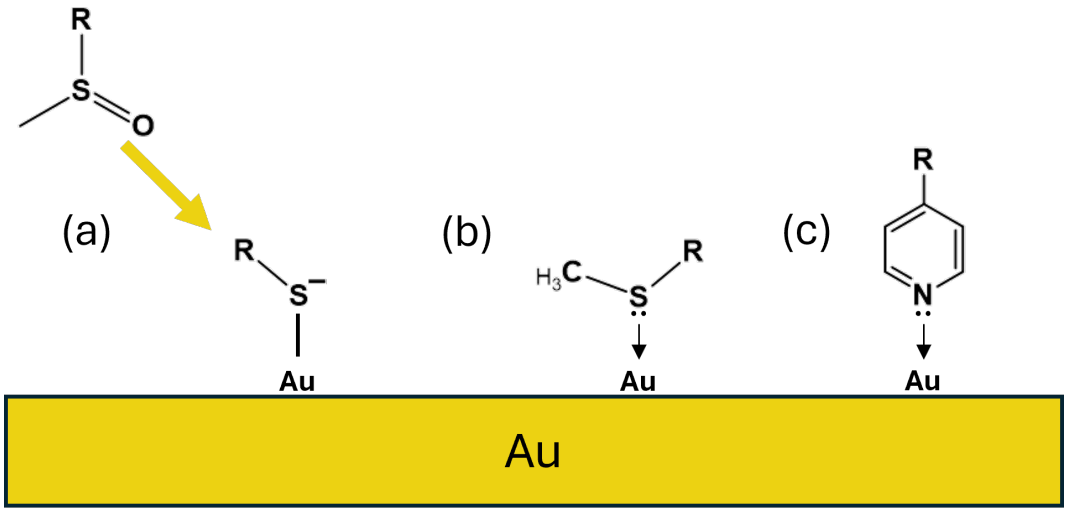

Figure 3.10: Diagram showing the anchor groups used in this thesis. (a) Thioacetate (SAc) which cleaves to a thiolate at the gold surface, (b) methyl thioether (SMe) and (c) pyridine.

In this thesis, both thioacetate and methyl thioether anchor groups are used. In the case of thioacetate, the protected group is cleaved off in the presence of gold, often with the aid of trace water on the surface. As this happens, a thiolate-Au bond is formed, as in Figure 3.10a. The lone pair in the 3p orbital is donated to the gold

surface. However, due to the increased electron density present on the sulphur from the deprotonation at the surface, the orbital energy of the lone pair is increased. This allows the energy to overlap effectively with the gold 6s and 5d orbitals, and therefore forms a strong covalent bond from the orbital hybridisation [160, 161]. This bond is highly directional, typically around 55 ° from the surface normal with a bond energy of around 1.8 eV [162]. For the case of the thioether anchor group, as in Figure 3.10b, no cleaving occurs and instead a dative bond is formed. This is a coordination covalent bond where the sulphur donates its lone pair to the gold, but the back donation is minimal in this case due to poor energetic alignment compared to the thiolate. This is a significantly weaker bond at around 0.4 eV, and therefore less directionally constrained than the thiolate [163].

Pyridine anchors are also used for some molecules in this thesis, as in Figure 3.10c. The nitrogen atom in the pyridine ring provides a lone pair of electrons which are available to coordinate to gold surfaces [164]. This coordination covalent bond is comparatively weaker than a thiolate-gold bond at around 0.1-0.4 eV, but is still classed as weak chemisorption to the surface [165, 166]. The bonding angle is not very directionally constrained due to the weak bond, with reports of tilt angles from the surface normal at 5.5 ° [165] to 45 ° [167]. Pyridine can readily desorb and re-adsorb to the surface, greatly reducing the time needed in stage two as the surface reconfigures to a minimum energy state. This process dominates the SAM structure and packing formation, as opposed to stage three in thiol anchored molecules. The reconstruction can be aided by rinsing the surface mid-deposition. This removes physisorbed and poorly coordinated molecules from the surface, immediately freeing up sites for new molecules to adsorb in a more optimal configuration. The artificial acceleration of desorption has been shown to aid in SAM growth, improving the packing and reducing the number of defects on the surface [168].

3.3.2 Thermal Evaporation in UHV

Another method of making molecular layers is using thermal evaporation under ultra-high vacuum (UHV) conditions. Molecules in a high-purity powder are heated until they sublime into gas phase. This creates a beam of molecules which can be directed towards the desired sample surface, where the molecules will adsorb and self-assemble to an optimal configuration. The adsorption of the molecules to the substrate is predominantly due to van der Waals interactions with the surface. After this initial weak adsorption, stronger interactions can dominate such as charge transfer effects or, if the molecule is designed with anchor groups, surface bonding as described in Section 3.3.1.

Molecules tend to be very mobile on the surface after a deposition due to thermal sublimation, so can easily arrange to the minimum energy configuration. How molecules assemble on the surface depends on the relation of the molecule-molecule interaction strength to the molecule-surface interaction strength. The assembly on the surface can follow one of three modes of growth, depicted in Figure 3.11.

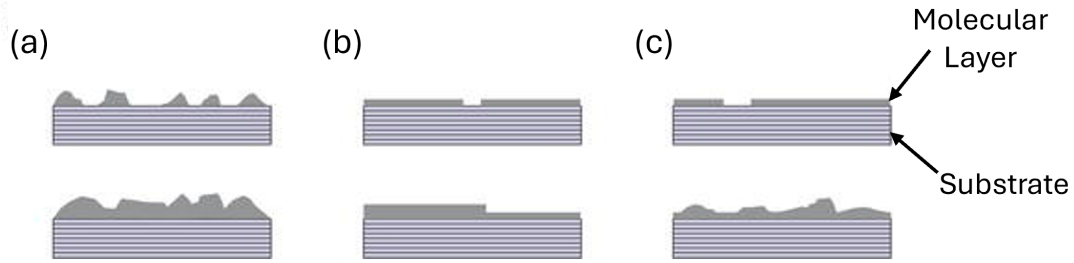

Figure 3.11: Three modes of growth molecules can follow from thermal evaporation depositions. (a) Volmer-Weber, (b) Frank-van der Merwe, (c) Stranski-Krastanov type growth. Image from [169].

If the molecule-molecule interaction is stronger than molecule-surface, the molecules will preferentially bond with each other rather than the surface. This causes the molecules to cluster and causes island growth. This process is Volmer-

Weber type growth and can be seen in Figure 3.11(a). The opposite effect is Frank-van der Merwe type growth, seen in Figure 3.11(b), where the molecule-surface interaction is stronger. This causes even layer growth, ideal for creating well-ordered films. The final type is Stranski-Krastanov type growth, seen in Figure 3.11(c), which is a middle ground between the two. The adsorbate begins to grow layer-by-layer, until a critical thickness where the molecule-molecule interactions begin to dominate and island growth begins, on top of the already formed even layers.

For the work conducted in this thesis, thermal evaporation is performed using a tube of borosilicate glass which contains the molecular powder. The tube has a tantalum wire coiled around it, which can heat the entire tube evenly by resistive heating. These molecular cells are in UHV conditions, so the mean free path of the molecule is greater than the cell to substrate distance. The gold substrates used in this work are first cleaned using sputter-annealing cycles in the UHV chamber. This involves three cycles of sputtering with argon gas at a pressure of 5×10^{-6} mbar for 20 minutes followed by an annealing step at 400 °C for 30 minutes. The deposition parameters for individual molecules will be detailed in the relevant experimental sections.

Chapter 4

Seebeck Polarity Inversion by Alkyne Co-Binding

4.1 Introduction

Measurement of the Seebeck coefficient of a molecular junction can provide information, not just on the thermopower performance of the molecule, but also about its electronic structure and method of charge transportation. For example, while I-V characteristics can be used to calculate the conductance of the molecule, and conductance-voltage (G-V) characteristics have even been shown to predict the magnitude of the Seebeck coefficient [170], information on whether the junction is p-type or n-type is lost [61, 140]. The position of the Fermi level of the electrode in relation to the HOMO and LUMO determines whether the junction is p-type (HOMO dominated) or n-type (LUMO dominated). While there can be disagreements over the predicted junction type [140], measurement of the Seebeck coefficient probes this property directly. Since the sign of the Seebeck is determined by the direction of the local gradient of the transmission function at the electrode Fermi level, from Equation 2.19, the polarity of the Seebeck coefficient shows which resonance dominates.

Achieving reliable control over the Seebeck polarity is important for thermoelectric devices, and should be considered in molecular design. However, as discussed in this chapter, molecular design alone is insufficient to accurately predict the experimental thermopower. The studied molecules, shown in Figure 4.1, have very similar electronic backbones and conductance values, yet Seebeck polarity inversions occur where they were not predicted by molecular structure alone.

The studied molecules are series of oligo(phenylene ethynylene) (OPE) derivatives with pyridyl anchor groups. Molecules **4A** and **4B** are designed with either one or two terminal alkynes, respectively, attached via propoxy arms, while **4C** is a cross-linked version where the alkynes connect two identical OPE backbones. The objective of this chapter is to understand how the competing anchoring interactions

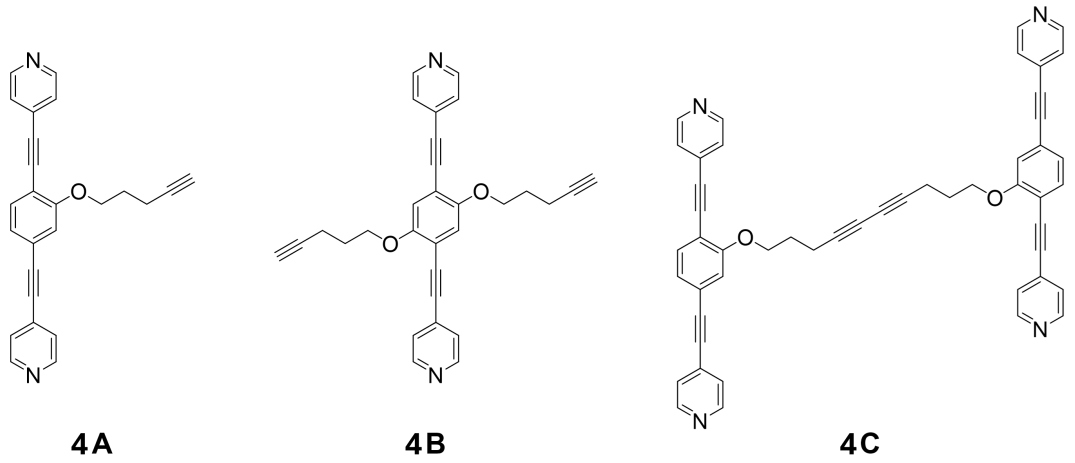

Figure 4.1: Structure of the molecules studied in this chapter.

affect the Seebeck coefficient. While anchor groups such as thiols and pyridines are typically assumed to dominate binding, additional substituents, especially flexible ones, may also interact with the metallic surface under certain geometries. Changes in molecular tilt or packing within a SAM can create conditions where such substituents are able to form secondary contacts with the surface, thereby altering the effective coupling pathway through the molecule-electrode interface. This study shows that, due to the sensitivity of the Seebeck effect to how electrons enter and exit the molecule, these secondary contact interactions can shift the transport orbital alignment enough to flip the sign of the Seebeck coefficient.

4.2 Methodology

4.2.1 Sample Preparation

Self-assembled monolayers of molecules **4A-C** were grown on template-stripped gold [171]. Powders of each molecule were dissolved and sonicated in chloroform to produce a solution with a 1 mMol/L concentration. For each molecule, the gold substrate was immersed in solution for a total of 1 hour while rinsing with chloroform every 15 minutes. The rinsing mid-deposition promotes the

desorption/re-adsorption process as described in Section 3.3.1. The deposition time of 1 hour was found to be sufficient to form a complete monolayer, as evidenced by QCM and the AFM images in Section 4.3.

4.2.2 XPS

XPS was performed using a Kratos Analytical AXIS Supra spectrometer with monochromatic Al Kα 1486.7 eV X-ray source, operating at 15 kV, 15 mA, and equipped with an electron gun for charge neutralisation. A pass energy of 40 eV was selected for spectra of N 1s and O 1s, while energies of 20 eV and 10 eV were selected for C 1s and Au 4f respectively. These values were chosen to optimise resolution against counts for each element measured. All spectra shown are charge corrected to the large C 1s peak centred at 284.8 eV. All the spectra were analysed using CASAXPS (Casa Software Ltd, UK).

4.2.3 AFM

All AFM measurements were carried out using a Bruker MultiMode 8 with a Nanoscope V controller in ambient conditions. Images were captured with PeakForce mode using NuNano Scout probes. These probes have a resonant frequency of 70 kHz and a spring constant of 2 N/m. Images were typically taken with a PeakForce setpoint of 300 pN and a scan rate ranging between 1-1.5 Hz. Conductive AFM data was collected using a Bruker TUNA module and Budget Sensors Multi75G probes. These are silicon probes coated with a conductive platinum layer.

4.3 Results and Discussion

After SAMs were made for each molecule by the method described in Section 4.2.1, both the prepared samples and the powdered form of the molecules were analysed by XPS. The wide spectra taken are shown in Figure 4.2.

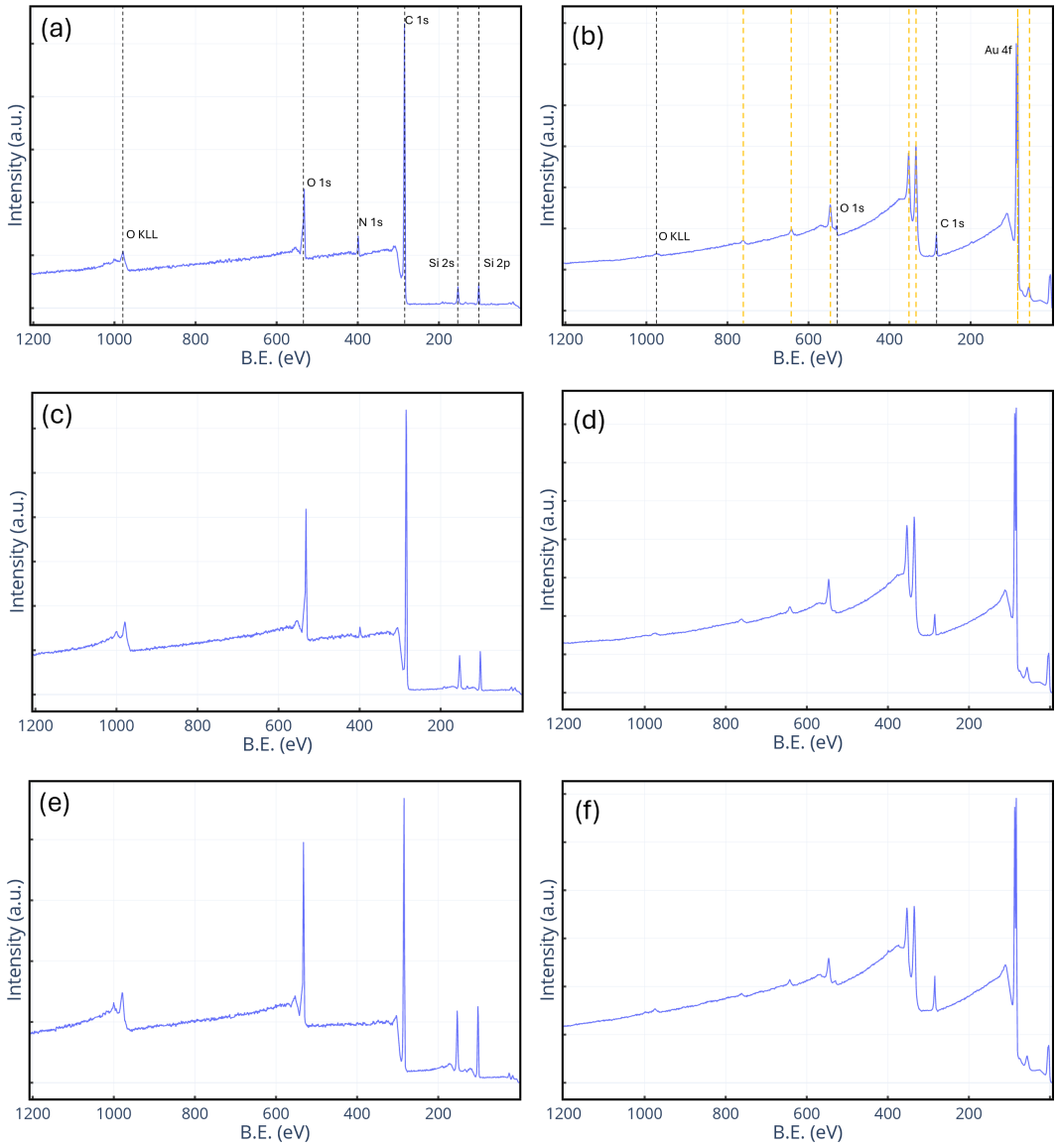

Figure 4.2: XPS wide spectra of powders (left column) and SAMs (right column). The investigated molecules are **4A** (a-b), **4B** (c-d) and **4C** (e-f). The main element peaks are labelled in (a) and (b) with the grey dotted lines. The yellow dotted lines in the SAM spectrum (b) represent all the peaks due to gold that appear across the spectra.

Molecules **4A-C** are comprised of mainly carbon with some nitrogen in the

pyridine anchors and oxygen in the propoxy arms. All of these elements are shown in the wide powder spectra shown in Figure 4.2. The silicon signal that is seen can be attributed to the adhesive in the carbon tape under the molecular powder [172]. In addition to silicon, the carbon tape will also add to the carbon and oxygen signals in the powder measurements. Note that the carbon and oxygen signals will be also inflated from adventitious carbon over the powders from exposure to air, and oxygen further increased due to the water layer that forms on surfaces in air too, although this addition will be small in comparison.

No additional elemental peaks can be seen, giving evidence for the purity of the molecules. This is also true for SAMs, so additional element contaminants have not been added to the surface during the assembly process. The gold signal dominates the wide spectra, so the layer must be thin. The oxygen peak is barely visible, further evidencing the lack of contaminants introduced. The oxygen peak here will be a combination of the molecule, as well as contributions from adventitious carbon and water layers, which is unavoidable when samples are prepared and transferred in ambient conditions.

High resolution spectra for the C 1s and N 1s regions give better insight into the formed SAMs. C 1s must always be investigated to be used as the reference for charge correcting, and comparison between the powder and SAM carbon spectra can give insight into changes the molecule may go through in the assembly process. The N 1s region is essential to monitor the formation of the SAM and is the main check that the SAM has assembled as intended. The results are shown in Figure 4.3.

In all the carbon spectra, there is a dominant C-C peak (orange) as expected. This is used as a reference and corrected to 284.8 eV. In every case there is a secondary peak (brown) at $\approx$ 286.0 eV. This is a combination of C-O and C-N

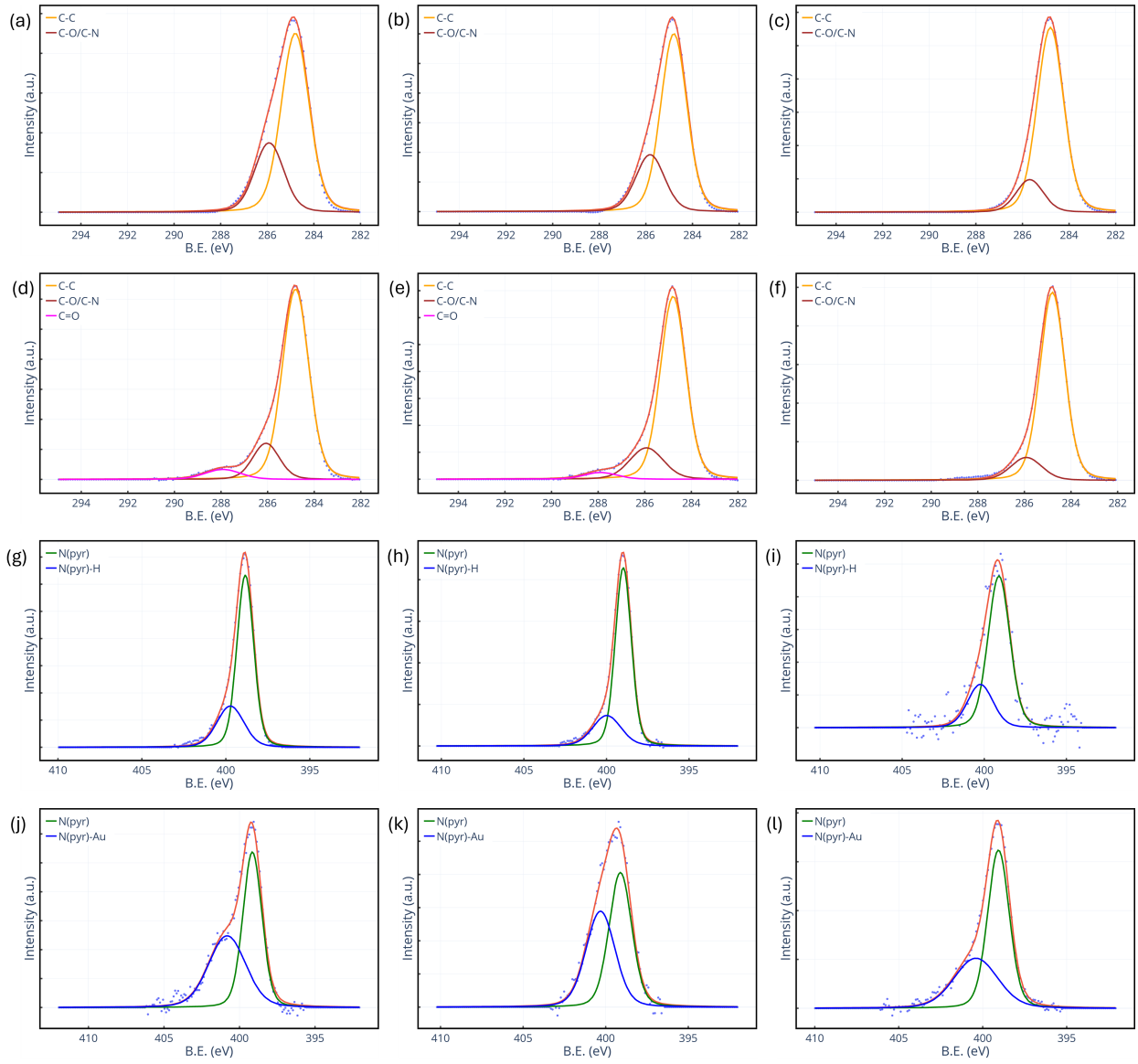

Figure 4.3: High resolution XPS spectra of the C 1s and N 1s regions. (a-c) C 1s region for the powder of molecules **4A-C**. (d-f) C 1s region for SAMs of molecules **4A-C**. (g-i) N 1s region for the powders of molecules **4A-C**. (j-l) N 1s region for SAMs of molecules **4A-C**.

contributions. Since both of these bonds appear at roughly the same binding energy, they cannot be distinguished between using standard XPS so are fitted as a single peak. This peak arises from the C-N bonds in the pyridine anchor and the C-O bonds in the propoxy arms, but will have contributions from the carbon tape adhesive in the

powder spectra and adventitious carbon in the SAM spectra. The third peak (pink) that arises for SAMs of molecules **4A** and **4B** (Figure 4.3d-e) at 288.0 eV is assigned to C=O and is thought to be caused from adventitious carbon [173]. Adventitious carbon does not form uniformly over a surface, and increases with exposure to air. So it is reasoned that the SAMs **4A** and **4B** were exposed for longer than SAM **4C**, or the regions measured had a particularly high coverage of carbon contamination. It should be noted there is some evidence of this peak beginning to form in the SAM **4C** spectra (Figure 4.3f) by a small bump at 288 eV in the raw data, which is represented by the blue dots, although not sufficient to fit as an independent peak.

In all the nitrogen spectra, there is a dominant peak at $\approx$ 399.0 eV (green). This is assigned pyridinic nitrogen [174], present in the anchor groups of each molecule. The secondary peak in the powder spectra (blue) is likely a shift due to hydrogenated pyridine. Due to air exposure, the water layer that forms can interact with the molecule. The nitrogen present in the pyridine can form a bond with a hydrogen within the water molecule [175]. This causes a shift in the binding energy to $\approx$ 400.2 eV [176,177]. Within the SAM, the secondary peak is assigned to N-Au as the anchor group in the molecule has coordinated to the gold substrate. This causes a shift of around 1.5 eV, slightly larger than that of hydrogenated pyridine [116, 176]. This peak is typically wider than the uncoordinated pyridine peak due to minor variations in possible binding sites and configurations, and possibly due to an effect of hydrogenated pyridine on the unbound side.

The area ratio between the two peaks gives the binding ratio for the molecules in the SAM. Since each of the studied molecules has an anchor group on both ends of the molecule, a perfectly formed SAM would have a binding ratio of 50%. Extra bound implies the molecules are lying down with both ends coordinating to the gold surface. Extra unbound implies additional growth on the surface from physisorbed molecules still present. The binding ratios for molecules **4A** and **4B**

(green and blue in Figure 4.3j-k) are both 48%. It should be noted that the bound signal will be slightly restricted by virtue of the binding pyridine being under the molecule. This causes attenuation of the intensity from Equation 3.1 which describes the intensity drop of photoelectrons originating from a given depth z. With this in mind, and perhaps some minor additional growth which is often unavoidable from manual rinsing, the binding ratio is considered acceptable of a well-formed SAM. The binding ratio for the SAM of molecule **4C** (Figure 4.3l) is 38%. However, the presence of two potential binding anchors adds additional complexity. The increased unbound signal could be due to comparatively more physisorbed material than the other two molecules, but it could also be due to a mix of binding configurations. If both legs consistently coordinated to the surface, a binding ratio of 50% would be expected. If only one leg consistently coordinates to the surface, the ratio should instead be 25%. The value of 38% implies a preference for both binding legs, but accepting the single binding leg if the packing or surface conditions did not allow for the second leg to connect.

Further investigation into the layer formation is conducted using AFM. Topographical images are taken in PeakForce mode. While the full extent of the packing quality can not typically be seen using AFM, especially in disordered SAMs like the ones studied here, it can provide good insight into surface coverage, extra growth and contamination. Additionally, a nanoscratch is performed [178,179]. A small scan size of 300-500 nm is selected and scanning proceeds in contact mode. A high setpoint equivalent to over 100 nN is selected as well as a rapid scan speed of 4 Hz. The region is scanned for 5 minutes, before returning to PeakForce mode with the usual topography parameters detailed in Section 4.2.3. Molecules are swept away from the area and the underlying gold surface is exposed. This allows for measurement of the SAM layer height as the difference in height between the inside and outside of the square that is formed. This procedure is conducted for each molecule, and the results are shown in Figure 4.4.

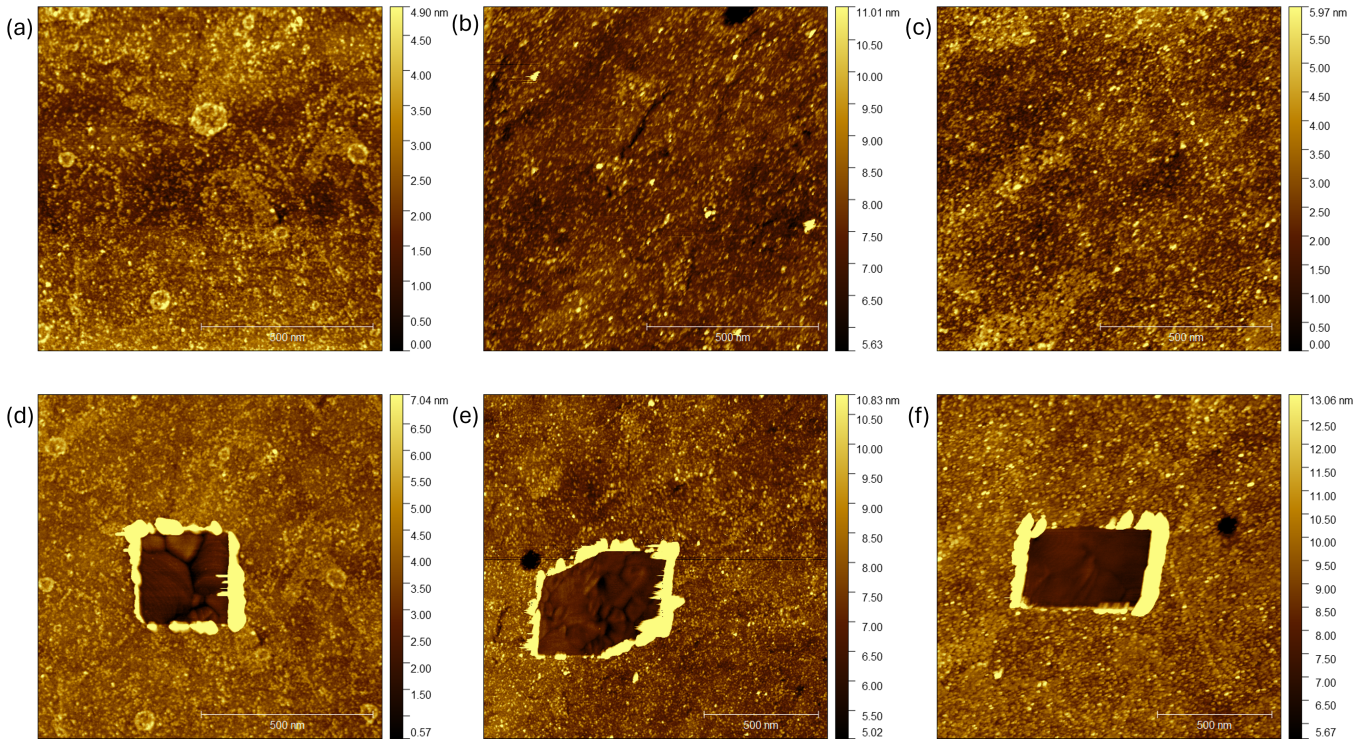

Figure 4.4: (a-c) Topography AFM images of molecules **4A-C**. (d-f) nanoscratches performed in the areas imaged above.

The topography AFM shows well formed SAMs with good surface coverage, although the SAM of **4B** may be less complete than the others from the increased number of apparent gaps in the layer (Figure 4.4(b) and (e)). Some minor areas of additional growth can be seen, but does not dominate any image. The gold surface, consistent with the typical form of template-stripped gold, can be seen in the centre of each of the nanoscratches, confirming a complete scratch. The tall features around the scratched areas are the "walls" of built up molecules which have been swept away. By masking everything outside of the square, a histogram of height values can be plotted to obtain an average value for the height inside the scratch. In order to get an accurate value for the average height of a molecule in the monolayer outside the scratch, the material on top of the monolayer should be masked out,

as well as the scratch and walls. This can be done by masking everything above a certain height within the image, however the chosen height is subjective. The scratch area is masked manually. In this thesis, masking heights have been chosen such that the mean value is roughly in the centre of the outside scratch histogram peak. The masked AFM images, and the histogram plots are shown in Figure 4.5.

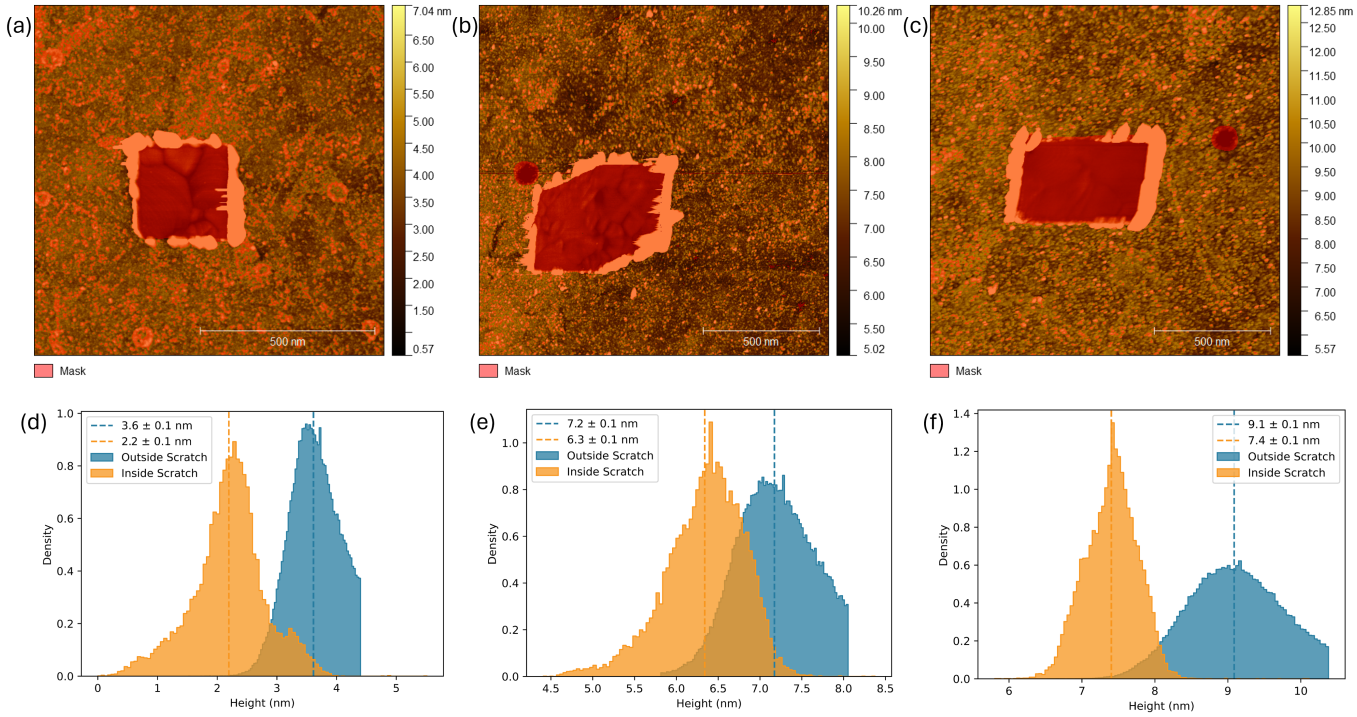

Figure 4.5: (a-c) The nanoscratch AFM images shown in Figure 4.4 with a mask applied to exclude additional growth from the height calculations. (d-f) Histograms showing the average height inside and outside of the scratch for molecules **4A-C**.

Taking the mean height value of the unmasked area outside of the scratch from the mean height value inside the scratch gives the average layer height. This is 1.4 ± 0.1 nm for molecule **4A**, 0.8 ± 0.1 nm for molecule **4B** and 1.7 ± 0.1 nm for molecule **4C**. Given the quantity of data used in each histogram, the standard error is lower than the noise floor of the AFM, which is calibrated to 50 pm. The noise floor value is therefore used, and added in quadrature to combine the two. The

stated errors are then rounded up to the significant figures of the mean height. Given the length of the molecule is 1.9 nm, this corresponds to molecular tilt angles relative to the surface normal of 42°, 64° and 28° for molecules **4A**, **4B** and **4C** respectively. It should be noted that the height of the SAM for molecule **4B** may be underestimated due to the potential incompleteness of the layer. Molecule **4C** tilts significantly less than the other two, likely due to the cross-linking between molecular backbones restricting tilt movements.

Conductance values were calculated for each of the SAM layers. The Bruker TUNA module, as described in Section 3.2.3.5, was used to collect over 10,000 I-V traces for the SAM of each molecule. At least four areas of each sample were probed during the measurements to ensure consistency across the sample. The individual areas are not static, however. While measuring each area, the probe will continuously drift across the surface. This means the junction being measured is constantly changing, including the molecules within the junction, number of molecules and binding configurations. A large quantity of data is therefore recorded for each area to average out the changes in the junction. The results are shown in Figure 4.6. The 2D histograms of the I-V traces include all of the data taken, after open-circuit and gold contact readings had been filtered out. Taking the gradient of the line at each point along the I-V trace gives a value for the conductance at the given bias. This is differential conductance, the results of which are shown in the G-V plots on the right of Figure 4.6. The average value at low bias is used to quote conductance values. In this thesis, the low bias regime used to give conductance values is between 0.15 V and 0.25 V. The junction conductance values for $\log(G/G_0)$ obtained from Figure 4.6 are -3.5 ± 0.6, -3.1 ± 0.6 and -2.8 ± 0.8 for molecules **4A-C** respectively. The uncertainties are calculated by the standard deviation of the histograms. A large variation in the I-V traces can be seen due to the inconsistency of the junction. With factors such as thermal drift and laser drift causing the molecules within the junction regularly change, there is a relatively large uncertainty in the final

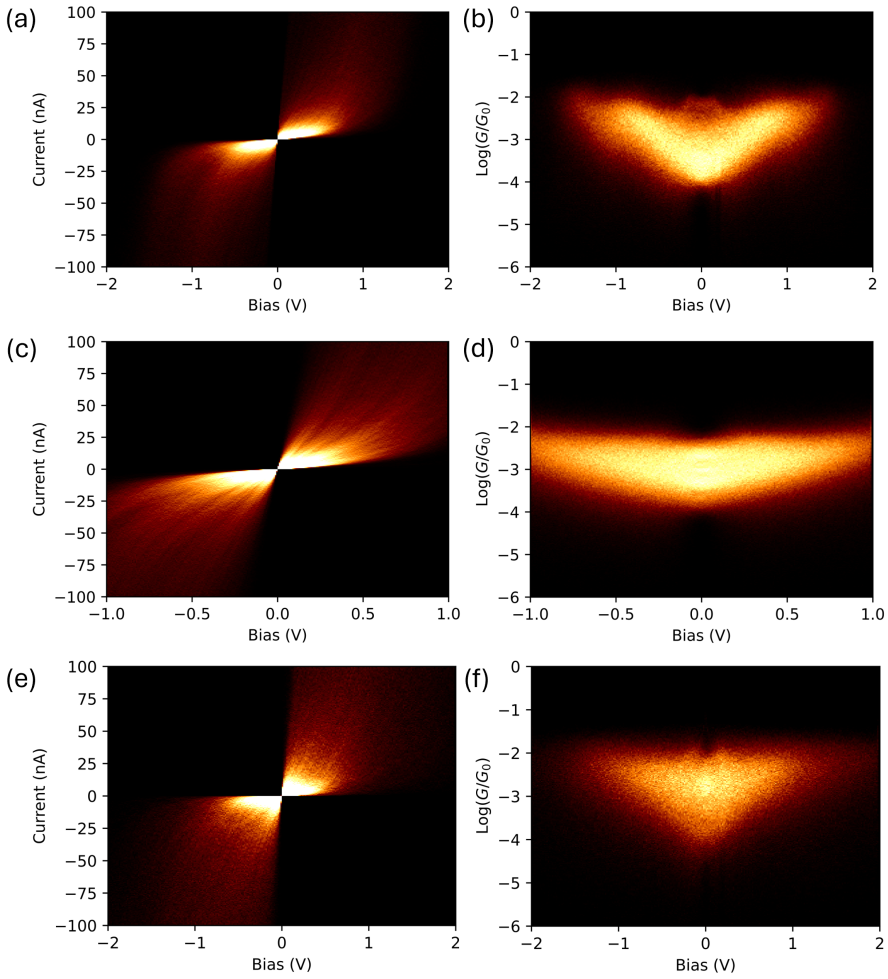

Figure 4.6: 2D histograms of all I-V traces (left column) and corresponding G-V plots (right column) for molecules (a-b) **4A**, (c-d) **4B** and (e-f) **4C**. Brighter areas represent more counts. Each plot is comprised of over 10,000 I-V sweeps with the open-circuit and gold contact readings filtered out.

conductance values. The obtained conductance values are all very similar, yet the thermoelectric properties vary significantly.

The thermoelectric properties were investigated by measuring the Seebeck coefficient of the SAMs for each molecule. Using the setup described in Section 3.2.3.6 and the same Budget Sensors Multi75 type probe as used for conductance measurements, the sample stage is mounted on a magnetic heater. While the probe is in contact

and heat is applied to the stage, the generated thermovoltage is measured. Between measurements, the probe is disengaged from the surface and at least 5 minutes is given to allow the surface to stabilise at the new temperature before re-engaging. During scanning, a 0 nm scan size is used and a resolution of 256 × 256 is selected. Two images of the collected thermovoltage are captured, resulting in over 130,000 data points taken for each temperature point. Measurements are taken between 40°C and 60°C in 5°C intervals. The results are plotted in Figure 4.7.

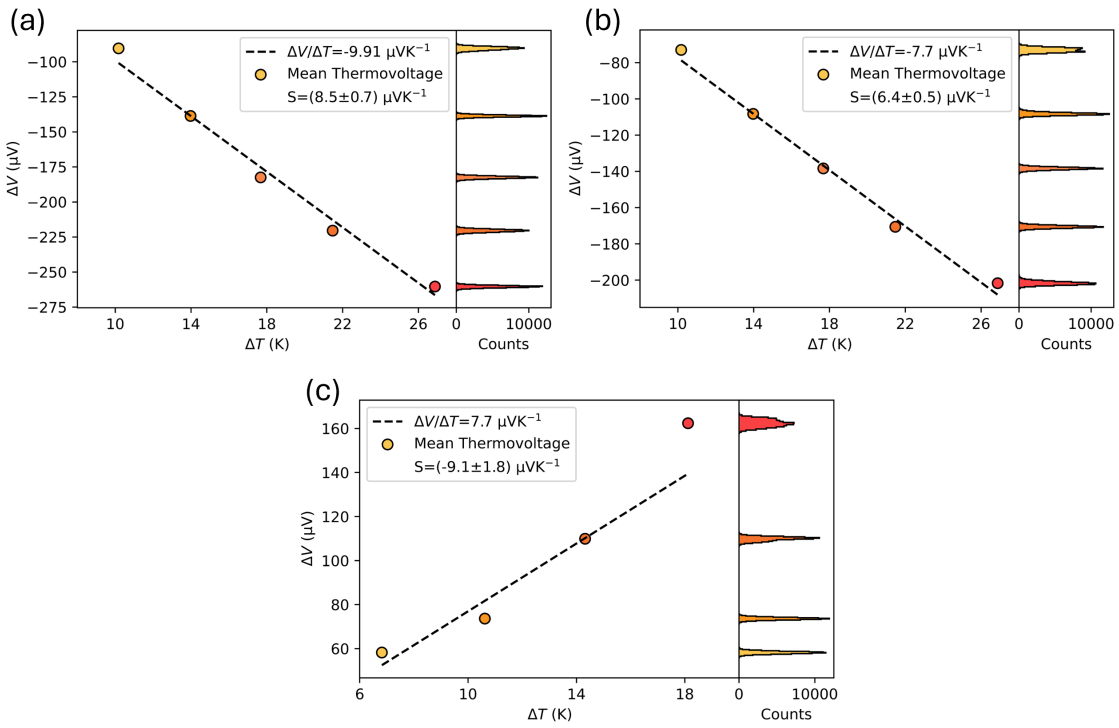

Figure 4.7: Plots of thermovoltage against temperature for (a) molecule **4A**, (b) molecule **4B** and (c) molecule **4C**.

In Figure 4.7, the temperature change stated on the x-axis is adjusted for calibration of the true temperature at the gold surface, since there is an offset between the temperature set on the heater and the temperature the reached at the gold surface. This offset is measured as the temperature increases during a calibration test, and the outcome is applied to all the temperatures plotted

for the SAM experiments. The measured gradient $\Delta V/\Delta T$ must be adjusted by a calibration clean gold sample. When measuring thermovoltage, each material involved in the electrical loop can contribute its own thermovoltage if subject to a temperature gradient. Measuring the Seebeck coefficient of a clean gold surface gives a calibration offset for the specific experimental setup which can then be applied to all future measurements taken using the same setup. This offset of $\approx 1.4\,\mu\mathrm{VK}^{-1}$ is applied to the gradients measured in Figure 4.7, then taking the negative gives the stated Seebeck coefficient value from Equation 2.6. The measured Seebeck coefficients are $(8.5 \pm 0.7)\,\mu\mathrm{VK}^{-1}$, $(6.4 \pm 0.5)\,\mu\mathrm{VK}^{-1}$ and $(-9.1 \pm 1.8)\,\mu\mathrm{VK}^{-1}$ for molecules **4A-C** respectively. Given the number of data points for each temperature, since none of the histograms overlap, there is little doubt over the polarity of the measured Seebeck coefficient for each molecule. This was a surprising result, as the similarity of the molecular backbones and identical anchor groups suggests each molecule should have the same sign of Seebeck.

Density functional theory (DFT) carried out by collaborators to model the electrical transport characteristics in single molecule junctions suggested that each molecule should exhibit LUMO dominated behaviour and appear n-type. Since the Seebeck coefficient is proportional to the negative of the slope of $\ln T(E)$ at the Fermi energy of the electrode, from Equation 2.19, a negative Seebeck coefficient is expected for LUMO dominated junctions. Experimentally, only molecule **4C** showed this behaviour. The simulated transport trends containing the frontier orbitals are shown in Figure 4.8.

The predicted arrangement, as shown, is a contact point by the anchor group on either end of the molecule. That is, one contact is the coordination of the bottom anchor to the gold electrode and the other is the top anchor contacting with the platinum AFM probe. This results in the Fermi energy of the electrode, highlighted by the dotted lines in Figure 4.8, resolving very close to the LUMO of the molecule

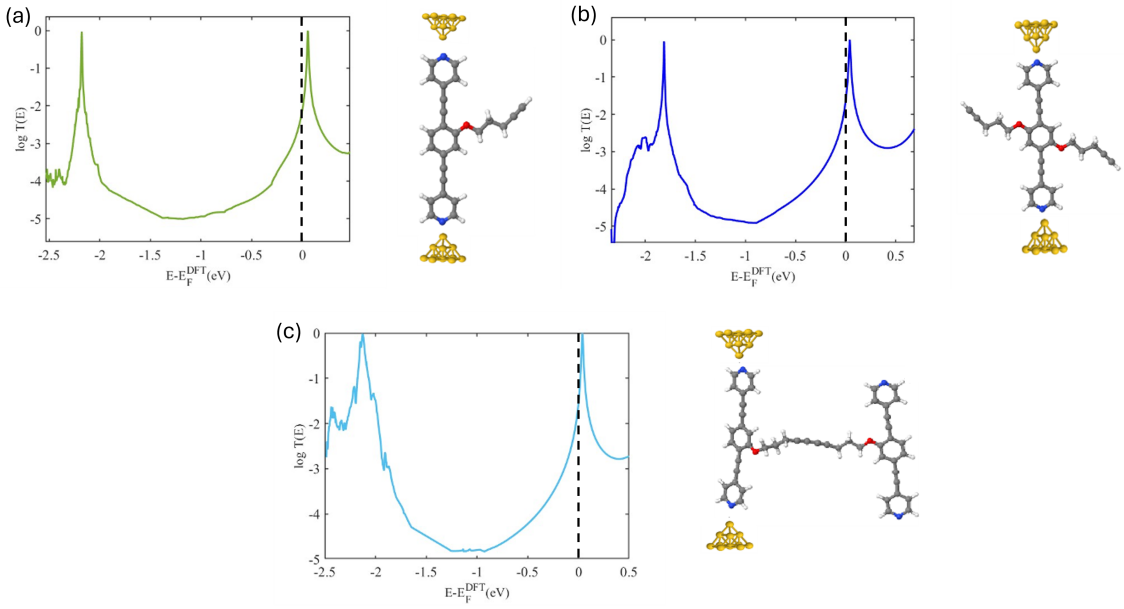

Figure 4.8: DFT simulated transport of molecules (a) **4A**, (b) **4B** and (c) **4C**. In each case, the contact points chosen are the anchor groups at the top and bottom of the molecule, as shown in the images next to the plots. The dotted line indicates the Fermi level of the electrodes. Data courtesy of Colin Lambert.

in a stable junction. This is true for the case of each molecule, so it is predicted Seebeck coefficients should be similar in both polarity and magnitude.

It is hypothesised that the cause of this discrepancy is an additional surface contact from the alkynes. Molecules **4A** and **4B** have one or two terminal alkynes on flexible propoxy arms, respectively, whereas molecule **4C** does not. Molecule **4C** can therefore act as a control where, given that the molecules are standing which both AFM and XPS strongly support, the only possible contact points to the gold electrode are by the intended pyridyl anchor groups. From AFM, the height of the SAM layer for molecules **4A** and **4B** are less than that of **4C**, implying a greater molecular tilt angle. It is reasoned that, given the additional space from the SAMs not being in an ordered and packed formation, it is energetically favourable for the molecule to create an additional surface contact through the alkyne arms, facilitated

by an increased tilt of the molecule.

This change in interaction with the gold electrode interface dramatically changes the transport properties of the junction. This was an unprecedented shift for an unintended additional contact, which has a significantly weaker interaction with the gold electrode than the pyridyl anchor. Yet the additional electron pathway shifts the molecular orbitals such that the junction becomes HOMO dominated, changing it from n-type to p-type. This is supported by extra DFT calculations carried out by collaborators to test the hypothesis. The results are shown in Figure 4.9.

The predicted shift in the transmission function when incorporating the co-binding terminal alkyne now agrees with the experimental data, as shown in Table 4.1. Not only do the junctions become HOMO dominated, but the transmission gradients resolved at the Fermi energy are more shallow. While molecule **4A** is still close to a frontier orbital, molecule **4B** lands in the centre of the HOMO-LUMO gap. Both have a reduced magnitude than originally predicted in Figure 4.8 with only anchor binding. This is reflected in the experimental results.

Molecule	Theoretical DFT S(μV/K^{-1})	Experimental S(μV/K^{-1})
4A	12.6	8.5 ± 0.7
4B	11.9	6.4 ± 0.5
4C	-14.0	-9.1 ± 1.8

Table 4.1: Table of results of the DFT calculations using the new binding configurations compared to the experimentally obtained values.

In each case, the experimentally obtained values have a smaller magnitude than the predicted values, as expected for a SAM measurement as opposed to an idealised single molecule junction, mainly due to variations in molecule-electrode coupling

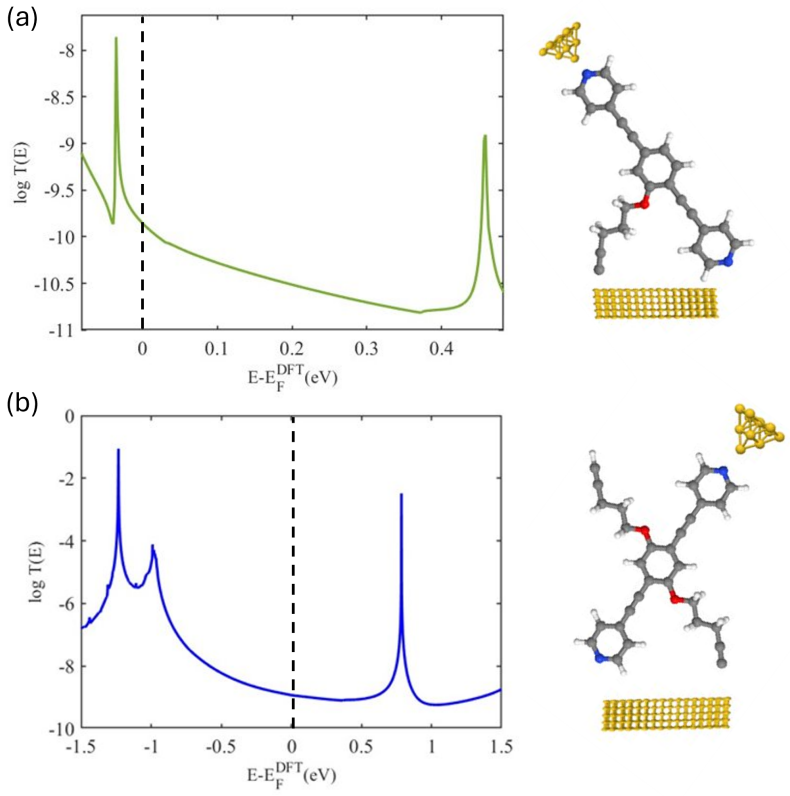

Figure 4.9: DFT simulated transport of molecules (a) **4A** and (b) **4B**. The contact points chosen are the bottom pyridyl anchor and alkyne arm to the bottom electrode, and the top pyridyl anchor to the top electrode, as shown in the images next to the plots. The dotted line indicates the Fermi level of the electrodes. Data courtesy of Colin Lambert.

within the junction. Molecule **4C** has the largest magnitude and expected negative Seebeck coefficient. This acts as a control to confirm the validity of the original DFT calculations with only anchor group connections, since this molecule has no other possible configurations. The experimental results for Molecule **4A** and **4B** agree with the amended DFT calculations which include an additional alkyne co-binding configuration. Both Seebeck coefficients become positive as the junction becomes HOMO dominated. The magnitudes of both drop compared to the original prediction as neither Fermi level is on a steep slope close to a resonance as before. However, the Seebeck coefficient of molecule **4A** is greater than that of **4B**, by virtue

of the Fermi level being closer to the HOMO resonance, increasing the gradient of the transmission function. This strongly supports the idea that terminal alkyne co-binding is occurring, and such an interaction can dramatically change the electrical properties of the system, in this case changing the junction from n-type to p-type.

4.4 Conclusions and Future Work

SAMs of molecules **4A-C** were grown on a template-stripped gold substrate, exhibiting close to 50% binding for molecules **4A-B** and 38% for molecule **4C**, which was likely due to an inconsistency in the number of anchors regularly binding to the surface, and more physisorbed material. Each layer had a similar low bias conductance measured, yet the thermoelectric properties were vastly different. Contrary to initial DFT calculations, the Seebeck coefficient was not negative in each case. Rather, molecules **4A** and **4B** exhibited a positive Seebeck coefficient, while the Seebeck coefficient of molecule **4C** was negative as expected. This inversion effect of the Seebeck coefficient is thought to be due an additional surface interaction arising in molecules **4A** and **4B** from alkyne co-binding. The molecule seems to tilt to allow the arm group to contact the gold surface, as evidenced by the smaller layer height in the AFM measurements compared to that of molecule **4C**. Revised DFT calculations show a similarly large shift in the Seebeck coefficient when including the additional surface interaction. The trend of the theoretical Seebeck values for each molecule matched that of the experimentally measured values, evidencing the occurrence of alkyne co-binding. The dramatic shift in shape of the transmission function was unprecedented for such an interaction, and resulted in the junction changing from n-type to p-type. Knowledge of the thermoelectric sensitivity of a molecule to its surface interaction can be used to greatly improve designs which may otherwise show little potential. While in this case, the Fermi level has shifted away from resonances in the transmission function, minor changes to the surface interaction for other molecular systems may shift a mid-gap Fermi level closer to

a resonance. This unlocks new potential to improve future molecular designs, or even affect the output from existing designs by altering binding configurations from deposition method, for example.

Future work for these molecules includes the possibility of cross-linking molecules **4A** and **4B** on the surface. With the use of halogens on the ends of the arm groups, it may be possible to cross-link the molecules together with the application of heat. Such an on-surface reaction should create a far more robust layer, improving the stability of the molecular junction during measurements. Additionally, this could be a method to induce a separation of the arm group from the gold surface. Following confirmation of a cross-linked layer, the Seebeck coefficient polarity should invert back to negative since the additional surface interaction has been removed. This would serve as further strong evidence for the proposed inversion mechanism.

Chapter 5

Memristive Behaviour in Edge-Fused Porphyrin Dimers

5.1 Introduction

As described in Section 2.6, a memristor acts as a form of non-volatile memory. The conductance of the material can switch reproducibly and reversibly between at least two stable states, and be stable without external influence. While research into the potential for organic molecule memristors is ongoing, there exists a knowledge gap between promising candidates in single molecule break-junction experiments, and integration into larger-scale practical devices. This chapter focusses on one molecule, shown in Figure 5.1, which has previously demonstrated promising memristive properties.

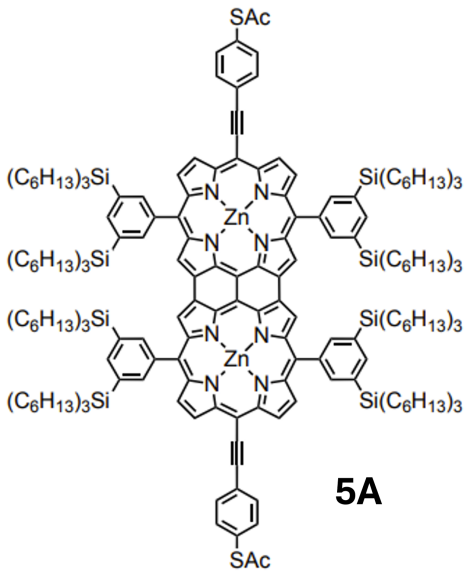

Figure 5.1: Structure of the molecule studied in this chapter.

Molecule **5A** is one of a series of edge-fused porphyrin oligomers which showed surprising electrical properties. The conductance of the molecules was shown to be unchanged with length and increases substantially under bias [180]. For coherent transport, conductance generally decays exponentially with length, governed by the decay constant, β, from Equation 2.26. The series of porphyrin oligomers

demonstrated values for β close to zero, or even negative. This arises due a rapid narrowing of the HOMO-LUMO gap with length. Retaining a good conductance with length allows for improved measurement of electrical properties despite the molecule's size, in this case 3.2 nm. This molecule has already shown memristive behaviour when investigated as a single molecule in STM break-junctions [181, 182]. In these studies, the length of the porphyrin tape increases up to 8 edge-fused porphyrins in a single molecule. It is shown how increasing length improves the consistency of memristive switching and creates strikingly high conductance values at high bias.

Redox switching has been observed in similar systems [183] and is believed to be the primary switching mechanism here too. For the porphyrin tape molecules, including molecule **5A**, both the HOMO and the LUMO exhibit strong coupling to the electrodes and determine the conductance. However, spatial localisation patterns of the HOMO-1 show a very weak coupling. It is therefore reasoned that redox switching is occurring through the HOMO-1 orbital, where after an initial oxidation from an applied bias over a certain value, the state becomes trapped and the system relaxes around it. This state can be long-lived after the bias is removed. In this study, the conductance was found to retain a two order of magnitude change for as long as 10 s [181]. As the length of the porphyrin tape increases, the HOMO-LUMO gap decreases. The HOMO-1 orbital also gets shifted towards the Fermi energy, so the energy barrier to trigger a redox switch is reduced. This aligns with the experimental data Deng *et. al.* gathered [182].

More recently, SAMs of the porphyrin tapes up to N = 3, including molecule **5A** (N = 2), have been grown and investigated [184]. These junctions were formed on template-stripped gold and were measured using an eutectic Ga-In (EGaIn) probe. These probes typically have a diameter of over 1 μm and are coated with a natural oxide layer [185]. The oxide layer is insulating, with an average thickness of ≈ 0.7 nm,

but does not grow uniformly [186]. The SAMs of the N = 2, 3 porphyrin tapes both exhibited switching behaviour. In the paper, it is discussed that a fraction as small as 10^{-4} of molecules in the junction formed by EGaIn contribute to the tunnelling through the junction [187]. It is then theorised that some molecules which are not strongly coupled to both electrodes build up a net positive charge, and it is these charged molecules which effectively gate the transport through the neutral conducting molecules, reducing the conductance. It is reasoned that the charged molecules are stabilised by relaxation within the layer, governed by ion-induced dipole interactions between molecules. These interactions are stronger with the length of the molecule, which would result in the longer porphyrin tapes producing a more stable and consistent conductance switching junction, which is reflected in their experimental results [184]. The aim of the experiments in this chapter are to recreate these results with molecule **5A**, but using a metal AFM probe as a top electrode instead of EGaIn. The intention is to provide additional information to the possible switching mechanisms, investigate if the oxide layer present in EGaIn is necessary to stabilise the switching junctions in SAMs, and ensure the results are repeatable.

5.2 Methodology

5.2.1 Sample Preparation

Self-assembled monolayers of molecule **5A** were grown on template-stripped gold [171]. The molecular powder was dissolved and sonicated in toluene to produce a solution with a 0.05 mMol/L concentration. The majority of depositions took place over a 24 hour period in a nitrogen atmosphere within a glove box, the exceptions are clearly stated. The deposition time was chosen based on previous experiments using the same molecule [184]. After the deposition, samples are rinsed in toluene by repeated dipping, before being taken out and dried with nitrogen gas. To perform XPS measurements on the powder, some of the solution is drop cast on a silicon

oxide surface and allowed to dry.

5.2.2 XPS

XPS was performed using a Kratos Analytical AXIS Supra spectrometer with monochromatic Al Kα 1486.7 eV x-ray source, operating at 15 kV, 15 mA, and equipped with an electron gun for charge neutralisation. Pass energies of 20 eV and 10 eV were selected for C 1s and Au 4f respectively, while 40 eV was selected for the other elements measured, that is Zn 2p, O 1s, N 1s and S 2p. These values were chosen to optimise resolution against counts for each element measured. All spectra shown are charge corrected to the C-C peak centred at 284.8 eV. All the spectra were analysed using CASAXPS (Casa Software Ltd, UK).

5.2.3 AFM

All AFM measurements were carried out using a Bruker MultiMode 8 with a Nanoscope V controller in ambient conditions. Images were captured with PeakForce mode using NuNano Scout probes. These probes have a resonant frequency of 70 kHz and a spring constant of 2 N/m. Images were typically taken with a PeakForce setpoint of 300 pN and a scan rate ranging between 1-1.5 Hz. Conductance data was collected using a Bruker TUNA module and Budget Sensors Multi75G probes. These are silicon probes coated with a conductive platinum layer.

5.3 Results and Discussion

5.3.1 Powder Analysis

XPS of the molecular powder is an important comparison point for results of the SAM XPS data. Since there was not sufficient powder available to pour directly onto a sample plate, a portion of the dissolved solution was drop cast onto a silicon-oxide surface and allowed to dry. This provided a sufficiently thick region of pure powder

to carry out the XPS measurements, although the silicon and oxygen signals are likely inflated in the results due to the surface. The results are shown in Figure 5.2.

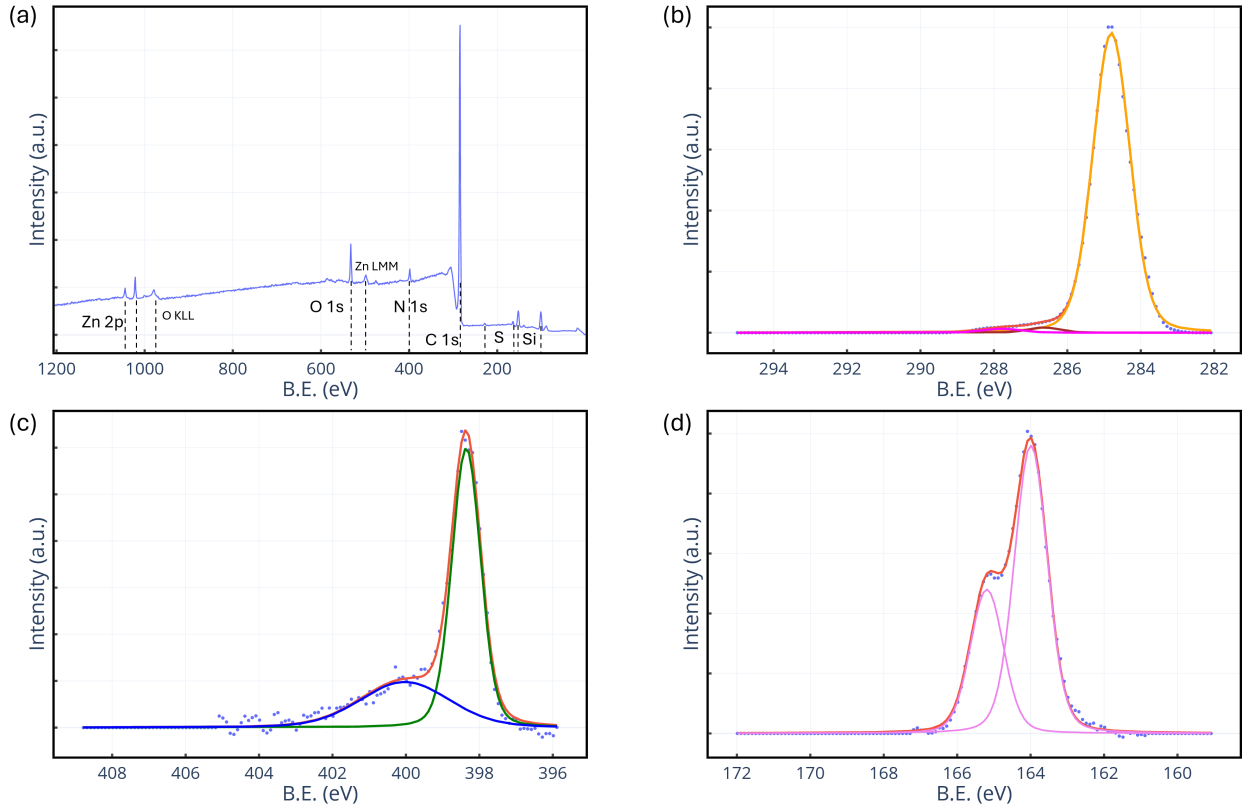

Figure 5.2: XPS spectra of the powder of molecule **5A**. (a) Wide spectra with the main element peaks labelled with black dotted lines. High resolution spectra is also shown for the (b) C 1s region, (c) N 1s region and (d) S 2p region.

The wide spectra of the powder shows the expected elemental peaks for the molecule. As seen in Figure 5.1, the majority of the molecule is carbon. There are two zinc porphyrins in the molecule, which each contribute a zinc atom and four nitrogen atoms. The thioacetate (-SC(=O)CH_3) anchor groups each contribute a sulphur and oxygen atom. A total of eight silicon atoms are present in the solubilising ligands. This accounts for every elemental peak in the wide XPS powder spectra, with no expected elements omitted.

The carbon spectra, Figure 5.2b, shows a large C-C peak (orange), used as the reference and set to 284.8 eV. The second peak (brown) is small and centred at 286.5 eV. This is assigned to C-N and originates from the nitrogen in the porphyrins. The third peak (magenta) at $\approx$ 288 eV is assigned to the C=O that is present in the thioacetate anchor groups.

The nitrogen spectra, Figure 5.2c, shows a sharp, large peak centred at $\approx$ 398.3 eV (green). This is typical of nitrogens within a metal centred porphyrin. A free-base porphyrin expects to have two roughly equal N 1s peaks, one around 397.2 eV assigned to =N- and one around 399.2 eV assigned to -NH-. Upon a metal entering the centre, this collapses to a single peak between the two originals, the exact energy depending on the metal [188]. The large peak in this nitrogen spectra is reasonable for a zinc-centred porphyrin [189]. However, there is also an unexpected secondary peak seen centred at 400 eV (blue). This peak is unexpected and unusually wide. It has been previously thought a secondary peak around this energy for a molecule containing zinc porphyrin is due to intermolecular interactions [190]. The broadness of the peak implies some inconsistent shifting due to a range of possible interactions, lending to the idea that it is caused by the porphyrin backbones interacting with parts of adjacent molecules.

The sulphur spectra, Figure 5.2d, shows a single doublet providing a good fit for the data. The doublet is fitted using the fixed parameters of $\Delta E = 1.2$ eV and halved area, as described in Section 3.1.3. When referencing a doublet position, the centre of the larger S $2p_3/2$ peak position is stated. In the case of the powder, there is a single doublet at 164.0 eV which can be assigned to the sulphur within the protected thioacetate. This is useful to compare with the more complex sulphur spectra in the SAMs, as this binding energy position should not shift for the protected thioacetates.

5.3.2 SAM analysis

SAMs of molecule **5A** were created by the method detailed in Section 5.2.1. Six samples were created this way, with care taken to replicate method and exposure time in air before measurements. After deposition in a nitrogen atmosphere and drying, samples are taken to the XPS where they are loaded onto a sample bar and placed into the load-lock which is rapidly pumped to a rough vacuum before reaching UHV after around an hour. The total exposure time to air for each sample before entering the XPS, including the drying step, was under 5 minutes. Of note, the first five samples were created using the same solution. The deposition of sample 5 was carried out after the solution was bubbled through with nitrogen gas for 15 minutes before being placed back in the glove box. Sample 6 was grown with a newly made solution.

C 1s spectra shown in Figure 5.3. In each case, the large C-C peak (orange) is used as the reference to 284.8 eV for the sample. The secondary shoulder peak (brown) is present in each and is assigned to a combination of C-N and C-S [191]. This peak is especially large and broad in samples 2 and 5 (Figure 5.3b and e). The full-width half-maximum of these peaks as fitted are 1.9 eV and 1.6 eV respectively. This could be an indication of extra contaminants on the surface, since the C-O peak overlaps with C-N and C-S, so would add some breadth. C-O is a common contaminant that could arise from additional adventitious carbon, for example, or contamination in the SAM itself. Samples 4 and 6 also exhibit a broader second peak, with full-width half-maximums of 1.7 eV and 1.6 eV respectively. For comparison, the full-width half-maximums of samples 1 and 3 are 1.2 eV and 1.0 eV respectively. This indicates that samples 4 and 6 still have extra C-O components, just less than samples 2 and 5. Samples 1 and 3 are relatively clean by comparison, further evidenced by a clearly reduced oxygen signal in the wide spectra of the SAMs, shown in Figure 5.4. The third carbon peak (magenta), assigned to C=O, should be a measure of the quantity of protected anchor groups still present on the surface, as the thioacetate

group is the only source of C=O within the molecule. Samples 1 and 3 show a clear third peak at $\approx 287.5\,\text{eV}$, while it is much smaller for the other samples. However, since there is no correlation between this finding and the binding percentage shown in the sulphur spectra, no clear conclusions can be drawn from this.

The wide spectra shown in Figure 5.4 indicate a well formed thin SAM. In comparison to the powder spectra, all the expected elemental peaks appear with no irregularities of additional elements. The quantity of oxygen can be seen to vary across samples, with samples 1 and 3 having the least as previously discussed. The oxygen in sample 5 also appears relatively low, likely due to the bubbling of nitrogen gas prior to sample deposition. While the zinc and sulphur signals can barely be distinguished from the background due to the dominance of the gold peaks, both are still present. The silicon peak is more pronounced in samples 4 and 6, although the sulphur and zinc peaks are not, indicating this is may not be due to presence extra molecule on the surface. Caution should be taken when analysing silicon signals on a template-stripped gold surface, as the gold is glued to a silicon substrate. Any cracks or holes in the gold surface within the x-ray beam spot will add to the silicon signal detected.

High resolution S 2p spectra, shown in Figure 5.5, reveals the expected mix of bound/protected species, but gives additional insight into binding configurations. Across all samples, there is a doublet peak at a higher binding energy (light pink) which is centred between 163.3 eV and 163.8 eV. This is assigned to unbound sulphur, where the thioacetate is still in its protected form. This is in broad agreement with the single doublet found in the powder spectra. Once a thioacetate comes into contact with gold, the acetyl group is cleaved and a thiolate is formed. The partially reduced sulphur in the thiolate has a lower binding energy of $\approx 162.0\,\text{eV}$ [110]. This appears as the largest doublet (grey) in all six samples, with central binding energies ranging from 161.9 eV to 162.3 eV. There is, however, a second doublet at even lower

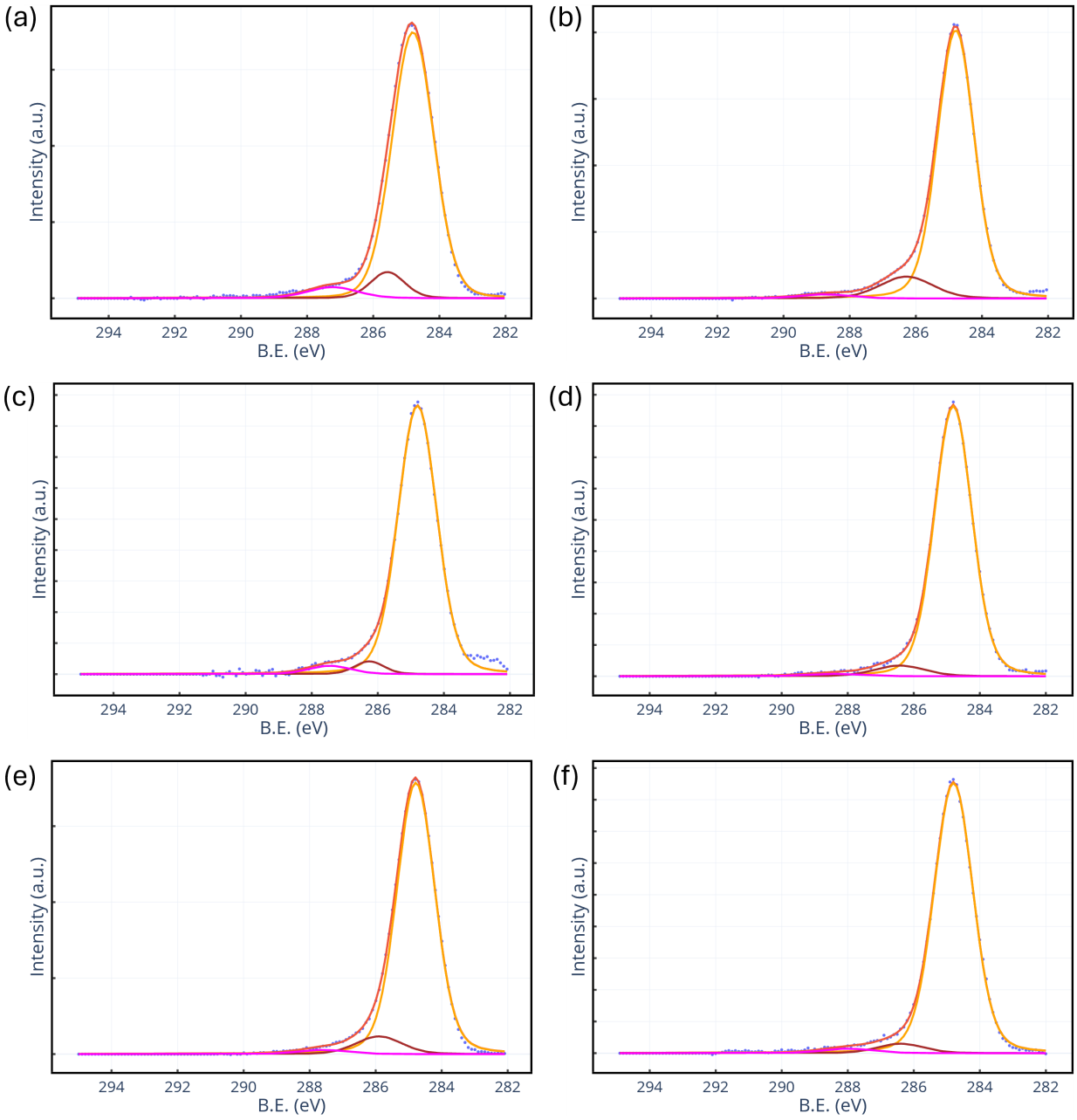

Figure 5.3: High resolution XPS spectra of the C 1s region for samples 1-6, labelled a-f respectively.

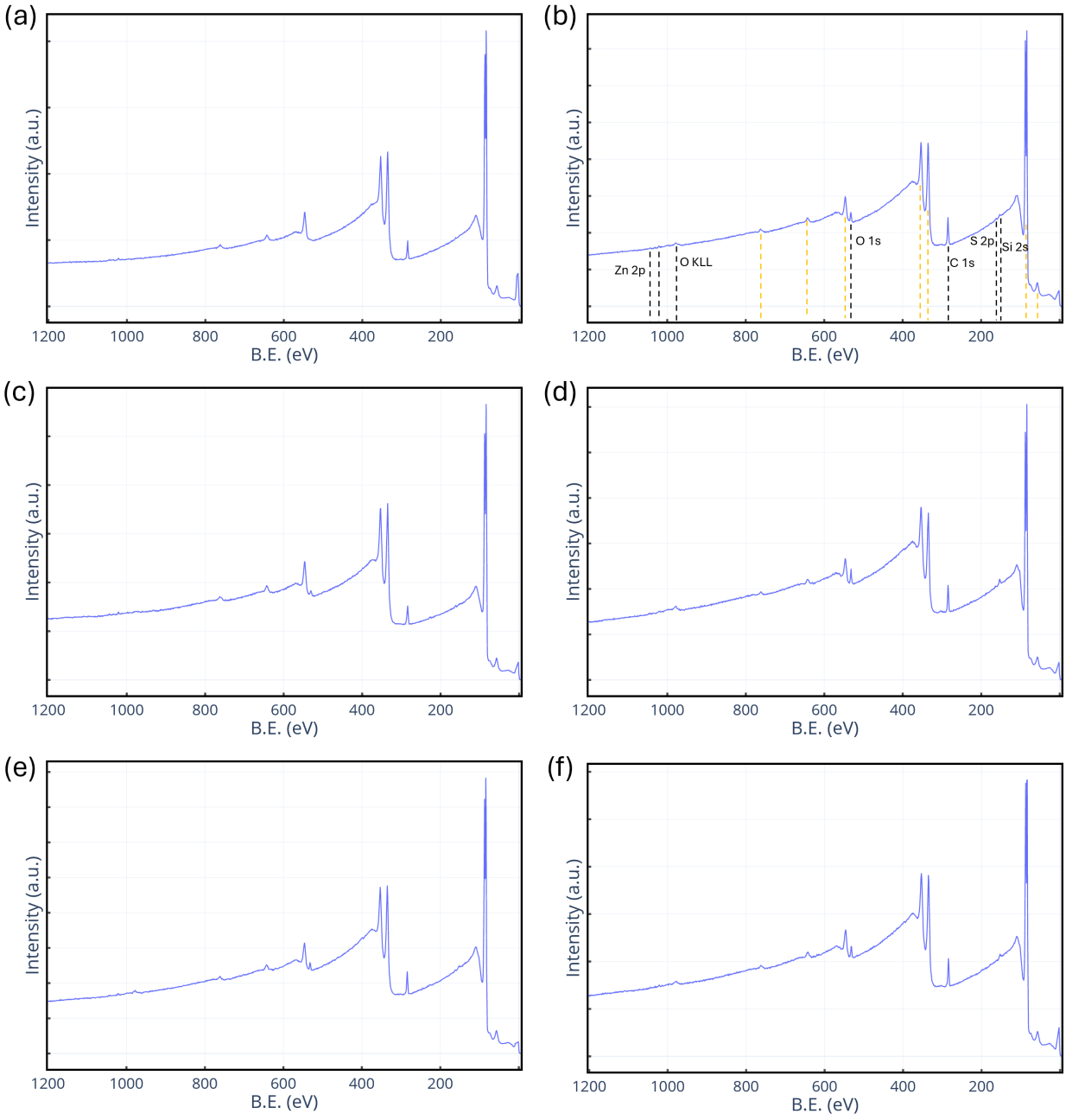

Figure 5.4: Wide XPS spectra for samples 1-6, labelled a-f respectively. The main element peaks are labelled with black dotted lines in (b) as an example. The peaks due to gold are indicated with yellow dotted lines.

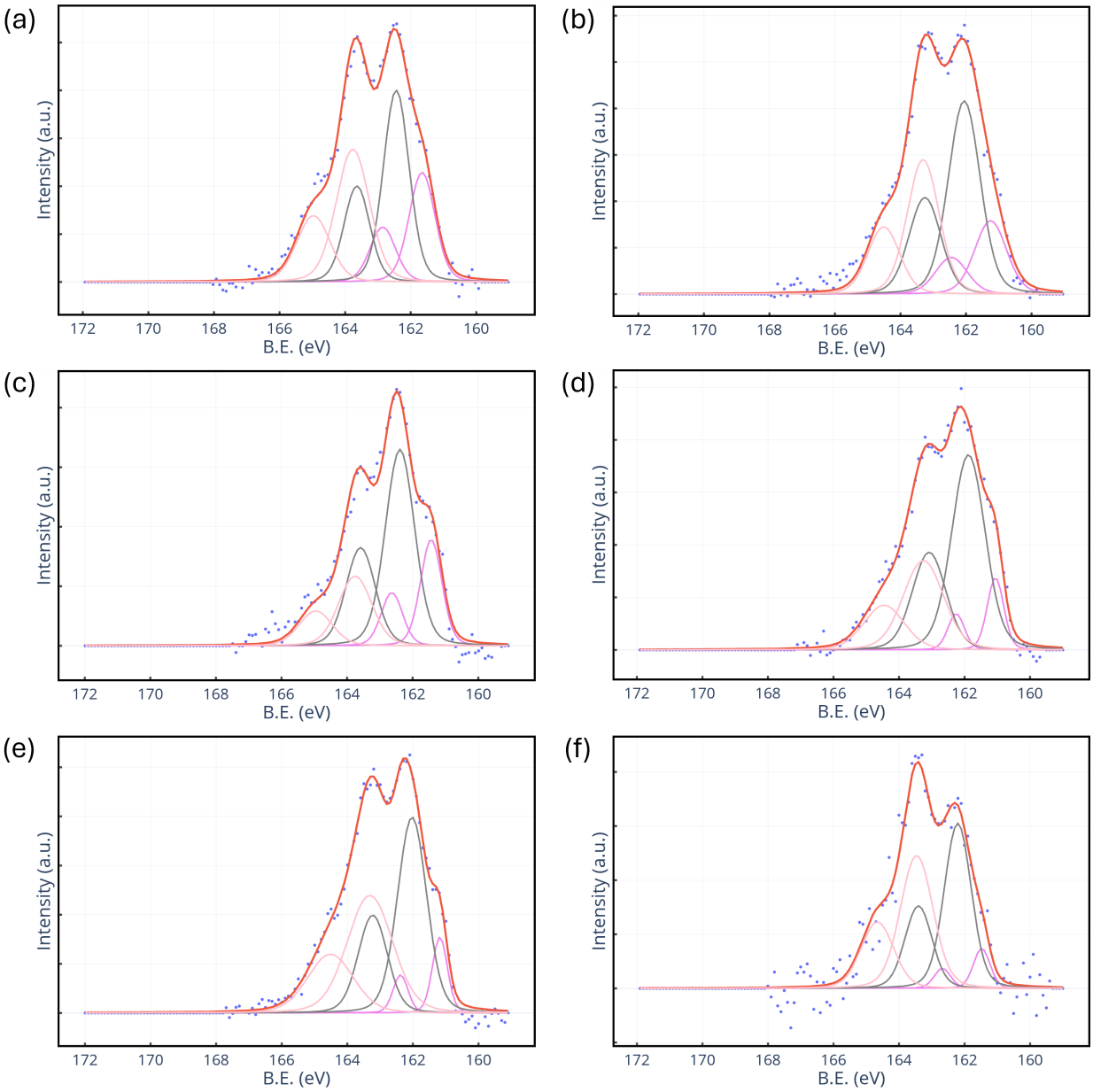

Figure 5.5: High resolution XPS spectra of the C 1s region for samples 1-6, labelled a-f respectively.

binding energy (violet) representing a different binding configuration. This shoulder is especially pronounced in samples 3, 4 and 5 (Figure 5.5c-e) but is present in each case. Even in the samples without the well defined shoulder, the peaks cannot be fitted correctly with just two doublets. The envelope does not properly fit the measured data and the protected signal gets shifted to an unrealistically low binding energy which no longer agrees with the powder spectra. This secondary binding doublet must therefore be real and explained.

Across the six samples, this doublet occurs at centre energies ranging from 161.1 eV to 161.5 eV. It has been observed that sulphur groups bound by step edges or defects carry a slightly more negative charge than those on terrace sites [192]. This would cause a reduction in binding energy due to additional screening of the nucleus. Studies which show additional sulphur peaks at similarly low binding energies assign them to an *sp* binding configuration as opposed to the sp^3 configuration which typically occurs in thiolate binding [193]. Thiols tend to bind to a gold surface using gold adatoms. Forming a bond with one or two adatoms occurs in an sp^3 configuration for either atom-top or bridge site binding. The alternative is to bond with three gold atoms in a hollow site, which takes an *sp* configuration [145]. Hollow site binding is more stable and exhibits a lower binding energy so is favourable during early stages of SAM formation, but is sub-optimal for full layer growth as the bonds are too rigid and cannot easily be adjusted to account for efficient packing of neighbouring molecules. Therefore, during the SAM reorganisation phase, atom-top bonds dominate the overall SAM layer and promote dense packing of molecules, eventually leading to a single sulphur binding doublet [193]. However, it can be reasoned that due to the nature of template-stripped gold being rough, with a high number of surface defect sites compared to an atomically flat Au(111) substrate, hollow site binding can occur more frequently. This is because there will be more hollow sites available and the SAM will be less ordered on the surface than it would be on an Au(111) substrate.

Sample #	Atom-Top Binding %	Total Binding %
Sample 1	78%	65%
Sample 2	72%	66%
Sample 3	72%	77%
Sample 4	84%	68%
Sample 5	83%	56%
Sample 6	87%	54%

Table 5.1: Table of binding percentage in each sample. The atom top binding % was calculated as the area under the grey peak against the total area under the grey and violet peaks. The total binding % was calculated as the area under the grey and violet peaks against the total area under the envelope.

The binding ratios for each sample are shown in Table 5.1. As expected, the atom-top binding configuration is far more common. However, rather unexpectedly the binding percentage is consistently over 50%. For an ideal SAM, a binding ratio of just under 50% is expected, as half of the anchor groups are bound and half are unbound, as well as some attenuation of the bound signal since it is under the molecular layer. Molecule **5A** is large, with a length of 3.2 nm and long solubilising arms which should prevent the molecule from arching over and contacting the surface with both anchor groups. One explanation for this could be the roughness of template-stripped gold. With a large amount of surface variation and steps on the atomic scale, this could facilitate to top thioacetate group getting close enough to surface gold atoms and cleaving the acetyl group. An alternative theory is gold atom migration through the SAM layer. In a recent study it was shown that surface gold atoms can diffuse upwards, along the molecular backbones of nitrogen containing molecules with a thiol present at the top when under light exposure in ambient conditions [194,195]. Such a process may be occurring in SAMs grown from molecule **5A**, where gold atoms diffuse through the SAM layer and nanoparticles cluster on

top of the SAM. This could potentially de-protect the upper thioacetate and result in the unusually high binding ratios seen across all of the samples.

AFM of each sample is carried out by the method outlined in Section 5.2.3. Scratch tests are performed by scanning in contact mode using a high deflection setpoint ($> 100\,\text{nN}$) and high scan rate ($4\,\text{Hz}$) for 5 minutes. The layer heights are then calculated as before: subtracting the mean height inside of the scratched area from the mean height outside, not including the scratch walls. The results are shown in Figure 5.6.

The AFM revealed very well formed layers, which appear well packed with minimal amounts of apparent physisorbed material. This is evidenced by the plotted histograms. Unlike molecules 4A-C in Chapter 4, no additional masking was needed aside from select spots which appear as saturated bright yellow on the AFM images. With these spots manually masked, the histograms show a smooth distribution with a mean value centred at the peak.

Sample #	Layer Height	Average Tilt Angle
Sample 1	1.6 nm	60°
Sample 2	1.7 nm	58°
Sample 3	2.0 nm	51°
Sample 4	2.2 nm	47°
Sample 5	1.7 nm	58°
Sample 6	2.2 nm	47°

Table 5.2: Table of layer heights and molecule tilt angles for each sample. The error in each layer height is ± 0.1 as discussed previously. The molecular tilt angle is taken from the surface normal and is calculated using 3.2 nm as the length of the molecule.

The calculated layer heights and corresponding molecule tilt angles for each

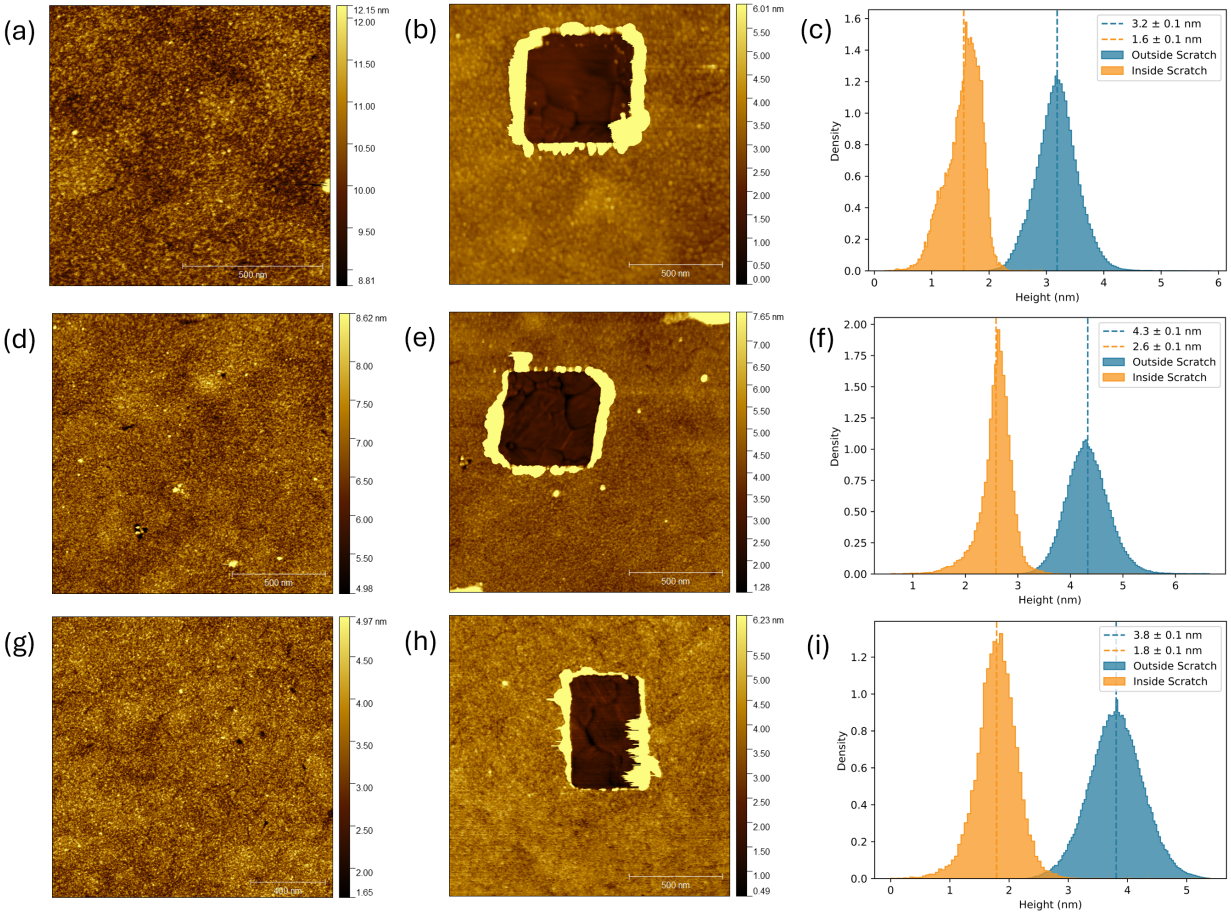

Figure 5.6: AFM images, including topography and scratch tests, as well as histograms depicting the average height inside and outside of the scratched area for sample 1 (a-c), sample 2 (d-f) and sample 3 (g-i).

sample are presented in Table 5.2. There is some variation between the layer heights, which range from 1.6 nm to 2.2 nm. There does not appear to be a correlation between the the amount of sulphur binding or surface coverage from the XPS to the calculated layer heights from AFM. Overall from the XPS and AFM data it can be said that each attempt at growing a layer of molecule **5A** was successful and appears to have formed a good SAM, however there are some significant inconsistencies between the samples. There is variation in additional oxygen, total sulphur and quantity of sulphur binding from XPS, as well as layer height in AFM.

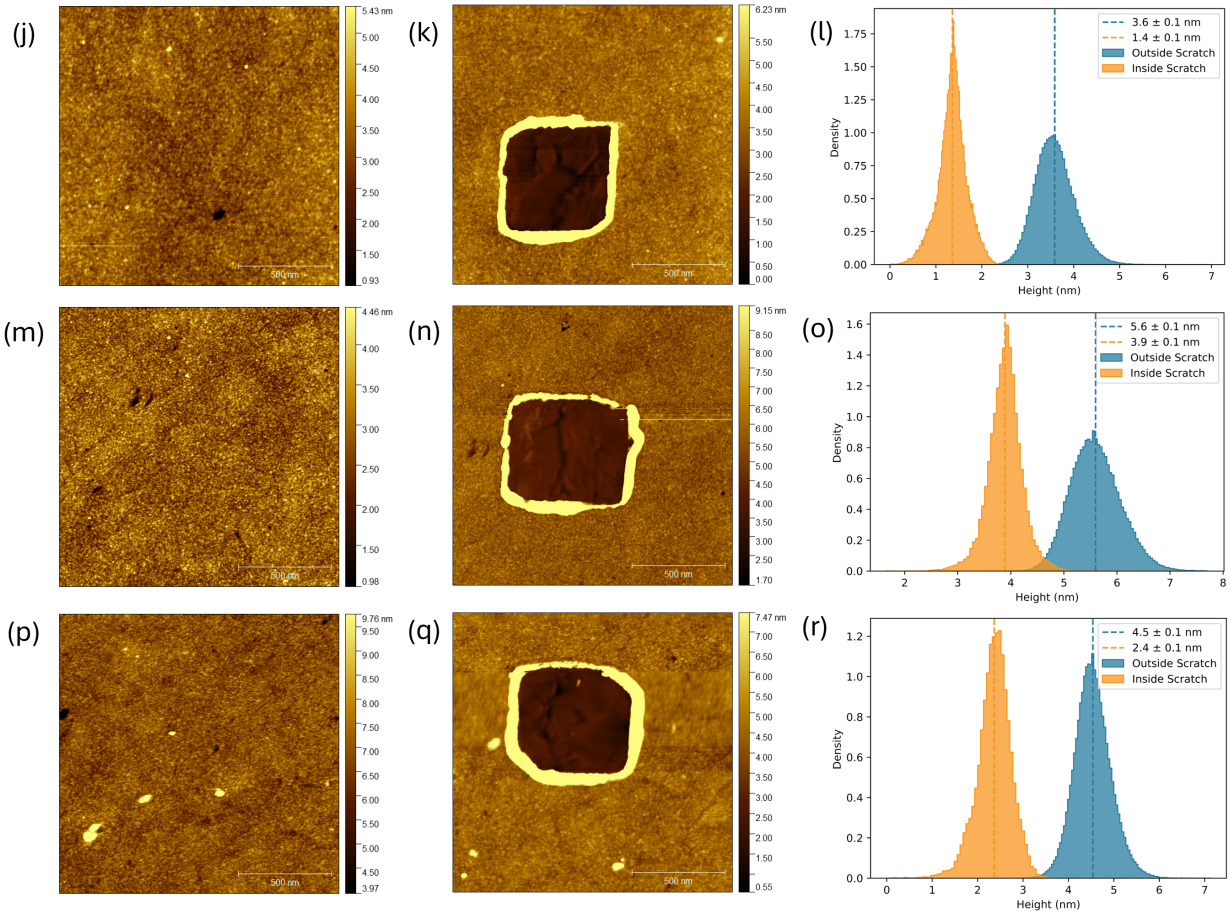

Figure 5.6: AFM images, including topography and scratch tests, as well as histograms depicting the average height inside and outside of the scratched area for sample 4 (j-l), sample 5 (m-o) and sample 6 (p-r).

Conductance data was measured using cAFM as detailed in Section 5.2.3. For each sample, at least 500 I-V traces are recorded between at least two areas on the surface. The results for sample 1 are shown in Figure 5.7. The measured I-V traces were incredibly consistent, as can be seen from the 2D histogram in Figure 5.7a. Almost no variation is seen between traces, especially on the negative bias side, despite changing both the bias sweep rate and the deflection setpoint throughout the measurements. This 2D histogram also includes three separate areas, between which the probe is withdrawn and the position offset is changed by 1 μm before re-engaging.

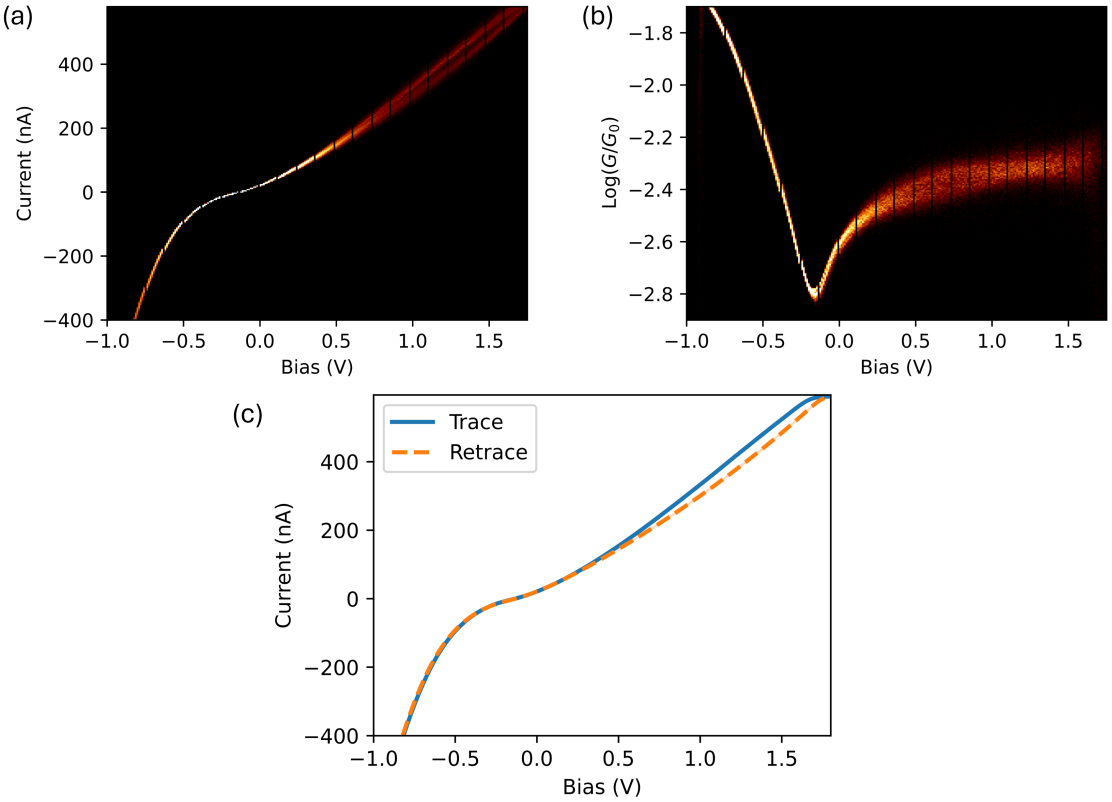

Figure 5.7: Collection of 1500 I-V traces collected via cAFM over 3 areas. (a) 2D histogram containing all of the collected I-V traces, where a brighter colour indicates more counts. (b) Corresponding 2D histogram showing the differential conductance throughout the bias sweep. (c) The trace and retrace averaged over all data points to highlight the hysteresis effect.

In Figure 5.7b it can be seen that the minimum junction conductance is not centred on 0 V. The measured low bias conductance of the junction is therefore slightly increased and is found to be $\log(G/G_0) = -2.5 \pm 0.1$. Hysteresis can be seen between the average trace and retrace in Figure 5.7c. The consistency of this hysteresis effect is highlighted in the 2D histogram of I-V traces, where there is a clear gap between two paths in the positive bias regime. The size of the hysteresis loop remained constant while the frequency of the bias sweep was changed between 0.5 V/s and 16 V/s. This rules out the possibility of a capacitive effect since that

would be frequency dependant. Memrisitive behaviour is therefore suggested as an explanation for this effect. The on/off ratio is extremely small however, with a change in conductance for $\log(G/G_0)$ of 0.2 at the point where the hysteresis is at a maximum. The other five samples were also measured using cAFM. The results brought a lot of variety between the samples, while maintaining consistency within the individual samples. In each case, much like the first, the I-V traces remain unchanging throughout the measurement. It is therefore valid to highlight the results using average trace/retrace plots. The results are shown in Figure 5.8.

A hysteresis effect can be seen in samples 1, 3 and 6. There is a notable difference in the conductance between each sample, shown in Table 5.3. However, the given conductance values alone may be misleading and should be used in context of the I-V sweeps. Each sample exhibits a different trace shape and is non-linear around zero bias. The current saturates earlier on some samples than others due to limitations of the TUNA module used to collect the data. A maximum current of 600 nA can be recorded before the signal saturates. Therefore in each case, only the I-V trace within the measurable current window can be shown. It cannot be concluded whether the other samples do exhibit switching or not outside of the current range measured. This dismissal is not so simple, however. Sample 4, Figure 5.8d, exhibits a conductance very similar to that of sample 1, which has the most pronounced hysteresis effect. Although, the relatively lower conductance is due to a shallower current gradient at low bias. The current increases rapidly as the bias reaches ± 0.6 V and still saturates before the full bias window of sample 1 can be seen.

Sample 3 shows hysteresis in the negative bias regime, but current saturates on the positive side before the expected switching ranges given by sample 1 and 6, which occurs over 0.6 V. Based on previous studies from collaborators using this molecule, it is expected to see some amount of conductance switching on both sides of the bias range, as shown in Figure 5.9 [184]. It is important to note that the

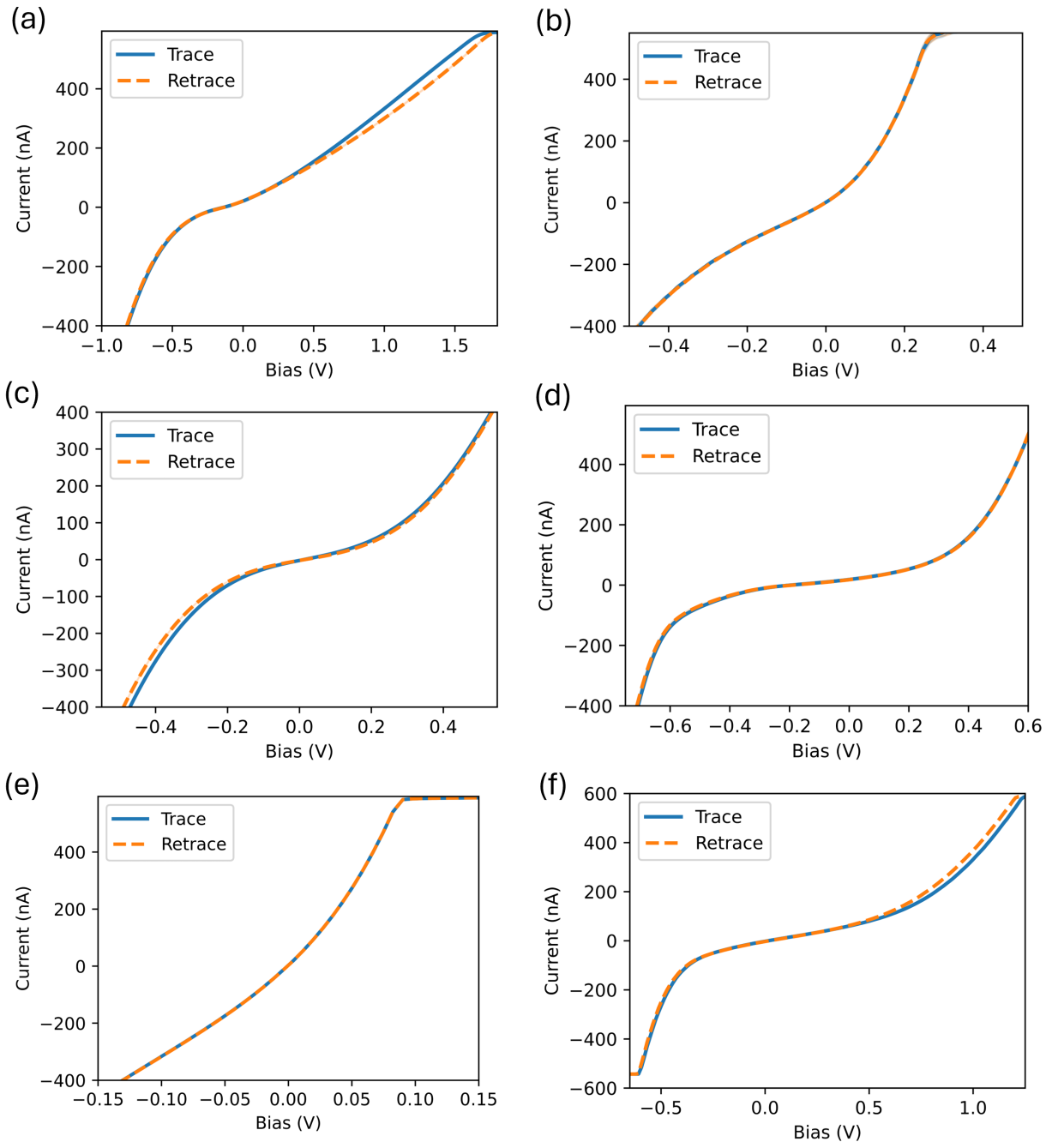

Figure 5.8: Average trace and retrace plots using at least 500 I-V sweeps over a minimum of 2 areas for samples 1-6 (a-f) respectively.

Sample #	Conductance $\log(G/G_0)$
Sample 1	-2.5 ± 0.1
Sample 2	-1.8 ± 0.2
Sample 3	-2.2 ± 0.2
Sample 4	-2.5 ± 0.2
Sample 5	-1.2 ± 0.1
Sample 6	-2.7 ± 0.1

Table 5.3: Measured average conductance values at low bias for samples 1-6. The uncertainties given are the standard deviation of the histograms obtained from the I-V traces. Standard deviation is calculated by $\frac{\text{FWHM}}{2\sqrt{2\ln 2}}$.

group which created this image used an experimental setup opposite to that in this thesis, they used a grounded sample and swept the bias through the probe. This causes the current to flow in the opposite direction, so the x-axis should be reversed when comparing to data presented in this thesis.

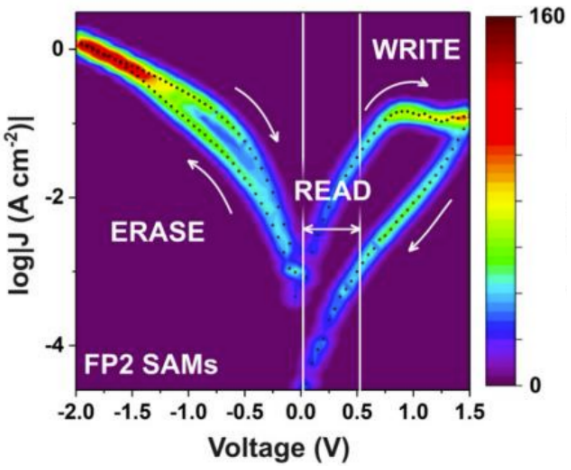

Figure 5.9: Example heat map of I-V traces collected for molecule **5A** in a junction with gold and EGaIn electrodes from a collaborating group. The x-axis should be reversed when comparing with other data in this thesis. Image from [184].

The hysteresis effect seen in samples 1 and 6 is similar to that of the negative bias regime in Figure 5.9. This suggests that some of the conductance switching effect is being recreated. However the large hysteresis loop is not being created, possibly due to an insufficient bias magnitude applied. Sample 3 observes some hysteresis on the same side as the large loop, and zooming into the negative bias regime on sample 6 shows a very minor hysteresis effect, potentially indicating the possibility of switching in both the positive and negative bias regimes within a single sample. This is shown in Figure 5.10. However, while the minor hysteresis can be seen on individual I-V traces, the on/off ratio is too small to draw any conclusions.

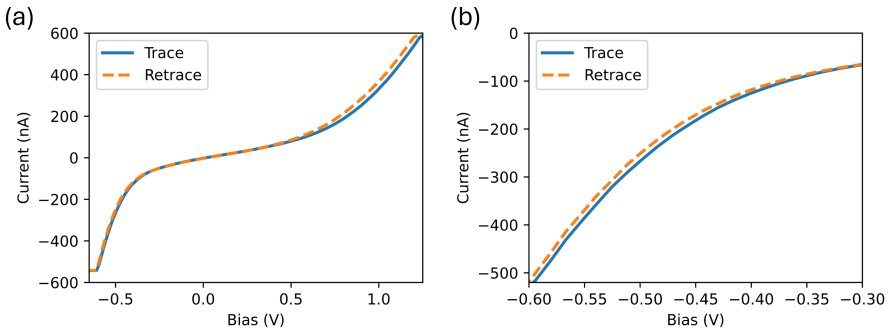

Figure 5.10: Average trace and retrace for sample 6 over the whole bias range (a) and zooming into the negative bias regime to highlight a minor hysteresis effect (b).

Three of the six samples measured showed a hysteresis effect. There is not a clear reason why these samples appear to work from the analysis conducted on them. There does not appear to be any correlation between XPS data, such as binding configurations and oxygen contamination, layer formation and height from AFM or conductance from cAFM. Despite the differences in layer properties and I-V curves between all the samples measured, each sample remained incredibly consistent within itself and showed little to no variation of measurements across the sample. Additional information is required from the growth of more samples to add to the pool of data, however more recent attempts to achieve this has not yielded the consistent cAFM of the initial samples made. The instability of the recent junctions

give a level of noise and inconsistency to the I-V traces which make it impossible to draw any conclusions, especially given the subtlety of the effects seen in samples 1,3 and 6. Despite this, additional experiments were performed on existing samples in order to better understand the switching mechanisms in the SAMs.

5.3.3 Graphene Capping

Graphene capping a sample by spreading graphene flakes over the SAM should help measurements two-fold. Firstly, by adding a solid contact over the soft SAM layer, the stability of the junction should be increased for the purposes of cAFM. While this is not needed for the initial samples due to their apparent inherent stability, it could be useful to stabilise future samples which do not possess this property. Secondly, contacting a graphene flake with a conductive probe greatly increases the effective area of measurement. Graphene possesses great in-plane conductance, so the range of effective electrical contact of the probe can span across the flake. While it is expected that not all molecules under the graphene flake will effectively couple and contribute towards transport, the total number of molecules in the junction compared to just a conductive probe is greatly increased. If each molecule is providing its own contribution towards the conductance switching effect within the junction, increasing the number of molecules in the junction should exaggerate the overall effect.

Graphene flakes were deposited on sample 1, which already presented the strongest hysteresis effect of all the samples measured. This was carried out by a colleague using Langmuir-Schaefer deposition, whereby a solid-like thin film of closely packed graphene flakes is suspended on a deionized water sub-phase. Sample 1 is then stamped horizontally onto the graphene film, transferring flakes to the surface of the SAM. The surface was then examined using AFM, as shown in Figure 5.11.

Once a large flake was found from a 30 μm scan size, it was chosen to be used as a

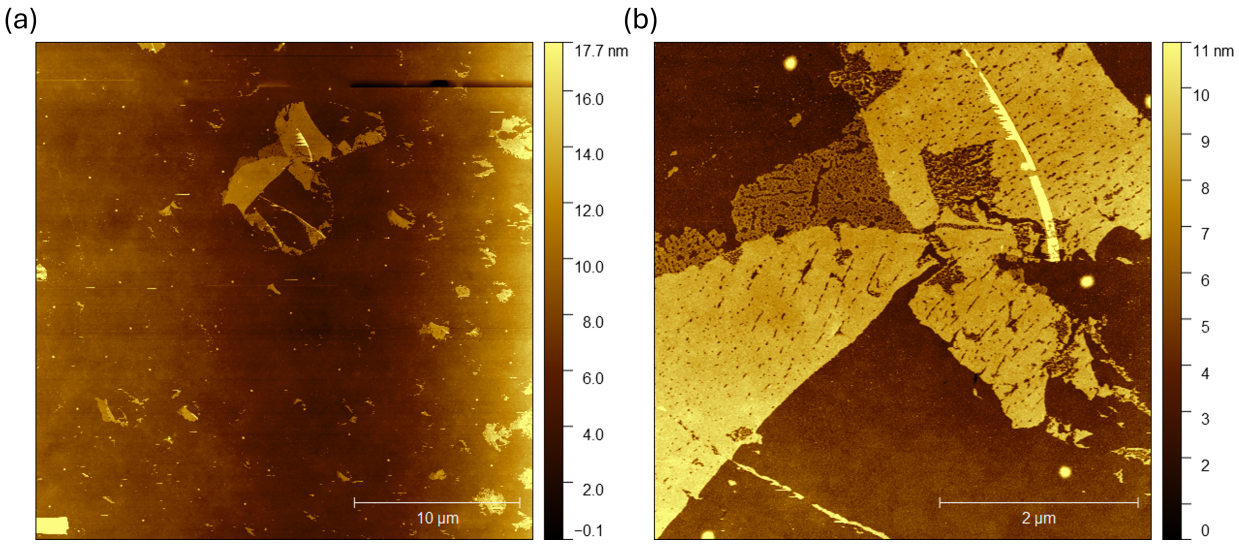

Figure 5.11: Topography AFM images showing the surface of sample 1 after graphene flake deposition. The scan sizes are 30 μm (a) and 5 μm (b) in the same area.

contact point. The topography images in Figure 5.11 were taken using a conductive probe in peak-force mode. Since the peak-force setpoint typically used is very low at 300 pN, the conductive coating should remain undamaged. A spot was chosen at the bottom left section of the flake in Figure 5.11b where a 2 μm X 2 μm image could be taken fully on the graphene flake. This was to ensure the probe engaged on the flake and would not move off due to thermal drift during measurements. The AFM mode was then switched to contact mode ready for cAFM. The results are shown in Figure 5.12.

The hysteresis effect is much more pronounced here. The additional sum of molecules within the electric junction has made a big difference, in both the size of the hysteresis loop and the bias at which it appears. The hysteresis here is already in effect at zero bias, where it could only be seen above 0.6 V previously for sample 1. This reinforces that the hysteresis seen is a property of the molecule itself, since the effect scales with the number of molecules in the junction. Additionally, the

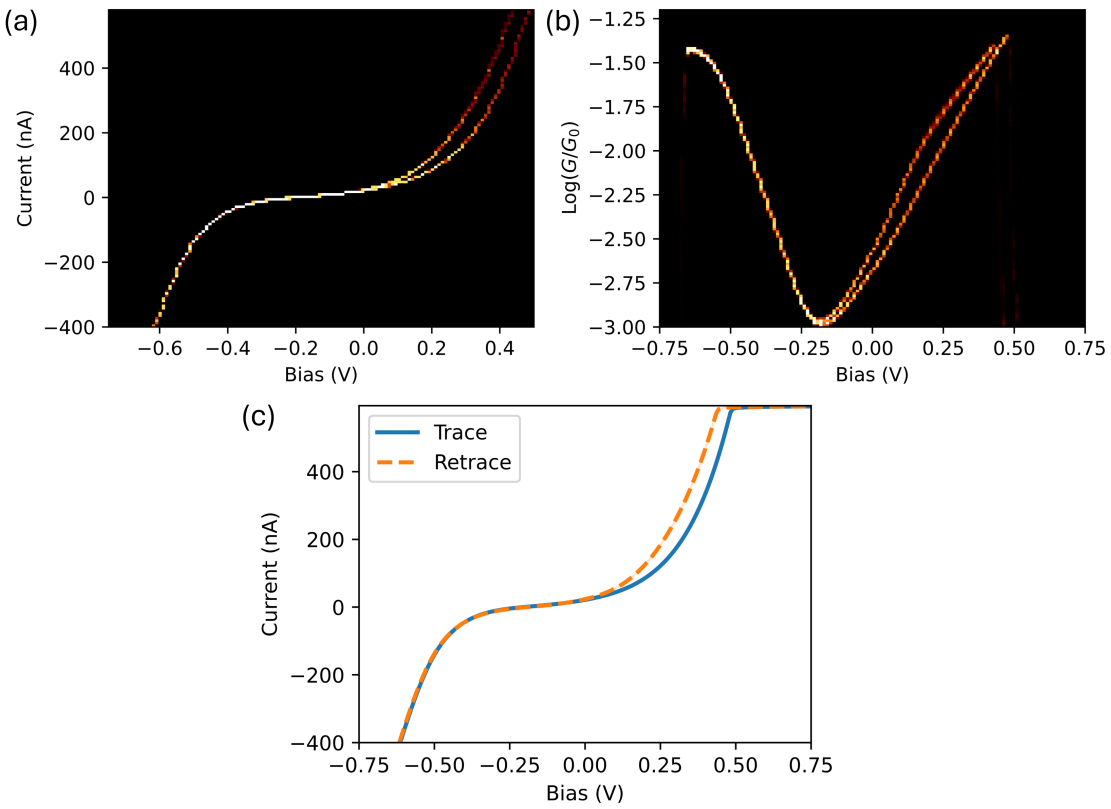

Figure 5.12: Collection of 1000 I-V traces collected via cAFM. (a) a 2D histogram containing all I-V traces, where a brighter colour indicates more counts. (b) Corresponding 2D histogram showing the differential conductance throughout the bias sweep. (c) The trace and retrace averaged over all data points.

graphene flake did indeed stabilise the junction. Where the conductance switching appeared more as a smeared region in the conductance 2D histogram for sample 1 in Figure 5.7b, here with the addition of graphene, there are two well defined and fully separated lines. The low bias conductance of the junction increased to $\log(G/G_0) = -2.0 \pm 0.3$, as expected for an increase in contact area. The current saturates at a relatively low bias, but due to the increased hysteresis presence the effect is still clearly seen. While this is the only sample which graphene capping was tested on, it provides much promise for future samples. Both to provide stability in the more recent noisy sample junctions, and to view hidden effects which may have been either too small or out of the measured bias range previously.

5.3.4 Sample Annealing

To further investigate the growth and binding configuration for a SAM of molecule **5A**, sample 2 was annealed at 100 °C overnight in UHV conditions. After completing the full analysis of sample 2 detailed in the sections above, the sample was was transferred back to the XPS where it was annealed for ≈ 18 hours at 100 °C before capturing new spectra to see how the sample had changed chemically. Figure 5.13 shows the XPS before and after annealing.

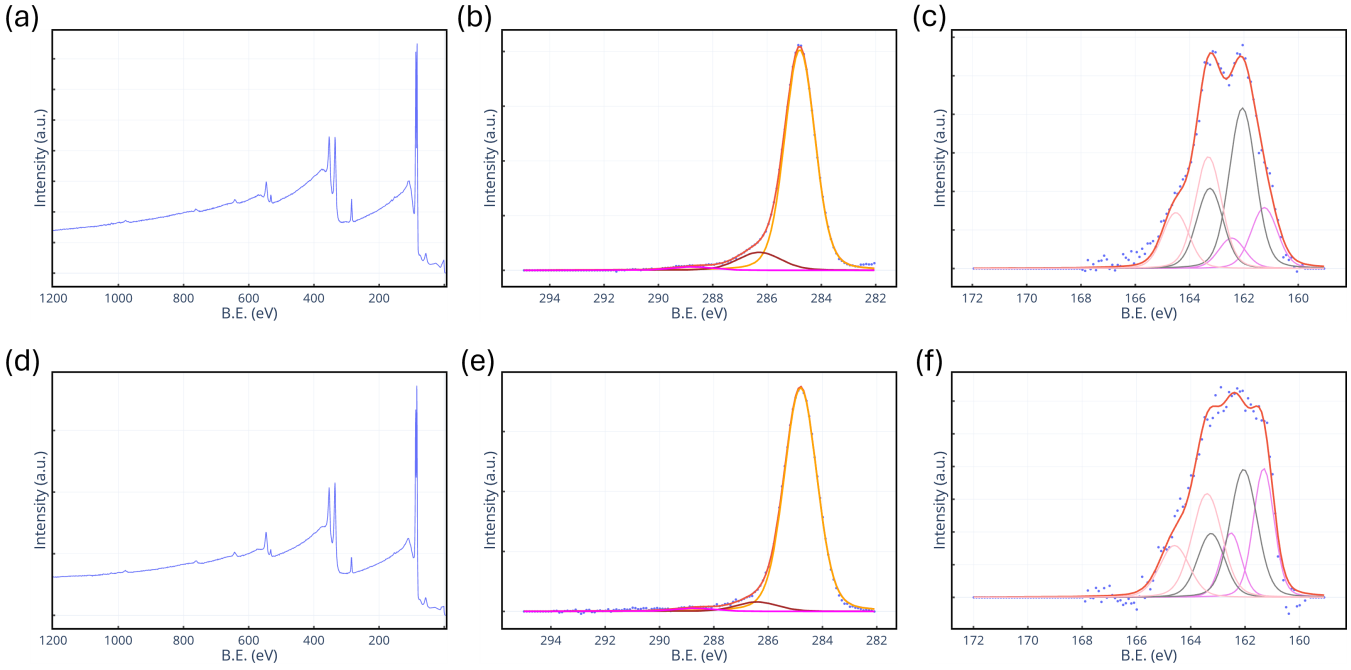

Figure 5.13: XPS spectra showing wide regions (a, d), and high resolution spectra of the C 1s region (b, e) and S 2p region (c, f) for sample 2 pre-annealed (a-c) and post-annealed (d-f).

The most notable change is the binding in the S 2p region. When fitting the sulphur doublets, each doublet agrees with the binding energy of the pre-annealed sample within 0.1 eV. The total binding is identical, with both pre and post-annealed samples agreeing on 66% total binding. The dominant type of binding, however, has shifted dramatically. The 161.3 eV peak, assigned to hollow site binding, increases

while total binding remains constant. The atom-top binding is now 56% post-annealing, compared to 72% pre-annealing. One reason for this could be gold surface reconfiguration due to heat. Typically, despite the hollow site configuration having a lower binding energy, it remains energetically unfavourable within a SAM due to a mismatch between the molecules, where molecule-molecule interactions dominate over the gold binding configuration. Here, however, it is proposed that the energy given to the sample surface allows for gold reconfiguration to shift surface morphology, whereby gold atoms arrange to allow more hollow sites in places where molecules can still interact with each other favourably. In other words, rather than molecules finding the optimal configuration on a near-preset surface, the additional energy from heat would allow the molecules to work with the gold surface to find an overall configuration with an even lower surface energy, which should involve more hollow sites placed at optimal points.

Another explanation is that S-C cleaving is occurring. In previous studies, the peak at 161 eV has been assigned to atomic sulphur species, which are lone sulphur atoms on a gold surface [196]. This was due to the binding energy matching that of gold sulphide species (Au_2S) in an XPS study of sulphur adsorption of gold [197, 198]. This peak is not assigned as atomic sulphur during the initial SAM, as such species are known to prevent further adsorption of thiol molecules, so would form an incomplete SAM, contrary to that shown in the AFM images of molecule **5A** in Figure 5.6 [199]. Additionally, although it has been shown that atomic sulphur can form during thiol adsorption, the quantity should increase with deposition time [200]. It will be shown in Section 5.3.5 that this trend does not hold, with the longest deposition having the smallest relative 161 eV peak. However, after the SAM has formed, it is possible that too high a temperature could cleave the S-C bond and lead to an increase in atomic sulphur. Since atomic sulphur only exhibits an *sp* binding configuration [201], an increase would be indistinguishable from that already assigned to hollow site binding. One issue with this explanation

is that the S-C cleaving would be expected to result in a reduction of the unbound species too, either by complete desorption from the surface or a partial desorption and subsequent re-adsorption with the other anchor to a free site. Since the total binding is unchanged from the pre-annealed sample, the first explanation of surface reconfiguration is reasoned to be more likely.

In the C 1s spectra, the secondary peak (brown) at $\approx 286\,\text{eV}$ halves from 10% of the total carbon spectra in the pre-annealed sample to 5% in the post-annealed sample. This could be due to a reduction in the C-S bonds, as explained by the C-S cleaving theory, or by a reduction in C-O bonds which overlap in energy and cannot be separated with the XPS system used. There is a reduction in the oxygen on the sample as seen from the wide spectra, so it would make sense for the C-O signal to also decrease. This could be due to desorption of the water layer from the surface to to the applied heat, or due to the desorption of adventitious carbon which typically contains C-O species.

5.3.5 Varying Deposition Times

SAMs of molecule **5A** were grown using a variety of deposition times to see the timescales necessary to form a well-packed complete layer. This is useful information for translation to devices, where deposition times should be minimised for efficiency, or to allow other means of deposition such as passing fibres through solution. Times of 1 minute, 10 minutes, 2 hours and 24 hours were chosen. XPS analysis of each is shown in Figure 5.14. These depositions were performed in ambient conditions, outside of the glovebox environment.

The oxygen on the wide spectra is consistently small and does not appear to change meaningfully between samples. From the C 1s spectra, the third peak (magenta) at $\approx 288\,\text{eV}$, assigned to C=O, decreases as time increases. While this would usually point to an increase in sulphur binding over time, due to the

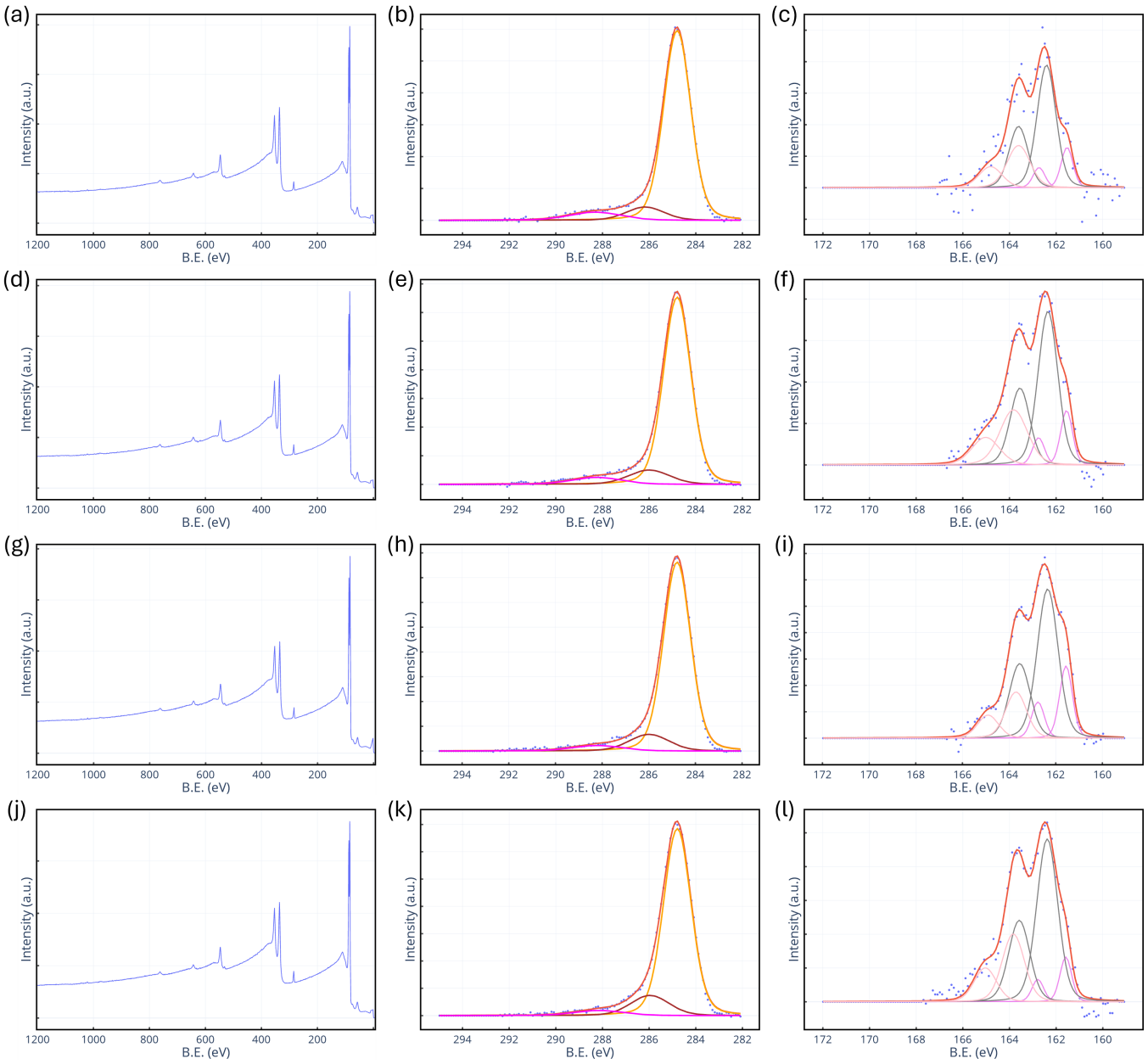

Figure 5.14: XPS spectra showing wide surveys, the C 1s region and S 2p region for varying deposition times of 1 minute (a-c), 10 minutes (d-f), 2 hours (g-i) and 24 hours (j-l).

presence of C=O in the thioacetate, the actual binding percentages calculated from the sulphur spectra, given in Table 5.4, do not reflect this. The secondary peak (brown) increases slightly as time increases. Since the oxygen does not change, this

is likely an indication of more molecules on the surface, seen as an increase in C-N and C-S bonds.

Deposition Time	Atom-Top Binding %	Total Binding %
1 minute	80%	76%
10 minutes	78%	72%
2 Hours	79%	81%
24 Hours	88%	75%

Table 5.4: Table of binding percentage in each sample. The atom top binding % was calculated as the area under the grey peak against the total area under the grey and violet peaks. The total binding % was calculated as the area under the grey and violet peaks against the total area under the envelope.

The atom-top binding is mostly unchanged between deposition times, until a large increase for the 24 hour sample. The atom-top binding of this sample appears higher than any of samples 1-6, although sample 6 was at a close 86%. As a direct comparison between times, the increase in atom-top binding is expected for a longer deposition. As discussed earlier, the hollow site coordination usually occurs in lower coverage SAMs. When given more opportunity to rearrange, atom-top coordination should increase [193]. A crucial difference between these samples and the original samples 1-6 is that these were prepared outside of a glovebox, potentially impacting the deposition. The total binding is maximised at the 2 hour deposition, potentially indicating a detrimental effect of prolonged exposure to the solution when in air. However, there are no usual signs of contamination such as an increased oxygen signal or the presence of rogue elements.

AFM topography was taken for the 1 minute deposition to show the lower bound of growth for a SAM of molecule **5A**, shown in Figure 5.15. Overall coverage appears to be good for such a short deposition, although there are many gaps in the SAM

layer that can be seen in Figure 5.15a, indicating incomplete packing. Still, a clear area can be scratched away which shows a full SAM has formed, despite not being densely packed.

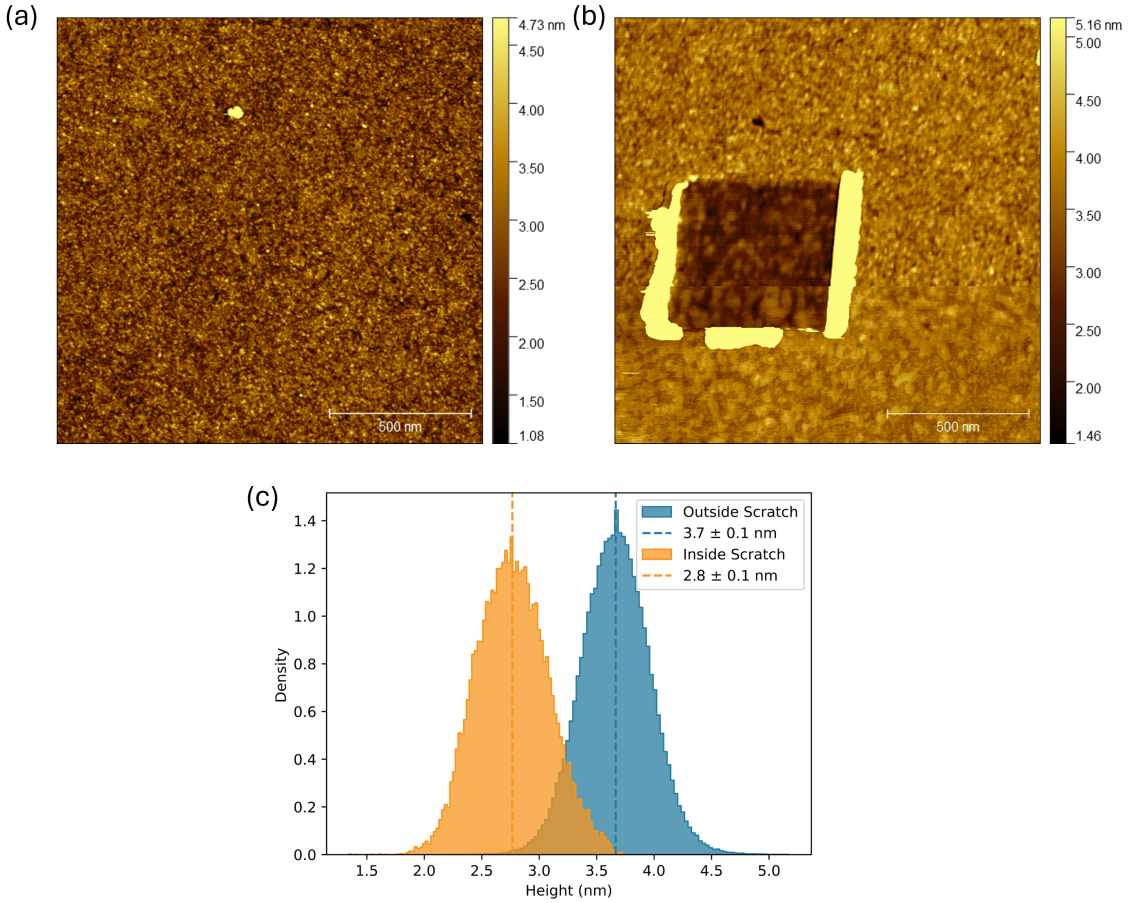

Figure 5.15: AFM results from a 1 minute deposition of molecule **5A**. (a) Topography image for a 1.5 μm X 1.5 μm area. (b) Topography image of the same area taken post-scratch. (a) histograms showing the height distribution inside and outside of the scratched area.

The histograms show smooth distributions in Figure 5.15c, despite no additional masking on the layer. This once again shows how consistently a SAM of molecule **5A** can form, even with a short deposition in this case. The layer height obtained from the histograms is 0.9 ± 0.1 nm, a significantly smaller layer height than all the

other depositions. This is expected since the molecules do not have time to densely pack and allow intermolecular interactions to align heights to a more optimal angle across the SAM. In addition to this, the outside histogram underestimates the height of the layer due to the holes present in the SAM. These are included in the natural variation of the SAM surface which in turn leads to an underestimation in the mean height. The AFM shown here reveals the coverage may be sufficient for devices to use similar fast depositions, especially if being contacted with a large top electrode such as an EGaIn probe.

5.3.6 Conclusions and Future Work

Molecule **5A** consistently made very neat SAMs, as seen by the AFM topography images. This is likely due to the size of the molecules resulting in an increase in molecule-molecule interactions, improving the consistency of the packing over the surface. The cAFM remained incredibly consistent for each sample over hundreds of I-V sweeps and multiple areas. This could be due to the strength of the SAM. With the packing producing such a stable SAM, forces exerted by the probe may have had negligible effects on the structure of the layer. This reduces the changes caused by damage from continuous measuring, and effects of probe drift will be mitigated from the uniformity of the layer. Such consistency of the junction allowed for small hysteresis effects in some samples to be seen. This hysteresis seen across the I-V traces is thought to be evidence of memristive switching in the molecule. The effect looks similar to that already shown in previous studies using this molecule [184], although the bias range measured may be hiding a signifiant portion of the full effect. This is due to a limitation on the maximum current able to be measured with the equipment used. The effect is exaggerated by means of graphene capping, evidencing the hysteresis seen is an effect of the molecule since the effect increases as the effective number of molecules in the junction increases. This implies the EGaIn top electrode used previously is not essential to the switching mechanism, but likely improves the ability to measure it due to a greatly increased contact area

and inherent stability of the junction.

While the samples were consistent within themselves, the results between samples were much less so. The conductance changes by over on order of magnitude across the measured samples. Three of the six samples showed the switching effect to different degrees, although it cannot be said whether the limit of the current measured prevented observation of hysteresis in other samples. The analysis of the samples showed different layer heights, oxygen presence and sulphur binding across all samples. One consistency was that the total binding of sulphur to gold was always over 50%. While the cause of this remains unknown, it is hypothesised that gold nanoparticles may be forming on top of the SAM by diffusion of gold atoms through the layer [194]. Additional experiments should be conducted to investigate this further, such as increased light exposure or iodine doping of the gold surface prior to SAM growth. Iodine doping should facilitate the diffusion as it has been shown that adsorbed iodine can increase the mobility of surface gold atoms [202]. One attempt of iodine doping post-deposition showed disruption to the SAM by a greatly reduced sulphur signal in XPS. In addition, there are also questions on whether the iodine can properly interact with the gold substrate after a SAM has been grown. Therefore doping pre-deposition is preferred and should be tested.

Use of graphene capping greatly enhanced the clarity of the switching by increasing both the stability of the junction and the number of effective molecules within the junction. Additionally, the work function of graphene likely plays a part in facilitating the switching effect. Goswami *et.al* showed the choice of electrode can determine whether switching occurs within a reasonable bias window. They demonstrate a lack of hysteresis within their chosen bias range when using a combination of Pt and Au electrodes, and using an indium tin oxide (ITO) top electrode with either Pt or Au bottom electrodes restores the effect. They attribute this to the deep work functions of Pt and Au, 5.6 eV and 5.1 eV respectively, causing

the applied bias to be insufficient to inject electrons into the molecule. Whereas ITO has a work function of around 4.5 eV, a lower bias need to be applied before the electrode Fermi level aligns with the desired molecular orbital. EGaIn, as used in the previous work shown earlier by collaborators [184], has a work function of around 4.2 eV [185], similar to that of ITO. The addition of a graphene cap likely facilitates the switching of the junction since the work function of graphene is also similar, around 4.6 eV [203]. The choice of electrode is an essential parameter when considering device fabrication. From the results presented here, it appears the shallower work function of the electrode may be important to optimise the properties of the memristive molecule being investigated. In this case, a smaller switch-on bias is required to change the conductive state when using a graphene cap. A lower energy per operation results in an improved TOPS/W from Equation 2.25. The devices could therefore present an improved figure of merit from electrode choice alone, without altering the molecule itself.

Due to the success of the graphene cap on a sample that already showed memristive behaviour, it should also be trialled on samples which previously did not exhibit such effects. The next and most immediate experiment that should be carried out with this molecule is to graphene cap a new batch of samples. This could be an essential test of the sample's capability to show conductance switching before being discounted. Finally, additional tests to confirm the hysteresis seen is a memristive effect are needed. Read, write and erase operations by carefully controlling the bias ranges used should be employed, as in previous studies [184]. This would examine the molecule's ability to hold a changed conductance state, and the ability to control the switching between the two. This is essential for implementation into devices.

Chapter 6

Effect of Surface Roughness and Molecular Templating on Charge Transport in Self-Assembled Monolayers

6.1 Introduction

The quality of the substrate a SAM is grown on is an often overlooked but crucial aspect of sample preparation. While the electrode material used, or the molecule anchor group chosen are often looked at as the key aspects in the investigation of an electrode-molecule interface, details such as the roughness of the surface can have a significant effect on the layer assembly, which in turn can affect the properties of the grown SAM. In a previous study, it has been shown that alkanethiols grown on a flame-annealed Au(111) on mica and template-stripped gold (TS-Au) can have measurably different mechanical properties [204]. They show the layer on TS-Au is more compressible and less homogenous over the measured area due to the disorder in the layer arising from the surface roughness. They quote roughness values for Au(111) and TS-Au of 1 Å and 3 Å respectively over μm scales. These are the two substrates that will be used and compared in this chapter. Although the difference in roughness is quantitatively not large, for molecular assembly, this difference is comparable to chemical bond lengths so can greatly affect the assembly of layers and top contact formation. Example AFM topography images are shown in Figure 6.1 to highlight the difference in surface quality between Au(111) and TS-Au.

The sputter-annealed gold on mica is achieved in UHV conditions using three sputter-annealing cycles. Each cycle consists of sputtering with argon gas at a pressure of 5×10^{-6} mbar for 20 minutes followed by an annealing step at 400 °C for 30 minutes. The result is a substrate like in Figure 6.1a, where the surface is steps of atomically flat plateaus. The substrate is then taken out of UHV where it can be used in solution self-assembly, or kept in UHV for thermal deposition of molecules. Both occur in this chapter. To fabricate TS-Au, a gold layer is grown epitaxially onto a silicon surface first. Small strips of silicon from a separate wafer are cut and cleaned using acetone, IPA and UV plasma cleaning. These are then glued to the gold surface using an epoxy resin when it is thermally cured at 140 °C to set. The gold conforms to the cleaned silicon surface, creating a macroscopically

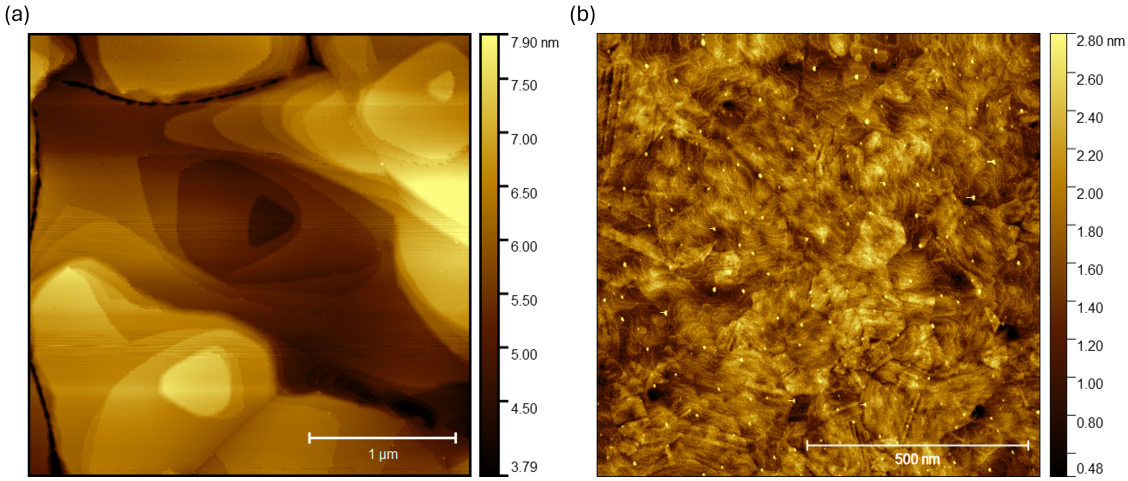

Figure 6.1: AFM topography images captured in Peak-Force mode showing examples of the types of gold surfaces used in this chapter. (a) a 3μm $\times$ 3μm image of Au(111) on mica after sputter-annealing. (b) a 1μm $\times$ 1μm image of TS-Au.

flat substrate such as Figure 6.1b. The sandwich gold can remain as such for long periods of time, and can be cleaved off for a consistently pristine, contaminant free surface on demand [171]. This is far more convenient than the Au(111) surface which requires a long UHV process and must be used rapidly to prevent contamination or degradation. TS-Au is a polycrystalline surface, where the gold has different crystal orientations separated by grain boundaries. This can include small regions of Au(111), as can be seen in the centre top of Figure 6.1b.

While the mechanical properties [204] and reproducibility of measurements [205] are shown to be affected by the roughness of the underlying substrate, this chapter aims to investigate how charge transport through a SAM is affected. The total transmission function through a molecular junction is additive of the individual transmission functions of the molecules within the junction [206]. The hypothesis is that molecules with consistent ordering and electrode coordination in the SAM should have similar $T(E)$, and therefore the more disordered the surface and less consistent the transmission at a given energy, the broader the features across the

transmission distribution. Since the Seebeck coefficient, S, is proportional to the gradient of the transmission function at the Fermi energy, from Equation 2.19, a broader distribution should lower the Seebeck coefficient. The effect on the conductance is less clear as it depends on the position of the Fermi energy relative to resonances. Conductance is related to the amplitude of the transmission function at the Fermi level, from Equation 2.18. Broader features result in reduced peak heights, reducing conductance if the Fermi energy rests near a resonance, but increased peak breadth, increasing conductance if the Fermi energy rests far from a resonance. The junction conductance can be effected by more factors, however. For example, if the heights of the molecule are more aligned, more molecules may be able to be contacted by a top electrode, increasing the number of contributing molecules to transport in the junction, and therefore increasing conductance regardless of the position of the Fermi energy. Using this hypothesis, the aim is to boost the Seebeck coefficient and conductance in a SAM only by reducing the roughness of the substrate. This study will be conducted using molecules **6A** and **6B**, shown in Figure 6.2, the electrical properties of which have already been investigated [137].

The second part of this project is to utilise molecule templating to further improve the Seebeck effect in the junctions. It has already been shown that a ZnPc layer coordinated to the top of a SAM can boost the Seebeck coefficient by up to 100% [116]. In addition, it is thought that the weak coupling to an electrode through the ZnPc would reduce the thermal conductance of the junction by suppressing phonon transmission. This study aims to build on that work, reversing the layer order and assembling the highly conjugated molecule of choice onto a ZnPc molecular template. This should increase the ordering of the SAM by providing well defined single binding points for the pyridine anchors to coordinate to across the surface, while exploiting the Seebeck enhancement already demonstrated from the ZnPc. A similar study built a multi-layer structure as proof of concept, by using a thin iron layer to decouple the Zinc-tetraphenylporphyrine (ZnTPP) from the gold electrode,

before self-assembly by thermal evaporation of the bridging molecule layer, also in UHV [207]. Neither the conductance nor Seebeck were measured in this study. Here, the aim is to build a similar structure using a combination of thermal evaporation of ZnPc and solution self-assembly of molecule **6C** to create an ordered multi-layer structure with promising thermoelectric properties.

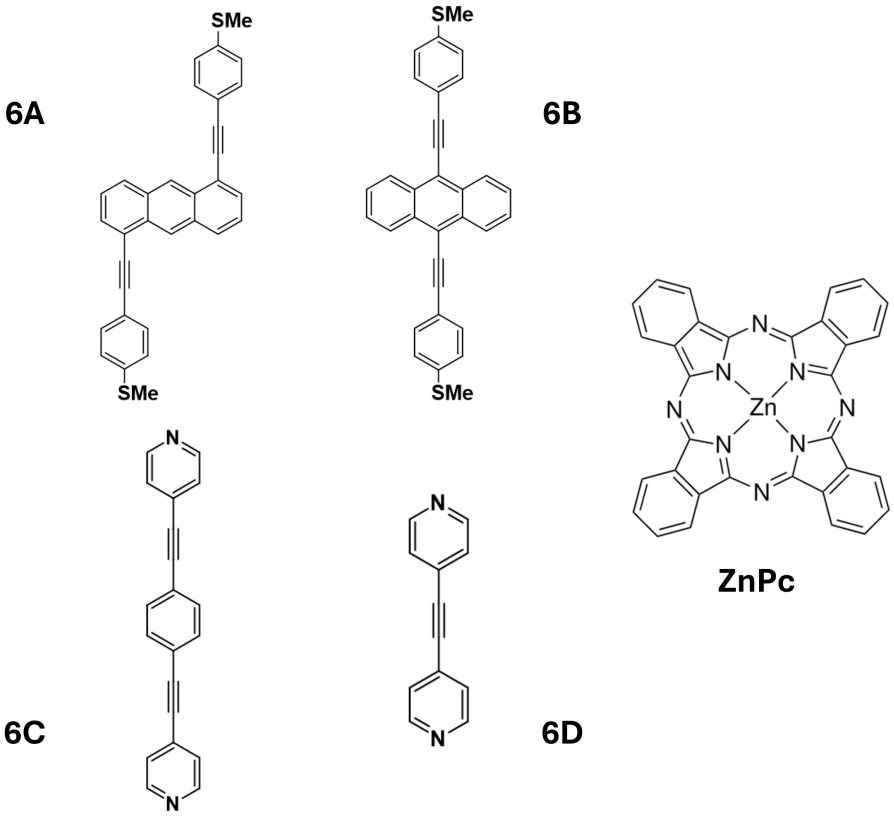

Figure 6.2: Structure of the molecules studied in this chapter. **6A** and **6B** are molecular wires with anthracene cores in a 1,5 and 9,10 connectivity configuration respectively. **6C** is an oligo(phenylene ethynylene)3 (OPE3) derivative with pyridine anchor groups. **6D** is an oligo(phenylene ethynylene)2 (OPE2) derivative with pyridine anchor groups. ZnPc stands for zinc-centred phthalocyanine.

6.2 Methodology

6.2.1 Sample Preparation

Self-assembled monolayers of molecules **6A** and **6B** were grown on Au(111) and TS-Au substrates. Powders of each molecule were dissolved and sonicated in chloroform to produce a solution with a 1 mMol/L concentration. For the TS-Au substrate, the gold substrate was immersed in solution for a total of 4 hours while rinsing with chloroform every hour. The rinsing mid-deposition aimed to aid the desorption/re-adsorption process as described in Section 3.3.1. For the Au(111) substrate, a longer deposition time was needed as the molecules appeared to by lying flat on the surface after 4 hours. The deposition time here was instead extended to 18 hours by leaving it overnight, with the addition of three hourly rinses at the start of the deposition. This was likely necessary due to the increased reactivity of the TS-Au surface due to the roughness inherently providing step edges across there sample, where the terrace sites on Au(111) are less reactive so need extra time to assemble.

The ZnPc monolayer was created first by a thick layer deposition from a long thermal evaporation. ZnPc powder in a tube of borosilicate glass is heated in UHV as described in Section 3.3.2. To create a thick layer, the crucible was heated to $\approx 500\,^{\circ}\mathrm{C}$ for 1 hour, resulting in a layer approximately 4 nm thick. The Thick layer is then transferred to the XPS, where the sample bar is heated to 400°C overnight while XPS is running. This temperature is used as a critical temperature at which excess material apart from the bottom layer is desorbed from the surface. This was calibrated in a previous experiment where the temperature was slowly increased to 500°C during XPS measurements. The point at which the Zinc signal stops decreasing implies only a monolayer remains, which is then confirmed by AFM. Molecules **6C** and **6D** could then be assembled onto the ZnPc layer through solution self-assembly. This required a choice of solvent that could both dissolve molecule **6C** while not disrupting the ZnPc player. Trial and error was utilised until chloroform

was settled on as a promising solution. Acetone is highly polar and did not fully dissolve molecule **6C**, forming a sub-optimal SAM. Toluene is ideal for dissolving molecule **6C**, but had previously been shown to disrupt the ZnPc. Toluene contains an aromatic ring which likely had a strong interaction to the π-system within the ZnPc and destroyed the layer. Chloroform was a compromise of being sufficiently non-polar to dissolve molecule **6C** and not having a strong interaction with the ZnPc. The evidence of the ZnPc layer surviving is shown in Section 6.4. 1 mMol solutions of molecule **6C** and **6D** were created in chloroform and SAMs were grown with a total deposition time of 5 hours, rinsing with chloroform every hour. The layer of molecule **6D** did not properly assemble onto the ZnPc, but provides a good comparison to the main molecule **6C** as evidence of success, as seen in Section 6.4.

6.2.2 XPS

XPS was performed using a Kratos Analytical AXIS Supra spectrometer with monochromatic Al Kα 1486.7 eV x-ray source, operating at 15 kV, 15 mA, and equipped with an electron gun for charge neutralisation. Pass energies of 20 eV and 10 eV were selected for C 1s and Au 4f respectively, while 40 eV was selected for the other elements measured, that is Zn 2p, O 1s, N 1s and S 2p. These values were chosen to optimise resolution against counts for each element measured. All spectra shown are charge corrected to the C-C peak centred at 284.8 eV. All the spectra were analysed using CASAXPS (Casa Software Ltd, UK).

6.2.3 AFM

All AFM measurements were carried out using a Bruker MultiMode 8 with a Nanoscope V controller in ambient conditions. Images were captured with PeakForce mode using NuNano Scout probes. These probes have a resonant frequency of 70 kHz and a spring constant of 2 N/m. Images were typically taken with a PeakForce setpoint of 300 pN and a scan rate ranging between 1-1.5 Hz. Conductance data was collected using a Bruker TUNA module and Budget Sensors ElectriMulti75-G

probes. These are silicon probes coated with a conductive platinum layer.

6.3 Results and Discussion of Surface Roughness Effects on Charge Transport

SAMs of molecules **6A** and **6B** are grown on both Au(111) and TS-Au as described in Section 6.2.1. XPS analysis was conducted on each sample, the results of which are shown in Figure 6.3.

The C 1s spectra shows the usual C-C peak (orange) which is used as a reference at 284.8 eV. The peak at ≈ 286 eV (brown) will be predominantly C-S species from the thioether anchor group. This anchor group, labelled as SMe in Figure 6.2, involves a C-S-C bond, so each anchor group is contributing to two C-S bonds. This is why the 286 eV peak appears larger than it may have on other samples. There will also be some contributions from C-O contamination, as evidenced by the third peak at 288.5 eV (magenta) present in each sample which is assigned to C=O. This is thought to be due to the adventitious carbon layer on the surface caused by air exposure.

The S 2p spectra reveals low binding, especially for molecule **6A**. Molecule **6B** exhibits two clear doublets, positioned at 162.6 eV and 163.6 eV for Au(111), with 161.8 eV and 163.3 eV for TS-Au. The higher energy doublet is consistent with unbound sulphur in a thioether and the lower energy doublet appears as coordination to the gold surface. Even as a thioether, this surface coordination bond is expected to give a binding energy of ≈ 162 eV, similar to that of a thiolate [201]. While both surfaces show a greater unbound signal compared to bound, in the case of molecule **6A** both surfaces are shown to be heavily dominated by the unbound signal. The exact size and position are difficult to determine due to how weak the signal is. AFM topography images in Figure 6.4 for molecule **6A** show there is a fully formed

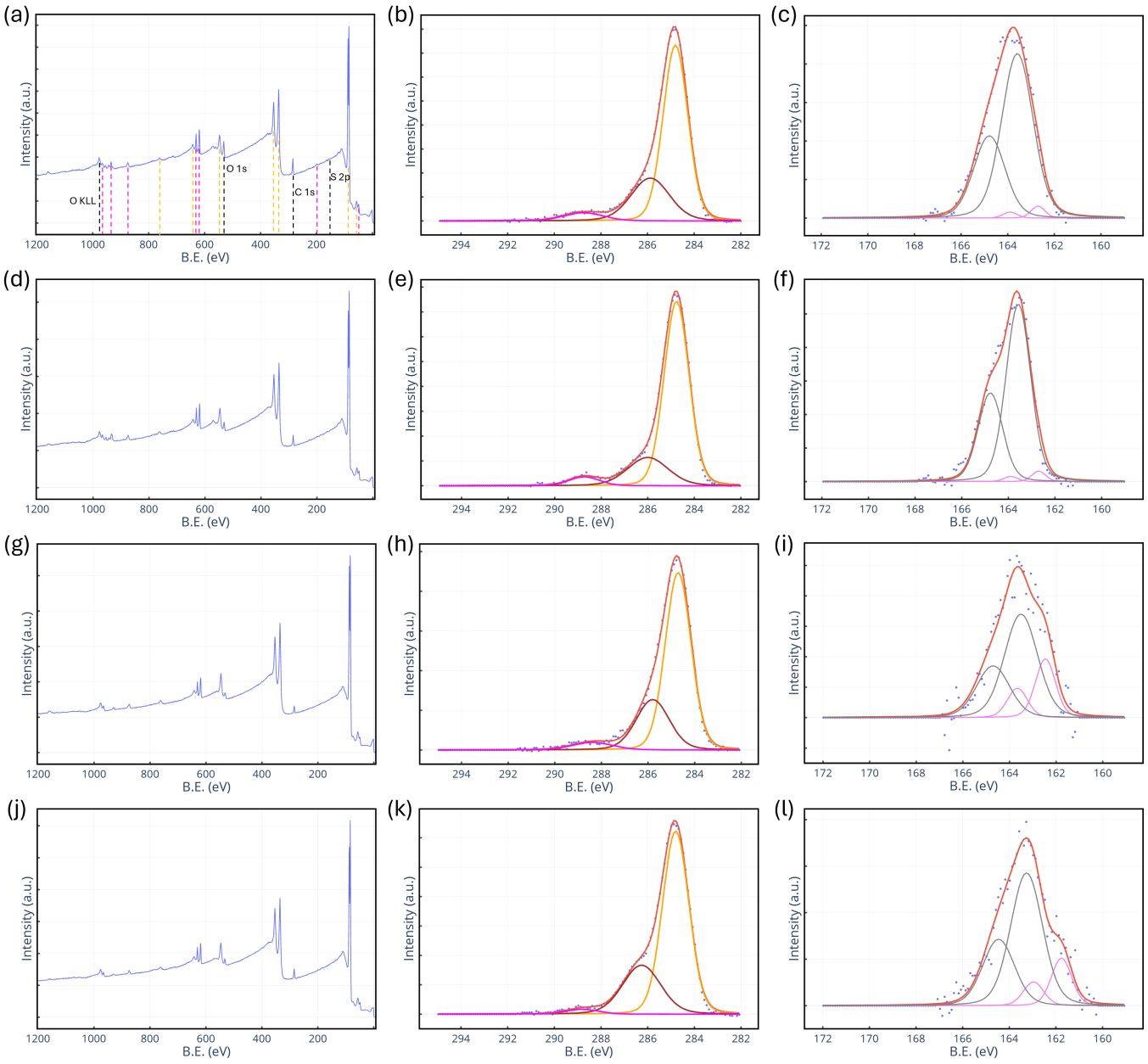

Figure 6.3: XPS spectra showing wide surveys, the C 1s region and the S 2p region for (a-c) molecule **6A** on Au(111), (d-f) molecule **6A** on TS-Au, (g-i) molecule **6B** on Au(111), (j-l) molecule **6B** on TS-Au. The wide survey (a) is used as an example to note the positions of the elemental peaks, labelled by black lines. The peaks due to gold are shown with yellow lines and peaks due to iodine are shown with pink lines.

layer, with a large amount of additional growth. The presence of the layer implies there must be some bound signal, and the level of additional growth evidences the dominance of the unbound peak.

One possible explanation for this is the iodine presence causing an interference with the self-assembly process. Iodine is be seen to be present in all of the samples. There are trace amounts seen in the XPS of the powder, so this is likely residue from the synthesis of the molecule. Iodine has a high affinity for a gold surface and has a strong chemisorption bond [208]. Even trace amounts in a solution can form an adsorbed layer onto the gold surface and potentially disrupt the SAM formation. A larger iodine signal is seen in the SAMs of molecule **6A** compared to **6B**. If there is less iodine present, the competitive binding may shift in the favour of sulphur species, allowing for more thioethers to correctly chemisorb to the surface. Although, the signal to noise ratio is certainly worse for the sulphur signal in molecule **6B**, implying less sulphur is present. This agrees with the AFM images which show much more physisorbed material for molecule **6A**. This would be the case for a SAM where additional iodine weakens the molecule-electrode interaction, instead favouring molecule-molecule interactions, which in turn leads to additional physisorbed material which is more difficult to effectively rinse away.

Results of AFM scratch tests are shown in Figure 6.4. A different analysis approach is adopted in this chapter to account for the Au(111) samples. Since the Au(111) surface is stepped, it cannot be assumed the underlying substrate is of constant average height and roughness, as has been done for TS-Au in previous chapters. Also, due to the healing effect of SAMs, it is difficult to isolate single plateaus on the Au(111) surface to use the histogram method. Instead, a height profile is used to compare the surface immediately before and after the walls of a scratch. The width of the height profiles are shown in the centre column of Figure 6.4. In each case they span the length of a scratched edge. The corresponding

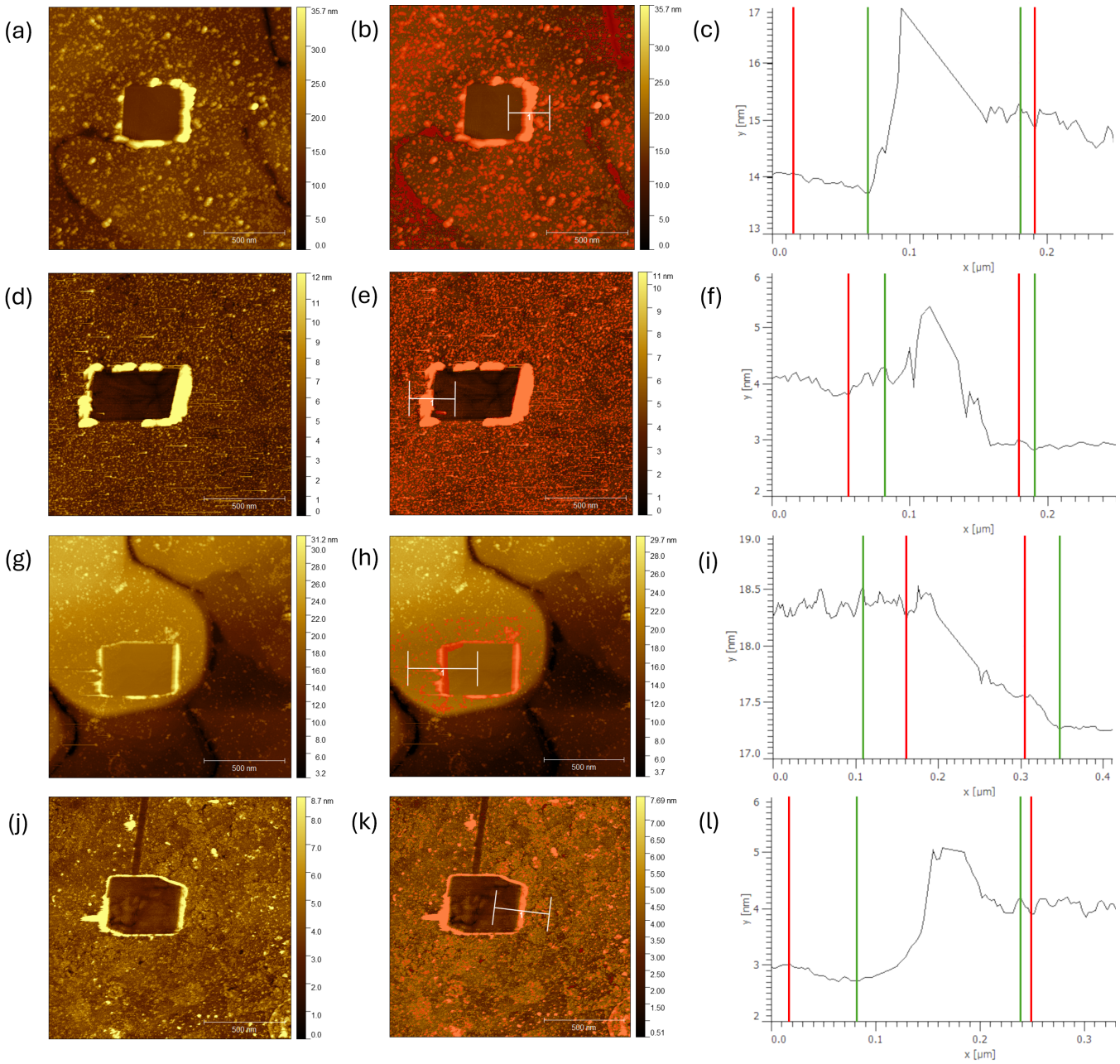

Figure 6.4: AFM topography images showing the scratched area, masking with profile lines and corresponding height profiles for (a-c) molecule **6A** on Au(111), (d-f) molecule **6A** on TS-Au, (g-i) molecule **6B** on Au(111), (j-l) molecule **6B** on TS-Au. The red lines indicate the smallest height estimate for the layer height and the green lines indicate the largest height estimate.

height profiles average all the rows within that range. The maximum and minimum layer heights are then chosen from the profiles, indicated by the green and red lines respectively. The quoted layer height is the average value of these extremes, with uncertainties reflecting the full range of possibilities. For the TS-Au samples, the histogram method was used to determine the level of masking needed, as in previous chapters. A mask is applied to cut off the top end of the histogram distribution, such that the mean height rests at the histogram peak. It also confirms that the layer height using the histogram method is contained within the uncertainty of the height profile method. For the Au(111) samples, due to the consistency of the SAM on the flat substrate, the areas of additional growth are clear so can all be masked out. The layer heights for each sample are shown in Table 6.1.

Sample	Layer Height nm
Molecule **6A** on Au(111)	1.2 ± 0.4
Molecule **6A** on TS-Au	1.2 ± 0.4
Molecule **6B** on Au(111)	1.0 ± 0.3
Molecule **6B** on TS-Au	1.2 ± 0.4

Table 6.1: Average layer heights for molecules **6A** and **6B** on Au(111) and TS-Au surfaces. The heights and uncertainties are determined from the red and green lines in Figure 6.4, as detailed above.

With each molecule having a length of 1.9 nm, these layer heights are all reasonable for a well-formed SAM. With a height of over 1 nm after masking, these molecules are forming a standing SAM under the areas of physisorbed extra growth, and must therefore be experiencing anchor coordination to the surface. Still, the binding component of the S 2p region in the XPS spectra is remarkably small. This highlights the quantity of physisorbed material, potentially exaggerated through signal attenuation since the photoemission of electrons at the electrode surface now

have significantly more material to travel through. This is especially true for a high coverage of physisorbed material, as is the case for molecule **6A** more so than molecule **6B**.

Conductive AFM was carried out as described in Section 6.2.3. For each sample, over 10,000 I-V traces are collected across at least 3 areas on the sample surface. After the open-circuit and gold contact measurement are filtered out, 2D histograms of the differential conductance are plotted. The results are shown in Figure 6.5. From these, the low bias conductance for each molecular junction can be obtained. These values are given in Table 6.2.

Sample	Conductance $\log(G/G_0)$
Molecule **6A** on Au(111)	-3.2 ± 0.7
Molecule **6A** on TS-Au	-3.4 ± 1.1
Molecule **6B** on Au(111)	-2.3 ± 0.4
Molecule **6B** on TS-Au	-2.8 ± 0.7

Table 6.2: Measured average conductance values at low bias for each sample. The uncertainties given are the standard deviation of the histograms shown in Figure 6.5. Standard deviation is calculated by $\frac{\text{FWHM}}{2\sqrt{2\ln 2}}$.

The electrical properties of molecules **6A** and **6B** have already been investigated in a previous study [137]. This was discussed in Section 3.2.3.5. In that study, Wang *et. al.* found the conductance of a SAM of molecule **6B** to be 10.2 times greater than that of molecule **6A**. This agrees with the results here, where it can be seen the average conductance of molecule **6A** is around an order of magnitude lower than that of molecule **6B**.

The uncertainties in these measurements are fairly large due to the instability of the

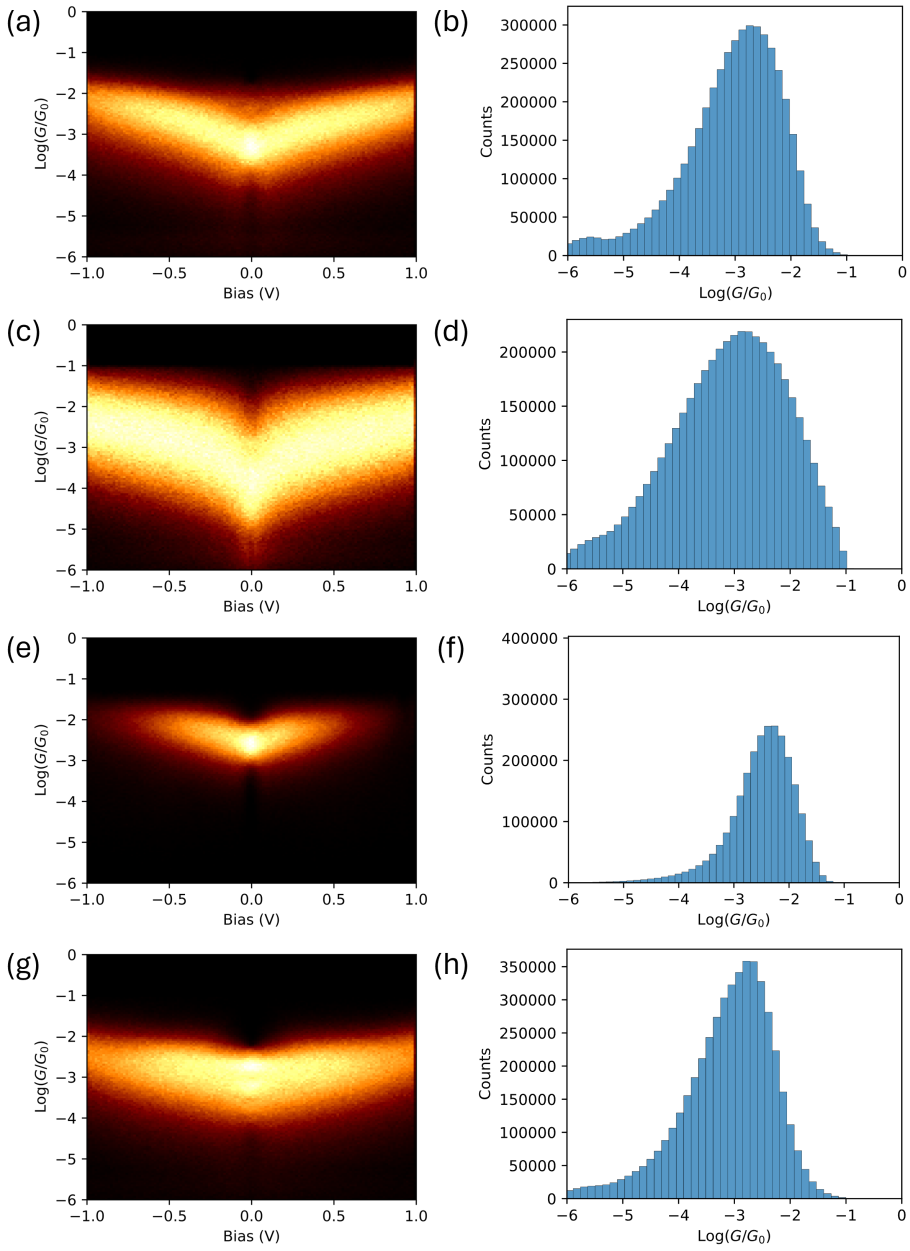

Figure 6.5: 2D histogram G-V plots and corresponding 1D histograms showing the spread of conductance values. (a-b) molecule **6A** on Au(111), (c-d) molecule **6A** on TS-Au, (e-f) molecule **6B** on Au(111) and (g-h) molecule **6B** on TS-Au. Each data set is created from over 10,000 I-V traces across at least 3 areas on the sample, with open-circuit and gold contact measurements filtered out. Brighter areas in the 2D histograms represent a higher count.

junction. The junction and the molecules within constantly change due to factors such as thermal and laser drift. By recording a large number of measurements, a large spread of results are recorded. This is exacerbated with extra physisorbed material, as this provides another mechanism for the junction to change during measurement. The uncertainties for molecule **6A** are therefore larger than **6B** due to this extra growth. The standard deviation in the Au(111) samples is much less than that of the TS-Au samples for both molecules. This is visualised in Figure 6.5, where the width of the band is tighter on the Au(111) samples compared to the Ts-Au result. The full 1D histograms shown also illustrate the variance in spread. This is compelling evidence for a greater consistency in the SAM when grown on a Au(111) surface. With the molecules better aligned in the layer, the variation in different contributions to transport through the junction reduces. Additionally, with more disordered films exhibiting an increased compressibility [204], the layer should deform less from tip-sample forces on Au(111), increasing the stability and consistency of the junction.

The conductances of both layers grown on Au(111) are greater than their TS-Au counterparts. Although, there must be caution in this conclusion since the mean values overlap within one standard deviation. As discussed earlier in Section 6.1, this could either be due to better alignment of the moderated transmission function resonances with the Fermi energy of the electrodes; or simply that more molecules are being contacted by their top anchor due to better packing and ordering, so more molecules are contributing to transmission through the junction. Unfortunately, Seebeck measurements of these junctions have not yet been performed. This is the next and most pressing step towards completion of this project.

6.4 Molecular Templating

The first step towards creating a multilayer structure of ZnPc and molecule **6C** was choosing the correct solvent. Since solution self-assembly was being used for the deposition of molecule **6C**, the solvent had to both dissolve the molecule so a high-quality SAM could be grown and not disrupt the ZnPc layer already deposited on the gold substrate. Toluene works well as a solvent for the self-assembly process of molecule **6C**, however a previous student had shown toluene destroys the ZnPc template layer. As discussed in Section 6.2.1, this is thought to be due to the aromatic ring in toluene allowing for a strong interaction with the ZnPc. Two readily available solvents were chosen next which did not have such aromatic rings: chloroform and acetone. The ZnPc layers were grown by deposition of a thick film before annealing at 400°C as described in Section 6.2.1. This method is employed to ensure a neat layer, as typically the second layer begins forming before the first layer is complete. The remaining ZnPc are lying down on the surface in either a monolayer or bilayer [209]. One example of the resulting layer is shown in Figure 6.6a, which gives a layer height of 0.8 ± 0.1 nm. The zinc atom within the ZnPc has been shown to sit 0.23 nm above the substrate surface [210] using XSW, and a monolayer of metalated phthalocyanine has been estimated to have a thickness of 0.34 nm using the attenuation of XPS intensities during deposition [211]. The layer height is therefore likely indicative of a bi-layer remaining post-deposition, however the AFM could be overestimating the layer height due to additional effects which would not impact other techniques such as XPS. The out-of-plane π-system would interact with the probe higher than that above the substrate surface, for example, which would artificially enhance the measured molecular height.

Two of these thin ZnPc layers were formed and separately placed in acetone and chloroform for 2 hours. Samples were then taken out, dried with nitrogen gas before being heated at 35 °C for an hour in a vacuum oven. They were then investigated with AFM, as shown in Figure 6.6, and XPS where the Zn 2p regions could be

directly compared to monitor the chemical change in the layer, as shown in Figure 6.7 .

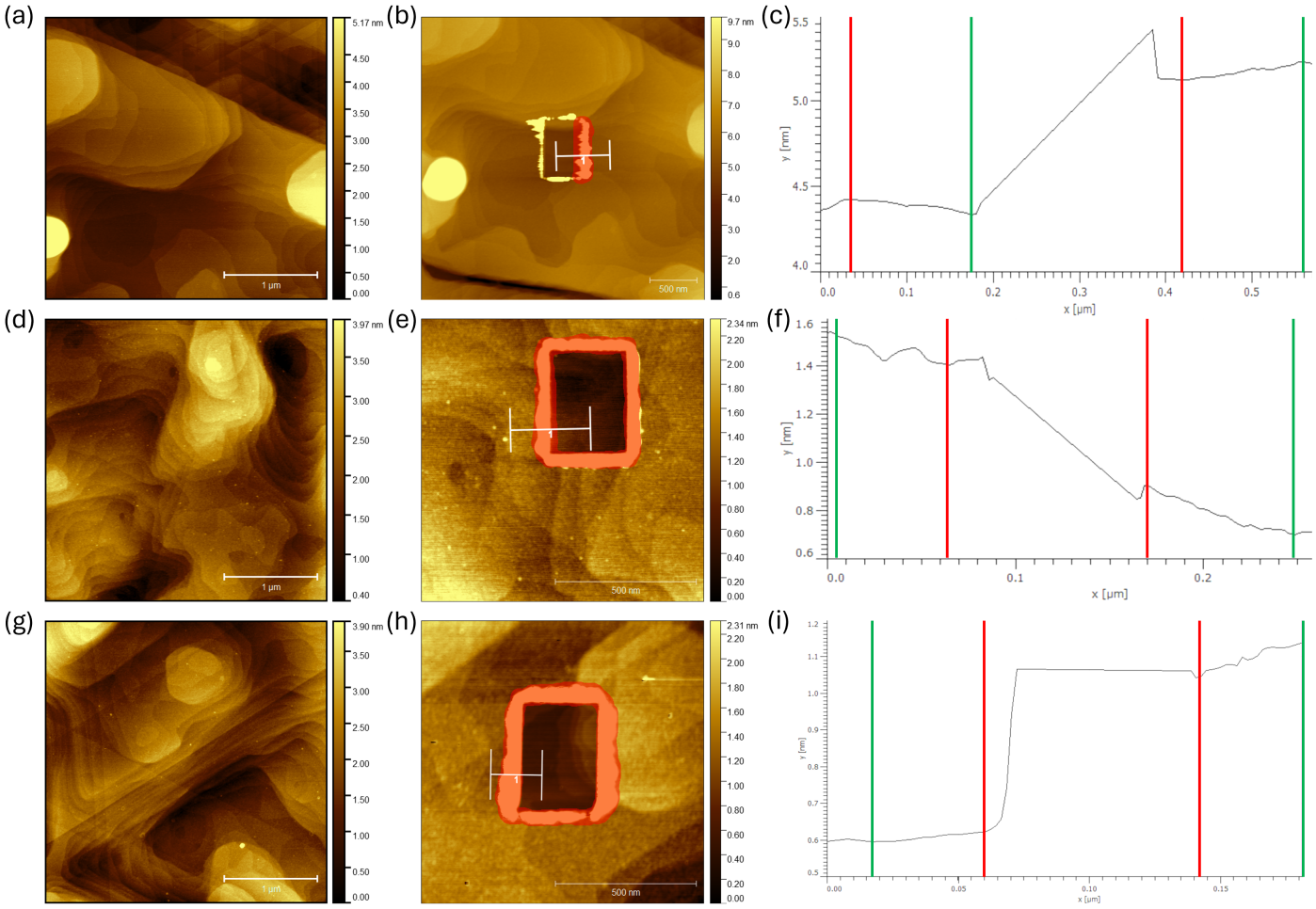

Figure 6.6: AFM topography showing a large 3 μm X 3 μm area, a scratched area and corresponding height profiles for the ZnPc layers. The samples are (a-c) a control ZnPc layer which has not been immersed in solvent, (d-f) a ZnPc layer after immersion in acetone, (g-i) a ZnPc layer after immersion in chloroform.

From Figure 6.6, layer heights of 0.8 ± 0.1 nm, 0.7 ± 0.2 nm and 0.5 ± 0.1 nm are obtained for the control sample, immersion in acetone and immersion in chloroform respectively. Both show a slight reduction in thickness, chloroform more than acetone, but both clearly retain their layer. The AFM image in each case shows

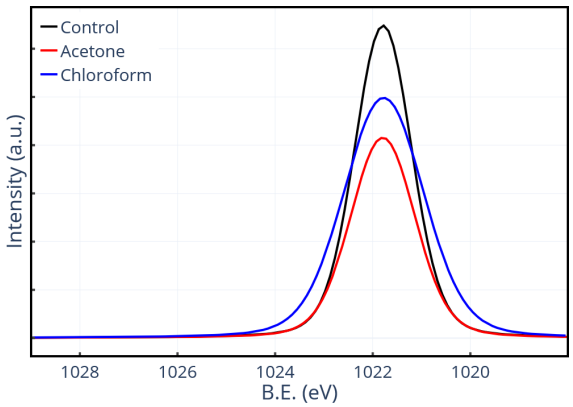

Figure 6.7: XPS fits of the Zn 2p region for the control, acetone and chloroform ZnPc samples. The spectra have each has their background signals removed before being overlaid to the same window.

the layer remains neat with no obvious holes or other destruction film. The XPS in Figure 6.7 shows a similar slight drop in zinc signal in both cases, with acetone dropping more than chloroform. These results signify that either acetone or chloroform would be a suitable candidate solvent which should retain the structure of the underlying ZnPc template through a long immersion during a self-assembly process of another molecule.

Next, molecule **6C** is investigated. For both solvent cases, as well as toluene as a solvent known to work for molecule **6C**, a 1 mMol solution was created and deposition was carried out as described in Section 6.2.1. The molecule did not appear to dissolve properly in acetone, with grains remaining despite prolonged sonication and slight heating to 35 °C. Despite this, a deposition was carried out regardless. A TS-Au substrate was used for the acetone and chloroform solutions, while Au(111) was used for the toluene to provide an ideal SAM to compare against. The results are shown in Figure 6.8.

The thickness of the toluene sample on Au(111) is 1.0 ± 0.3 nm. The thickness of the acetone and chloroform samples are 0.2 ± 0.1 nm and 0.9 ± 0.5 nm respectively.

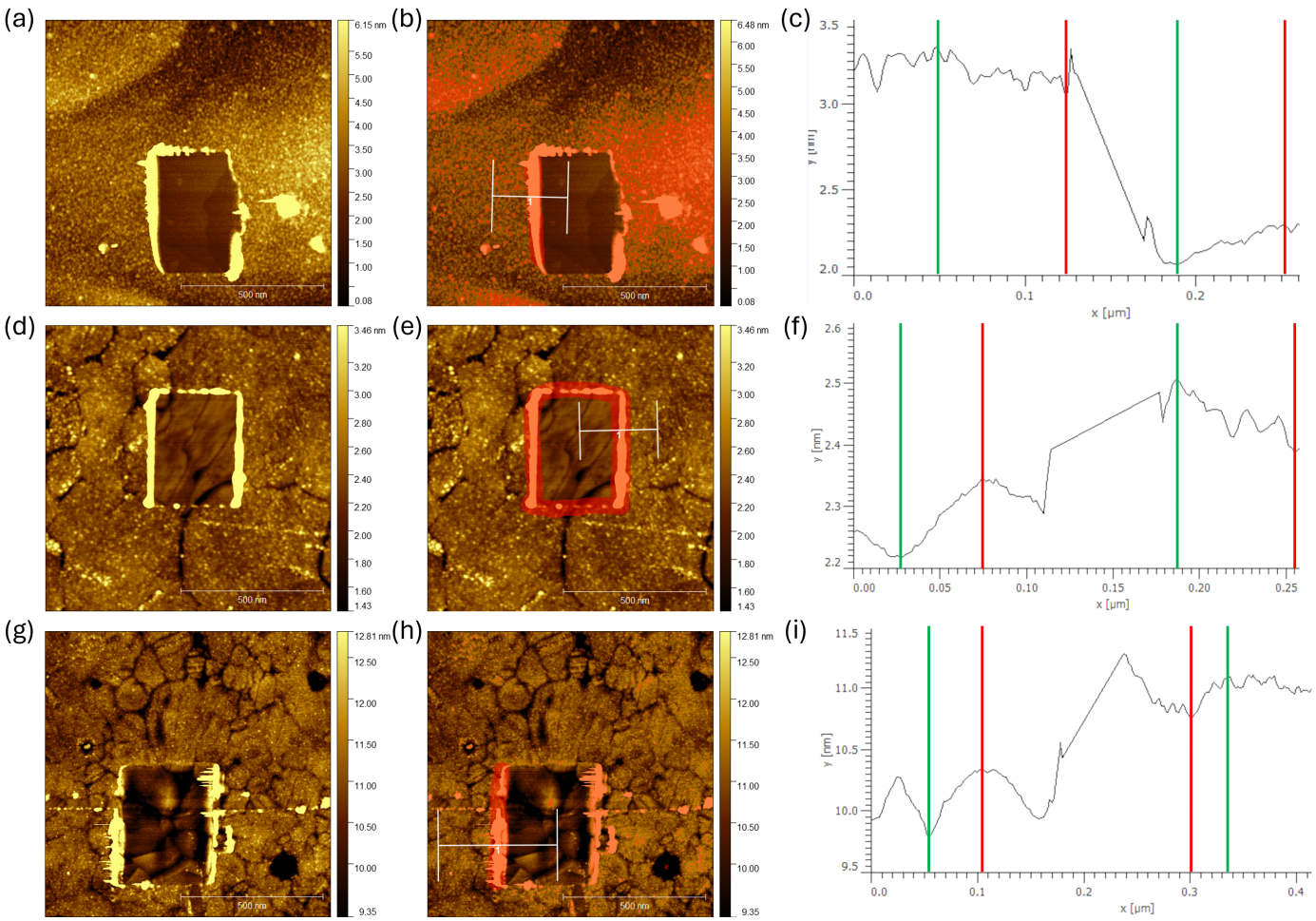

Figure 6.8: AFM topography showing the scratched area, masking with profile lines and corresponding height profiles for SAMs of molecule **6C** grown with different solvents. (a-c) toluene on Au(111), (d-f) acetone on TS-Au, (g-i) chloroform on TS-Au.

The uncertainty in the thickness for the chloroform sample is largely due to the underlying roughness of the TS-Au, which appears to be a particularly rough piece. As can be seen in the AFM image, the SAM itself does not show much additional physisorbed growth, usually the cause of high uncertainties. The acetone sample has not formed a standing SAM. The layer is very thin, indicative of molecules lying on the surface. This problem will likely improve given extra time to assemble, however the immersion time should be kept as short as possible to help preserve the ZnPc

layer. Since the molecule did not appear to dissolve properly in acetone anyway, and the chloroform sample worked sufficiently well for the desired immersion time, chloroform was selected as the solvent to proceed with for the combined deposition samples.

A thin ZnPc layer is created as before, and XPS is performed to use for comparison later. The sample is then cut in half, one half was placed in a solution of molecule **6C** in chloroform, the other in a solution of molecule **6D** in chloroform. Both followed the usual deposition process of a 5 hour total deposition time, with a chloroform rinse after each hour before a final dry with nitrogen gas. XPS is then utilised again, to look for a shift in the Zn 2p peaks indicative of N-Zn coordination from the pyridine anchors coordinating to the metal centre. In the results, shown in Figure 6.9, a positive shift of 0.3 eV can be seen for molecule **6C** (red) compared to the thin ZnPc pre-solution self-assembly (black) and molecule **6D** (blue), which AFM confirmed did not properly assemble. A similar positive shift in binding energy is seen in a previous study which used ZnTPP assembled onto a SAM of molecule **6C** [116].

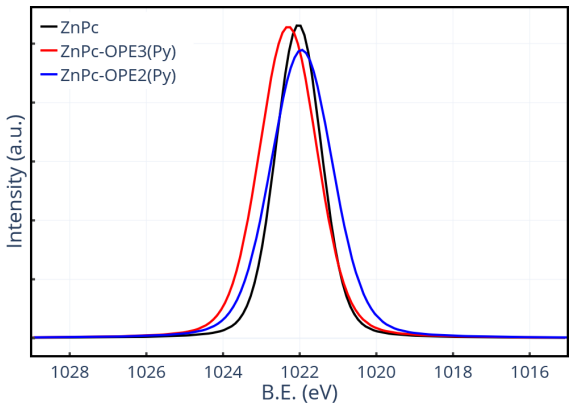

Figure 6.9: XPS fits of the Zn 2p region for the thin ZnPc layer, as well as additional assemblies of OPE3Py (molecule **6C**) and OPE2py (molecule **6D**). The spectra have each has their background signals removed before being overlaid to the same window.

The AFM is shown in Figure 6.10. While both large area images appear to

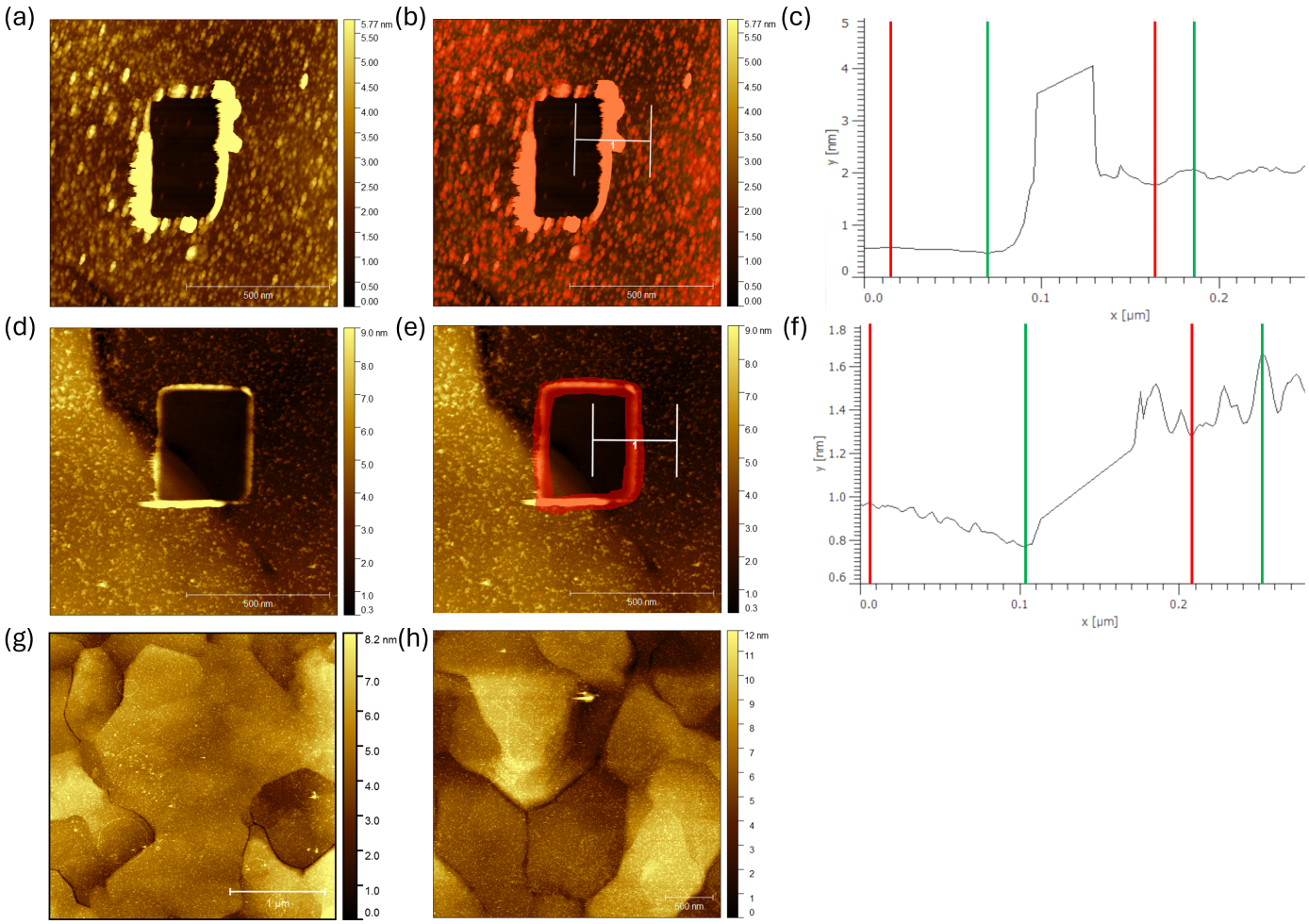

Figure 6.10: AFM topography showing the scratched area, masking with profile lines and corresponding height profiles for SAMs of multilayer structures using ZnPc as a template layer. (a-c) assembly of molecule **6C** (d-f) assembly of molecule **6D**. Large 3 μm X 3 μm areas are also shown for (g) molecule **6C** and (h) molecule **6D**.

show a full coverage of the SAMs onto the ZnPc template, closer inspection to the scratches reveal otherwise. The layer heights obtained from Figure 6.10c,f are 1.4 ± 0.2 nm and 0.6 ± 0.3 nm for the molecule **6C** and **6D** depositions respectively. The height for the molecule **6D** structure corresponds to the results from the ZnPc layer after immersion in chloroform, with a small increase from the specs of physisorbed material which can be seen across the surface. This implies the layer imaged is just the ZnPc, with patches of physisorbed molecule **6D** which has not coordinated

to the zinc centres. The height of the multilayer structure formed from molecule **6C** corresponds to the thickness of the ZnPc layer after chloroform immersion in addition to the thickness of the layer of molecule **6C** grown on TS-Au using the chloroform solvent. There is also physisorbed material on top of this templated SAM, which has been masked out for the purposes of calculating the layer height as shown in Figure 6.10b. The presence appears to be exaggerated somewhat from apparent tip artifacts in the image. Physisorbed material of both molecules **6C** and **6D** may occur as the aromatic rings within the OPE backbone likely interact with the π-system above the ZnPc. This would be enhanced for molecule **6C** which has an extra ring, leading to a stronger interaction and therefore a greater difficulty in rinsing excess molecule away.

CAFM was performed as described in Section 6.2.3. As a comparison point, the sample of molecule **6C** grown on Au(111) using toluene as a solvent was measured. This was earlier shown to make a good SAM, and is being used as the optimal case for a molecular junction using molecule **6C**. The sample of molecule **6C** grown on TS-Au using a chloroform solvent is also measured as an additional comparison point. Finally, the multilayer structure of a SAM of molecule **6C** grown onto a ZnPc molecular template on Au(111) is investigated. In each case, over 10,000 I-V traces are collected across at least three areas on the sample surface. The results are shown in Figure 6.11, with corresponding low bias conductance values of the junction given in Table 6.3.

Firstly, it is difficult to draw conclusions from the relative conductance values as they are all similar and overlap with one standard deviation. With this in mind, there is an approximate trend to improved conductance on the flatter substrate, and further improved conductance with the ZnPc templating. This is consistent with the trend observed for molecule **6A** and **6B** observed in the previous section. The

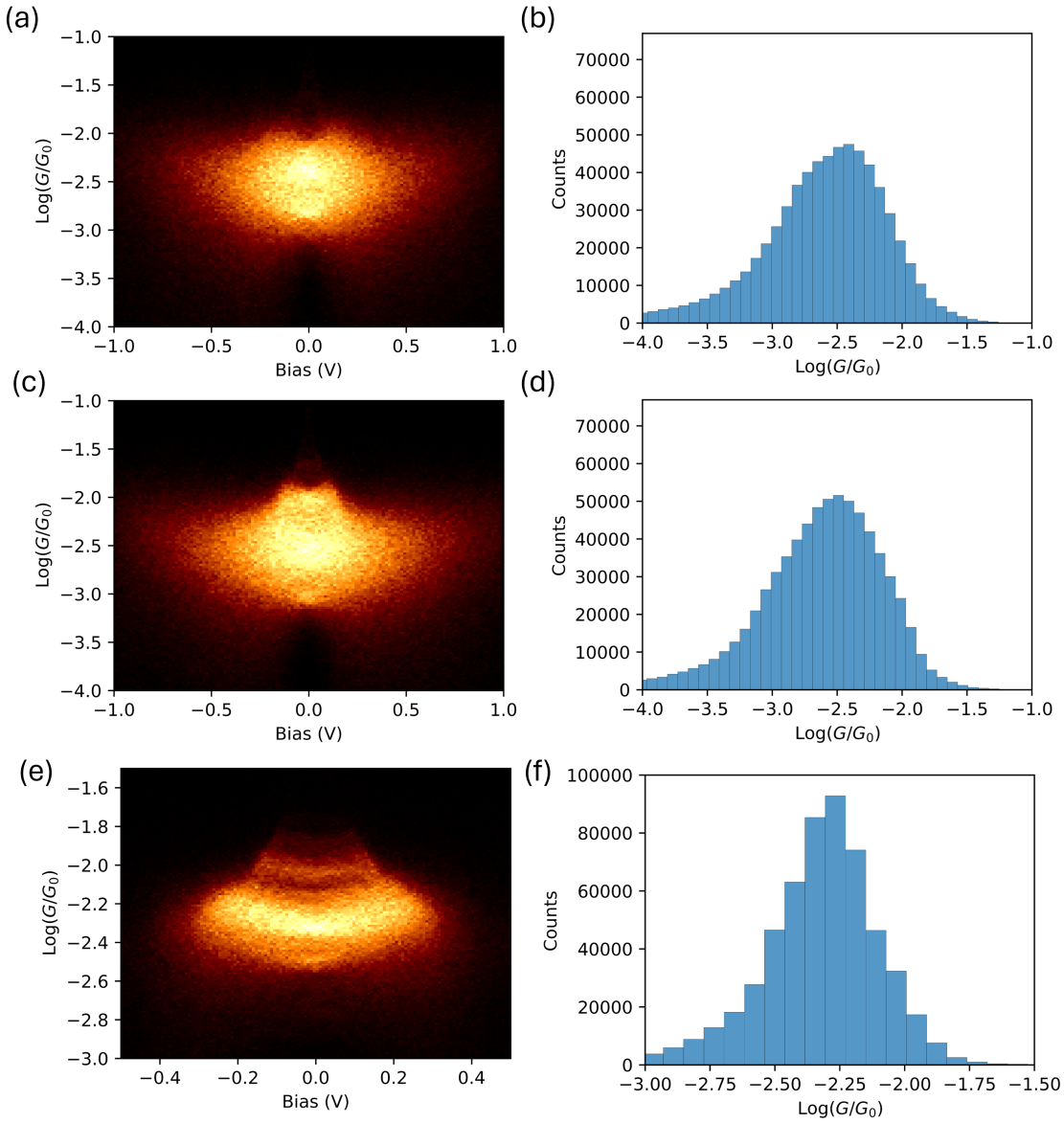

Figure 6.11: 2D histogram G-V plots and corresponding 1D histograms showing the spread of conductance values. (a-b) molecule **6C** on Au(111) using a toluene solvent, (c-d) molecule **6C** on TS-Au using a chloroform solvent, (e-f) molecule **6C** on a ZnPc template layer, grown on Au(111). Each data set is created from over 10,000 I-V traces across at least 3 areas on the sample, with open-circuit and gold contact measurements filtered out. Brighter areas in the 2D histograms represent a higher count.

Sample	Conductance $\log(G/G_0)$
Molecule **6C** on Au(111)	-2.4 ± 0.4
Molecule **6C** on TS-Au	-2.5 ± 0.4
Molecule **6C** + ZnPc	-2.3 ± 0.2

Table 6.3: Measured average conductance values of the junction at low bias for each sample. The uncertainties given are the standard deviation of the histograms shown in Figure 6.11. Standard deviation is calculated by $\frac{\text{FWHM}}{2\sqrt{2\ln 2}}$.

standard deviations of the measurements over the Au(111) and TS-Au substrates are the same, in contrast to the clear improvement with a more ordered surface as demonstrated earlier in this chapter. This is likely due to the increased molecule-molecule interactions involved with molecule **6A** and **6B** from the π-systems due to the anthracene cores. This promotes competition between molecule-molecule interactions and molecule-surface interactions. The more a molecule is forced to conform to its neighbours rather than the surface, the less consistent the coupling is to the surface. This becomes especially prominent for a rougher surface, further increasing the spread of conductances measured in the molecular junctions. Here, the standard deviations are the same, implying more robust SAMs can be formed on rougher surfaces as the molecule-molecule interactions decrease.

The standard deviation of the templated layer is distinctly lower. This is especially clear in the histograms in Figure 6.11 which show a tighter distribution. This implies a much improved stability of the molecular junction. The SAM appears more robust and more consistent with the use of a molecular template to promote ordering by providing strict binding sites for the assembling molecule to coordinate to. During measurements, while the low bias conductance is similar to that of the non-templated SAMs, the current quickly saturates to maximum as the magnitude of the applied bias increases. This is seen by the cut-off in data points at more than

$\pm$ 0.4 V in Figure 6.11e. A rapid increase in current compared to the non-templated SAMs with an increase in bias in either polarity implies a narrowing of the HOMO-LUMO gap. The addition of ZnPc appears to be decreasing the HOMO-LUMO gap for the combined molecular structure in the junction, which would increase the conductance slightly as a result. This is how a previous study, discussed in Chapter 5, maintained a good conductance through increased molecular length in fused-porphyrin molecules [180]. While the conductance would normally drop with length, if the HOMO-LUMO gap is decreased then conductance is boosted, so no overall drop is observed. This should also mean the Fermi energy is closer to a resonance in the transmission function, so the Seebeck coefficient should also see a boost as the slope is increased. Unfortunately, Seebeck measurements have not yet been performed on a multi-component templated SAM to confirm this.

6.5 Conclusions and Future Work

The effect of the substrate quality has been shown to make an impact in the quality of the SAM layer grown. While the thickness of the layers remained unchanged, the conductances for junctions containing molecules **6A** and **6B** displayed a greater consistency in the SAMs grown on a flatter substrate. There also appears to be a slight increase in conductance with an improved surface, which could be due to a change in the shape of the transmission function from improved molecular alignment, or a universal shift upwards from increasing the number of molecules in the junction participating in transmission.

A multi-component structure utilising a ZnPc molecular template was achieved through a combination of thermal evaporation in UHV and solution self-assembly techniques. Molecule **6C** successfully coordinated to the zinc centres in the ZnPc template layer, as evidenced by the shift in the Zn 2p binding energies from XPS and the increased layer thickness from AFM. To do this, a neat thin film of ZnPc

had to be created by thick layer deposition followed by thermal annealing. This layer had to survive the self-assembly process by identifying a solvent which was both suitable for the medium of self-assembling molecule **6C**, and non-interactive to the ZnPc. The result is a layer which exhibits a clear improvement in junction stability as well as a slightly increased conductance by narrowing the HOMO-LUMO gap. The next step for both of these projects is to carry out Seebeck measurements on similar successful samples. As was the initial motivation for this project, the Seebeck coefficient should improve as molecular ordering improves. This project has so far shown the charge transport through a SAM can be altered by surface roughness alone. The consistency of molecular junctions can be improved with a better quality substrate, and further boosted with the use of a molecular template. Knowledge of the effect of surface quality on the thermoelectric output could be crucial to improving device fabrication. Much time and expense would be needed to improve the surface roughness for current device concepts designed to be scalable. Quantification of the potential thermoelectric improvements due to surface quality would be needed to investigate whether the resource cost is warranted. If the impact of surface quality is large, molecular templating could provide a solution to the scalability problem of atomically flat surfaces, producing a standardised layer which could consistently improve molecular packing and alignment.

Chapter 7

Conclusions and Future Work

The work presented in this thesis tackles two main topics: thermoelectric and memristive properties in self-assembled monolayers. For the former, surface interactions and their effect of the measured thermopower of the molecular films if the focus. Chapter 4 presents the idea that electrically similar molecules, in both design and performance, can exhibit vastly different thermoelectric properties. Two of the molecules have free alkyne arm groups which can interact with the surface as the molecule tilts. The third molecule was used as a control as it was a cross-linked version with no free arms to interact with the surface. Measurement of the Seebeck coefficient confirmed a negative sign for the cross-linked variety while the others were found to have a positive sign. This agrees with density functional theory (DFT) calculations which predict an inversion of the Seebeck polarity when alkyne co-binding occurs, as opposed to a consistently negative Seebeck coefficient for each molecule when surface binding occurs exclusively through the indented anchor groups. The shift in the transmission function is caused only by the molecule-surface interaction, without any chemical changes. The shift was dramatic enough to change the molecular junctions from n-type to p-type. Future work on this project includes on-surface cross-linking of the molecules using halogenated ends on the arm groups. This should improve the stability of the junctions for electrical measurements and evidence the alkyne co-binding theory by showing another inversion of the Seebeck polarity.

Additional studies on the effect of surface interactions on the thermopower in a molecular films were also conducted in Chapter 6. One study compared the electrical measurements of identical molecules grown on surfaces with different roughnesses. The layers grown on flatter substrates displayed a greater consistency in the measured conductances, reflected in the reduced standard deviations of the measured values. This is likely due the molecules assembling as a more robust and homogeneous layer, limiting the variation of the molecular junction as the probe naturally drifts along the sample. Additionally, a small increase in the conductance

was observed with a flatter substrate. This could either be due to a change in the transmission function due to improved molecular alignment, or simply due to extra molecules being able to be contacted by the top electrode and participating in the transmission. This idea was built upon with the inclusion of a zinc phthalocyanine (ZnPc) molecular template. A multilayer structure using a ZnPc template for a highly conjugated molecule was created using a combination of thermal evaporation and solution self-assembly. A successful structure was confirmed by XPS and AFM, and exhibited a greatly improved junction stability for the electrical measurements, and a yet further slight improvement in the measured conductance. These projects show that the charge transport through a molecular film can be altered by surface roughness alone, and improved with the use of a molecular templating layer. The next step in both of these projects is to perform Seebeck coefficient measurements. Improved molecular alignment should create sharper features in the transmission function over the junction, resulting in a boost to the Seebeck coefficient.

The other aspect of this thesis was an investigation into the potential memristive properties of an edge-fused porphyrin dimer, carried out in Chapter 5. Despite the SAMs forming consistently similar layers as measured by AFM, the electrical properties of different samples was inconsistent. Each sample remained incredibly consistent within itself over many I-V traces and multiple areas. Potential memristive behaviour in the form of hysteresis between the trace and retrace in the I-V sweeps was found in three of the six samples measured. With limitations in the current range which was able to be measured, it cannot be said whether the three unsuccessful samples did not undergo switching or if significant features at higher biases were hidden. Regardless, additional samples should be created to accommodate for the inconsistency of the samples presented here. Graphene capping proved to be a excellent method of enhancing the hysteresis effect. The stability of the junction is even further increased and many more molecules are contacted by the flake to participate in transport, increasing the effective number of molecules in

the junction. The graphene capped sample showed a larger hysteresis loop which spanned a greater bias range. Graphene may be an important aspect to facilitating the reaction due to the shallower work function when compared to a platinum top electrode. Therefore, future samples made using this molecule should also undergo graphene capping. While a sample may initially show no memristive behaviour, the addition of a graphene top layer may reveal effects which were previously hidden.

While much of the field of molecular electronics focusses on molecular design to enhance the desired electrical or thermoelectrical properties, the projects in this thesis highlight the importance of the environment in which those molecules are assembled. In particular, the impact of the molecule-electrode interface and the surface interactions which occur there. This ranges from large changes of the expected Seebeck due to additional surface interactions which could alter the functionality of a potential device, to a more precise optimisation of the potential output from an improvement in surface roughness. Such knowledge can be fed back into the wider community, where future molecular designs and their initial simulations should consider potential alternative surface interaction combinations, or where the benefits of a smoother electrode are known for device implementation. Electrode choice for memristive molecules appears to be essential to optimising the output of a memristive junction. While the graphene flake enhanced the memristive effect due to an increased number of effective molecules in the junction, it likely also facilitates switching with its shallower work function or increased gating from non-transporting molecules within the junction. Further work should be conducted to fully expose the mechanisms of the benefits the graphene caps provide. Also, additional work is needed to highlight the potential enhancements in thermoelectric performance from improved electrode quality.

Bibliography

[1] Richard Feynman. There's plenty of room at the bottom. In *Feynman and computation*, pages 63–76. CRC Press, 2018.

[2] BA Joyce and RR Bradley. A study of nucleation in chemically grown epitaxial silicon films using molecular beam techniques i.—experimental methods. *Philosophical Magazine*, 14(128):289–299, 1966.

[3] Wagma Hidayat and Muhammad Usman. Applications of molecular beam epitaxy in optoelectronic devices: an overview. *Physica Scripta*, 99(11):112002, 2024.

[4] Gerd Binnig, Heinrich Rohrer, et al. Scanning tunneling microscopy. *Helv. Phys. Acta*, 55(6):726–735, 1982.

[5] Gerd Binnig, Calvin F Quate, and Ch Gerber. Atomic force microscope. *Physical review letters*, 56(9):930, 1986.

[6] Arieh Aviram and Mark A Ratner. Molecular rectifiers. *Chemical physics letters*, 29(2):277–283, 1974.

[7] Hoesung Lee, Katherine Calvin, Dipak Dasgupta, Gerhard Krinner, Aditi Mukherji, Peter Thorne, Christopher Trisos, José Romero, Paulina Aldunce, Ko Barrett, et al. *Climate change 2023: synthesis report. Contribution of working groups I, II and III to the sixth assessment report of the intergovernmental panel on climate change*. 2023.

[8] Abram Fedorovich Ioffe, LS Stil'Bans, EK Iordanishvili, TS Stavitskaya, A Gelbtuch, and George Vineyard. Semiconductor thermoelements and thermoelectric cooling. *Physics Today*, 12(5):42–42, 1959.

[9] Eric G Wood, Jennifer A Herman, Ronald A Hall, Andrew W Mitchell, Paul M Stella, and Thomas I Valdez. Multi-mission radioisotope thermoelectric generator experience on mars. Technical report, 2016.

[10] NASA Jet Propulsion Laboratory and NASA Science. Mars 2020 perseverance rover's multi-mission radioisotope thermoelectric generator (mmrtg). `https://science.nasa.gov/resource/441839/`, 2025.

[11] Taolin Zhao, Xin Li, Weiming Wu, Jialin Gu, Yunze Han, and Xian Tang. Enhancing the thermoelectric properties and delaying their attenuation in n-type sige alloy through sic nanoparticle doping. *ACS omega*, 10(28):30023–30030, 2025.

[12] Jing-jing Feng, Wei Zhu, and Yuan Deng. An overview of thermoelectric films: Fabrication techniques, classification, and regulation methods. *Chinese Physics B*, 27(4):047210, 2018.

[13] Said Hamdioui, Lei Xie, Hoang Anh Du Nguyen, Mottaqiallah Taouil, Koen Bertels, Henk Corporaal, Hailong Jiao, Francky Catthoor, Dirk Wouters, Linn Eike, et al. Memristor based computation-in-memory architecture for data-intensive applications. In *2015 Design, Automation & Test in Europe Conference & Exhibition (DATE)*, pages 1718–1725. IEEE, 2015.

[14] Arm Ltd. Powering the edge: Machine learning at the edge. Technical report, Arm Ltd., 2019.

[15] Deepak Sharma, Santi Prasad Rath, Bidyabhusan Kundu, Anil Korkmaz, Harivignesh S, Damien Thompson, Navakanta Bhat, Sreebrata Goswami, R Stanley Williams, and Sreetosh Goswami. Linear symmetric self-selecting 14-bit kinetic molecular memristors. *Nature*, 633(8030):560–566, 2024.

[16] https://ch301.cm.utexas.edu/imfs/mo/mo-theory-all.php.

[17] Jin Zhong Zhang, Jinghong Li, Yat Li, and Yiping Zhao. *Hydrogen generation, storage and utilization*. John Wiley & Sons, 2014.

[18] Gao Yang, Lihua Li, Wing Bun Lee, and Man Cheung Ng. Structure of graphene and its disorders: a review. *Science and technology of advanced materials*, 19(1):613–648, 2018.

[19] Peter W Atkins and Ronald S Friedman. *Molecular quantum mechanics*. Oxford university press, 2011.

[20] NW Ashcroft and ND Mermin. Solid state physics, holt, rinehart and winston. *New York*, 2005:403, 1976.

[21] Norbert Koch. Organic electronic devices and their functional interfaces. *ChemPhysChem*, 8(10):1438–1455, 2007.

[22] Hisao Ishii, Kiyoshi Sugiyama, Eisuke Ito, and Kazuhiko Seki. Energy level alignment and interfacial electronic structures at organic/metal and organic/organic interfaces. *Advanced materials*, 11(8):605–625, 1999.

[23] Georg Heimel, Lorenz Romaner, Jean-Luc Brédas, and Egbert Zojer. Interface energetics and level alignment at covalent metal-molecule junctions:¡? format?¿ π-conjugated thiols on gold. *Physical review letters*, 96(19):196806, 2006.

[24] Joseph A Stroscio and William J Kaiser. *Scanning tunneling microscopy*, volume 27. Academic press, 1993.

[25] Jascha Repp, Gerhard Meyer, Sladjana M Stojković, André Gourdon, and Christian Joachim. Molecules on insulating films: scanning-tunneling microscopy imaging of individual molecular orbitals. *Physical Review Letters*, 94(2):026803, 2005.

[26] Constant M Guédon, Hennie Valkenier, Troels Markussen, Kristian S Thygesen, Jan C Hummelen, and Sense Jan Van Der Molen. Observation of quantum interference in molecular charge transport. *Nature nanotechnology*, 7(5):305–309, 2012.

[27] Gemma C Solomon, David Q Andrews, Randall H Goldsmith, Thorsten Hansen, Michael R Wasielewski, Richard P Van Duyne, and Mark A Ratner. Quantum interference in acyclic systems: Conductance of cross-conjugated molecules. *Journal of the American Chemical Society*, 130(51):17301–17308, 2008.

[28] Gregory Breit and Eugene Wigner. Capture of slow neutrons. *Physical review*, 49(7):519, 1936.

[29] Colin John Lambert. *Quantum Transport in Nanostructures and Molecules: An introduction to molecular electronics*. IoP Publishing, 2021.

[30] Troels Markussen, Robert Stadler, and Kristian S Thygesen. The relation between structure and quantum interference in single molecule junctions. *Nano letters*, 10(10):4260–4265, 2010.

[31] Ph Sautet and Ch Joachim. Electronic interference produced by a benzene embedded in a polyacetylene chain. *Chemical physics letters*, 153(6):511–516, 1988.

[32] Lanlan Sun, Yuri A Diaz-Fernandez, Tina A Gschneidtner, Fredrik Westerlund, Samuel Lara-Avila, and Kasper Moth-Poulsen. Single-molecule electronics: from chemical design to functional devices. *Chemical Society Reviews*, 43(21):7378–7411, 2014.

[33] David Michael Rowe. *Thermoelectrics handbook: macro to nano*. CRC press, 2005.

[34] Yi Wang, Yong-Jie Hu, Brandon Bocklund, Shun-Li Shang, Bi-Cheng Zhou, Zi-Kui Liu, and Long-Qing Chen. First-principles thermodynamic theory of seebeck coefficients. *Physical Review B*, 98(22):224101, 2018.

[35] H Julian Goldsmid et al. *Introduction to thermoelectricity*, volume 121. Springer, 2010.

[36] Hatef Sadeghi, Sara Sangtarash, and Colin J Lambert. Enhancing the thermoelectric figure of merit in engineered graphene nanoribbons. *Beilstein journal of nanotechnology*, 6(1):1176–1182, 2015.

[37] Munirah Alsaqer, Abdalghani HS Daaoub, Sara Sangtarash, and Hatef Sadeghi. Large mechanosensitive thermoelectric enhancement in metallo-organic magnetic molecules. *Nano Letters*, 23(23):10719–10724, 2023.

[38] GD Mahan and JO Sofo. The best thermoelectric. *Proceedings of the National Academy of Sciences*, 93(15):7436–7439, 1996.

[39] Jesse Maassen. Limits of thermoelectric performance with a bounded transport distribution. *Physical Review B*, 104(18):184301, 2021.

[40] Mario Wolf, Richard Hinterding, and Armin Feldhoff. High power factor vs. high zt—a review of thermoelectric materials for high-temperature application. *Entropy*, 21(11):1058, 2019.

[41] G Jeffrey Snyder and Eric S Toberer. Complex thermoelectric materials. *Nature materials*, 7(2):105–114, 2008.

[42] Hee Seok Kim, Weishu Liu, Gang Chen, Ching-Wu Chu, and Zhifeng Ren. Relationship between thermoelectric figure of merit and energy conversion efficiency. *Proceedings of the National Academy of Sciences*, 112(27):8205–8210, 2015.

[43] Dietmar Weinmann. The physics of mesoscopic systems. *Institut de physique et chimie des Materiaux de strasboury, 67037 Strasbourg Cedex France*, 2005.

[44] Liang-Yan Hsu and Herschel Rabitz. Theory of molecular conductance using a modular approach. *The Journal of Chemical Physics*, 145(23), 2016.

[45] Anders Mathias Lunde and Karsten Flensberg. On the mott formula for the thermopower of non-interacting electrons in quantum pointcontacts. *Journal of Physics: Condensed Matter*, 17(25):3879, 2005.

[46] Fabian Garmroudi, Michael Parzer, Alexander Riss, Cédric Bourgès, Sergii Khmelevskyi, Takao Mori, Ernst Bauer, and Andrej Pustogow. High thermoelectric performance in metallic niau alloys via interband scattering. *Science Advances*, 9(37):eadj1611, 2023.

[47] MX Chen and Raimund Podloucky. Electronic thermal conductivity as derived by density functional theory. *Physical Review B—Condensed Matter and Materials Physics*, 88(4):045134, 2013.

[48] Ali Lavasani, Daniel Bulmash, and Sankar Das Sarma. Wiedemann-franz law and fermi liquids. *Physical Review B*, 99(8):085104, 2019.

[49] Mohammed D Noori, Sara Sangtarash, and Hatef Sadeghi. The effect of anchor group on the phonon thermal conductance of single molecule junctions. *Applied Sciences*, 11(3):1066, 2021.

[50] Shubhaditya Majumdar, Jonatan A Sierra-Suarez, Scott N Schiffres, Wee-Liat Ong, C Fred Higgs III, Alan JH McGaughey, and Jonathan A Malen. Vibrational mismatch of metal leads controls thermal conductance of self-assembled monolayer junctions. *Nano letters*, 15(5):2985–2991, 2015.

[51] Liyuan Zheng, Erfan Norouzi Farahani, Abdalghani HS Daaoub, Sara Sangtarash, and Hatef Sadeghi. Rules of connectivity-dependent phonon interference in molecular junctions. *Nano Letters*, 25(16):6524–6529, 2025.

[52] Hatef Sadeghi. Quantum and phonon interference-enhanced molecular-scale thermoelectricity. *The Journal of Physical Chemistry C*, 123(20):12556–12562, 2019.

[53] Jan-Christopher Klöckner, Juan C Cuevas, and Fabian Pauly. Tuning the thermal conductance of molecular junctions with interference effects. *Physical Review B*, 96(24):245419, 2017.

[54] Longji Cui, Wonho Jeong, Sunghoon Hur, Manuel Matt, Jan C Klöckner, Fabian Pauly, Peter Nielaba, Juan Carlos Cuevas, Edgar Meyhofer, and Pramod Reddy. Quantized thermal transport in single-atom junctions. *Science*, 355(6330):1192–1195, 2017.

[55] Su Ying Quek, Maria Kamenetska, Michael L Steigerwald, Hyoung Joon Choi, Steven G Louie, Mark S Hybertsen, JB Neaton, and Latha Venkataraman. Mechanically controlled binary conductance switching of a single-molecule junction. *Nature nanotechnology*, 4(4):230–234, 2009.

[56] Mark A Reed, C Zhou, CJ Muller, TP Burgin, and JM Tour. Conductance of a molecular junction. *Science*, 278(5336):252–254, 1997.

[57] Mervyn Roy. The tight binding method. *Rutgers University*, 5:57, 2015.

[58] CJ Lambert. Basic concepts of quantum interference and electron transport in single-molecule electronics. *Chemical Society Reviews*, 44(4):875–888, 2015.

[59] TA Papadopoulos, IM Grace, and CJ Lambert. Control of electron transport through fano resonances in molecular wires. *Physical Review B—Condensed Matter and Materials Physics*, 74(19):193306, 2006.

[60] Haoyang Pan, Peiqi Yang, Yudi Wang, Jie Li, Shi Li, and Shimin Hou. A designing strategy for fano resonances in molecular junctions. *The Journal of Physical Chemistry C*, 127(27):13407–13413, 2023.

[61] CM Finch, VM Garcia-Suarez, and CJ Lambert. Giant thermopower and figure of merit in single-molecule devices. *Physical Review B—Condensed Matter and Materials Physics*, 79(3):033405, 2009.

[62] Byungjin Cho, Sunghun Song, Yongsung Ji, Tae-Wook Kim, and Takhee Lee. Organic resistive memory devices: performance enhancement, integration, and advanced architectures. *Advanced Functional Materials*, 21(15):2806–2829, 2011.

[63] Sven Möller, Craig Perlov, Warren Jackson, Carl Taussig, and Stephen R Forrest. A polymer/semiconductor write-once read-many-times memory. *Nature*, 426(6963):166–169, 2003.

[64] Qi-Dan Ling, Der-Jang Liaw, Chunxiang Zhu, Daniel Siu-Hung Chan, En-Tang Kang, and Koon-Gee Neoh. Polymer electronic memories: Materials, devices and mechanisms. *Progress in polymer science*, 33(10):917–978, 2008.

[65] Technical University of Munich (TUM). In-memory computing: Tum professor develops an energy-saving ai chip. `https://www.tum.de/en/news-and-events/all-news/press-releases/details/tum-professor-develops-an-energy-saving-ai-chip`, Oct 2023. Accessed: 2025-11-18.

[66] Ovidiu Vermesan, Franz Wotawa, Björn Debaillie, et al. *Industrial Artificial Intelligence Technologies and Applications*. Taylor & Francis, 2023.

[67] Taha Soliman, Swetaki Chatterjee, Nellie Laleni, Franz Müller, Tobias Kirchner, Norbert Wehn, Thomas Kämpfe, Yogesh Singh Chauhan, and Hussam Amrouch. First demonstration of in-memory computing crossbar using multi-level cell fefet. *Nature Communications*, 14(1):6348, 2023.

[68] imec-International. Cmos advanced compute accelerators. `https://www.imec-int.com/en/expertise/cmos-advanced/compute/accelerators`. Accessed: 2025-11-18.

[69] Sreetosh Goswami, Santi P Rath, Damien Thompson, Svante Hedström, Meenakshi Annamalai, Rajib Pramanick, B Robert Ilic, Soumya Sarkar, Sonu Hooda, Christian A Nijhuis, et al. Charge disproportionate molecular redox for discrete memristive and memcapacitive switching. *Nature nanotechnology*, 15(5):380–389, 2020.

[70] T Venkatesan, Sreebrata Goswami, R Stanley Williams, and Sreetosh Goswami. Entrenching decision trees in a robust molecular circuit element. In *2022 IEEE International Symposium on Circuits and Systems (ISCAS)*, pages 2229–2232. IEEE, 2022.

[71] Sreetosh Goswami, Rajib Pramanick, Abhijeet Patra, Santi Prasad Rath, Martin Foltin, A Ariando, Damien Thompson, T Venkatesan, Sreebrata Goswami, and R Stanley Williams. Decision trees within a molecular memristor. *Nature*, 597(7874):51–56, 2021.

[72] Tae-Lim Choi, Kwang-Hee Lee, Won-Jae Joo, Sangkyun Lee, Tae-Woo Lee, and Mi Young Chae. Synthesis and nonvolatile memory behavior of redox-active conjugated polymer-containing ferrocene. *Journal of the American Chemical Society*, 129(32):9842–9843, 2007.

[73] Qiongshan Zhang, Qiang Che, Dongchuang Wu, Yunjia Zhao, Yu Chen, Fuzhen Xuan, and Bin Zhang. Dual redox-active covalent organic framework-based memristors for highly-efficient neuromorphic computing. *Angewandte Chemie*, 136(46):e202413311, 2024.

[74] Yingmei Han and Christian A Nijhuis. Functional redox-active molecular tunnel junctions. *Chemistry–An Asian Journal*, 15(22):3752–3770, 2020.

[75] Agostino Migliore and Abraham Nitzan. Nonlinear charge transport in redox molecular junctions: A marcus perspective. *Acs Nano*, 5(8):6669–6685, 2011.

[76] Christian Joachim and Mark A Ratner. Molecular electronics: Some views on transport junctions and beyond. *Proceedings of the National Academy of Sciences*, 102(25):8801–8808, 2005.

[77] Abraham Nitzan. Electron transmission through molecules and molecular interfaces. *Annual review of physical chemistry*, 52(1):681–750, 2001.

[78] Florian Schwarz, Georg Kastlunger, Franziska Lissel, Carolina Egler-Lucas, Sergey N Semenov, Koushik Venkatesan, Heinz Berke, Robert Stadler, and Emanuel Lörtscher. Field-induced conductance switching by charge-state alternation in organometallic single-molecule junctions. *Nature nanotechnology*, 11(2):170–176, 2016.

[79] Lei Dong, Guangwu Li, An-Dih Yu, Zhishan Bo, Cheng-Liang Liu, and Wen-Chang Chen. Conjugated donor-acceptor-acceptor (d-a-a) molecule for organic nonvolatile resistor memory. *Chemistry–An Asian Journal*, 9(12):3403–3407, 2014.

[80] Ye Tao, Dong Li, Ting Hu, Shiwei Qin, Zhongyu Wan, Shaojie Zhang, Kunkun Cao, Yiheng Rao, Guokun Ma, Jun Zhang, et al. Electric field-induced intramolecular charge transfer of two-dimensional covalent organic frameworks with d–a systems for organic memristors. *Journal of Materials Chemistry C*, 13(12):6444–6452, 2025.

[81] Ryan P Sullivan, John T Morningstar, Eduardo Castellanos-Trejo, Robert W Bradford III, Yvonne J Hofstetter, Yana Vaynzof, Mark E Welker, and Oana D Jurchescu. Intermolecular charge transfer enhances the performance of molecular rectifiers. *Science Advances*, 8(31):eabq7224, 2022.

[82] Lu Sun, Xiamin Hao, Qingling Meng, Ligen Wang, Feng Liu, and Miao Zhou. Polaronic resistive switching in ceria-based memory devices. *Advanced Electronic Materials*, 5(10):1900271, 2019.

[83] Yuqi Hou, Xue Zhang, Kepeng Chen, Dongyi Liu, Zhijia Wang, Qingyun Liu, Jianzhang Zhao, and Antonio Barbon. Charge separation, charge recombination, long-lived charge transfer state formation and intersystem crossing in organic electron donor/acceptor dyads. *Journal of Materials Chemistry C*, 7(39):12048–12074, 2019.

[84] James B Derr, Jesse Tamayo, John A Clark, Maryann Morales, Maximillian F Mayther, Eli M Espinoza, Katarzyna Rybicka-Jasińska, and Valentine I Vullev. Multifaceted aspects of charge transfer. *Physical Chemistry Chemical Physics*, 22(38):21583–21629, 2020.

[85] Dongchuang Wu, Qiongshan Zhang, Ning Gu, Yang Cao, Youyi Sun, Bin Zhang, and Yu Chen. Improved resistive switching performance through donor–acceptor structure construction in memristors based on covalent organic framework films. *Journal of Materials Chemistry C*, 11(47):16672–16678, 2023.

[86] Kun-Li Wang, Gang Liu, Po-Hao Chen, Liang Pan, and Hsin-Luen Tsai. Structural effect on controllable resistive memory switching in donor–acceptor polymer systems. *Organic Electronics*, 15(1):322–336, 2014.

[87] Ramachandran Gokul, Ramesh Gayathri, Predhanekar Mohamed Imran, Nattamai SP Bhuvanesh, and Samuthira Nagarajan. Exploring the potential of malononitrile functionalized donor–acceptor systems for non-volatile memory device applications. *Physical Chemistry Chemical Physics*, 27(1):129–137, 2025.

[88] Hamna F Haneef, Andrew M Zeidell, and Oana D Jurchescu. Charge carrier traps in organic semiconductors: a review on the underlying physics and impact on electronic devices. *Journal of Materials Chemistry C*, 8(3):759–787, 2020.

[89] Lei Li. Tunable memristic characteristics based on graphene oxide charge-trap memory. *Micromachines*, 10(2):151, 2019.

[90] Jinyong Wang, Yujing Ren, Ze Yang, Qiaoya Lv, Yu Zhang, Mingyue Zhang, Tiancheng Zhao, Deen Gu, Fucai Liu, Baoshan Tang, et al. Synergistically modulating conductive filaments in ion-based memristors for enhanced analog in-memory computing. *Advanced Science*, 11(22):2309538, 2024.

[91] Monika Ozga, Robert Mroczynski, Krzysztof Matus, Sebastian Arabasz, and Bartłomiej S Witkowski. Filamentary resistive switching mechanism in cuo thin film-based memristor. *Materials*, 18(16):3820, 2025.

[92] Hea-Lim Park, Min-Hwi Kim, Min-Hoi Kim, and Sin-Hyung Lee. Reliable organic memristors for neuromorphic computing by predefining a localized ion-migration path in crosslinkable polymer. *Nanoscale*, 12(44):22502–22510, 2020.

[93] Xiliang Luo, Jianyu Ming, Jincheng Gao, Jingwen Zhuang, Jingwei Fu, Zihan Ren, Haifeng Ling, and Linghai Xie. Low-power flexible organic memristor based on pedot: Pss/pentacene heterojunction for artificial synapse. *Frontiers in Neuroscience*, 16:1016026, 2022.

[94] Viet Cuong Nguyen and Pooi See Lee. Resistive switching memory phenomena in pedot pss: Coexistence of switchable diode effect and write once read many memory. *Scientific Reports*, 6(1):19594, 2016.

[95] Jozef A Helsen and Andrzej Kuczumow. Wavelength-dispersive x-ray fluorescence. In *Handbook of X-ray Spectrometry*, pages 114–217. CRC Press, 2001.

[96] SV Trofymenko. K-shell ionization and characteristic x-ray radiation by high-energy electrons in multifoil targets. *Physical Review A*, 102(6):062804, 2020.

[97] Grzegorz Greczynski and Lars Hultman. X-ray photoelectron spectroscopy: towards reliable binding energy referencing. *Progress in Materials Science*, 107:100591, 2020.

[98] Martin Berger, Qiao Yang, and Andreas Maier. X-ray imaging. *Medical imaging systems: an introductory guide*, pages 119–145, 2018.

[99] Thermo Fisher Scientific. X-ray sources for x-ray photoelectron spectroscopy. `https://www.thermofisher.com/uk/en/home/materials-science/learning-center/surface-analysis/x-ray-generation.html`, 2025. Accessed: 2025-12-08.

[100] Adel Sarolta Racz and Miklos Menyhard. Xps depth profiling of nano-layers by a novel trial-and-error evaluation procedure. *Scientific Reports*, 14(1):18497, 2024.

[101] M Pl Seah and WA Dench. Quantitative electron spectroscopy of surfaces: A standard data base for electron inelastic mean free paths in solids. *Surface and interface analysis*, 1(1):2–11, 1979.

[102] Grzegorz Greczynski and Lars Hultman. A step-by-step guide to perform x-ray photoelectron spectroscopy. *Journal of Applied Physics*, 132(1), 2022.

[103] David Hesp. *Surface characterisation of contact materials for thin film CdTe solar cells*. The University of Liverpool (United Kingdom), 2015.

[104] ED Sosa, R Allada, CB Huffman, and S Arepalli. Xps protocol for the characterization of pristine and functionalized single wall carbon nanotubes. Technical report, 2009.

[105] John C Vickerman and Ian S Gilmore. *Surface analysis: the principal techniques*. John Wiley & Sons, 2011.

[106] Grzegorz Greczynski, Oleksandr Pshyk, and Lars Hultman. Toward an increased reliability of chemical bonding assignment in insulating samples by x-ray photoelectron spectroscopy. *Science advances*, 9(37):eadi3192, 2023.

[107] Thermo Fisher Scientific. Carbon — periodic table (material science learning center). `https://www.thermofisher.com/uk/en/home/`

materials-science/learning-center/periodic-table/non-metal/carbon.html, 2025. Accessed: 2025-12-08.

[108] Thermo Fisher Scientific. Sulfur — element information from thermo fisher materials science learning center. https://www.thermofisher.com/uk/en/home/materials-science/learning-center/periodic-table/non-metal/sulfur.html. Accessed: 2025-12-08.

[109] Johannes Poppenberg, Sebastian Richter, Erik Darlatt, Christoph H-H Traulsen, Hyegeun Min, Wolfgang ES Unger, and Christoph A Schalley. Successive coordination of palladium (ii)-ions and terpyridine-ligands to a pyridyl-terminated self-assembled monolayer on gold. *Surface science*, 606(3-4):367–377, 2012.

[110] Marie-Caroline Bourg, Antonella Badia, and R Bruce Lennox. Gold- sulfur bonding in 2d and 3d self-assembled monolayers: Xps characterization. *The Journal of Physical Chemistry B*, 104(28):6562–6567, 2000.

[111] JE Baio, T Weidner, J Brison, DJ Graham, Lara J Gamble, and David G Castner. Amine terminated sams: Investigating why oxygen is present in these films. *Journal of electron spectroscopy and related phenomena*, 172(1-3):2–8, 2009.

[112] Jan CA Boeyens. The periodic electronegativity table. *Zeitschrift für Naturforschung B*, 63(2):199–209, 2008.

[113] Anders Nilsson. Applications of core level spectroscopy to adsorbates. *Journal of Electron Spectroscopy and Related Phenomena*, 126(1-3):3–42, 2002.

[114] Stephan Hüfner. *Photoelectron spectroscopy: principles and applications*. Springer Science & Business Media, 2013.

[115] Rosa Arrigo, Manfred E Schuster, Zailai Xie, Youngmi Yi, Gregor Wowsnick, Li L Sun, Klaus E Hermann, Matthias Friedrich, Patrick Kast, Michael

Havecker, et al. Nature of the n–pd interaction in nitrogen-doped carbon nanotube catalysts. *Acs Catalysis*, 5(5):2740–2753, 2015.

[116] Troy LR Bennett, Majed Alshammari, Sophie Au-Yong, Ahmad Almutlg, Xintai Wang, Luke A Wilkinson, Tim Albrecht, Samuel P Jarvis, Lesley F Cohen, Ali Ismael, et al. Multi-component self-assembled molecular-electronic films: towards new high-performance thermoelectric systems. *Chemical Science*, 13(18):5176–5185, 2022.

[117] George H Major, Neal Fairley, Peter Sherwood, Matthew R Linford, Jeff Terry, Vincent Fernandez, and Kateryna Artyushkova. Practical guide for curve fitting in x-ray photoelectron spectroscopy. *Journal of Vacuum Science & Technology A*, 38(6), 2020.

[118] Encyclopaedia Britannica, Editors. van der waals forces. `https://www.britannica.com/science/van-der-Waals-forces`, 2025. Accessed: 2025-12-17.

[119] András Pálinkás, György Molnár, Chanyong Hwang, László Péter Biró, and Zoltán Osváth. Determination of the stm tip-graphene repulsive forces by comparative stm and afm measurements on suspended graphene. *RSC Advances*, 6(89):86253–86258, 2016.

[120] John E Lennard-Jones. Cohesion. *Proceedings of the Physical Society*, 43(5):461, 1931.

[121] Xipeng Wang, Simón Ramírez-Hinestrosa, Jure Dobnikar, and Daan Frenkel. The lennard-jones potential: when (not) to use it. *Physical Chemistry Chemical Physics*, 22(19):10624–10633, 2020.

[122] Wenhai Han and F Michael Serry. Force spectroscopy with the atomic force microscope. *Application Note¡ www. agilent. com*, 2011.

[123] Hans-Jürgen Butt, Brunero Cappella, and Michael Kappl. Force measurements with the atomic force microscope: Technique, interpretation and applications. *Surface science reports*, 59(1-6):1–152, 2005.

[124] Mauricio J Giuliodori, Heidi L Lujan, Whitney S Briggs, Gurunanthan Palani, and Stephen E DiCarlo. Hooke's law: applications of a recurring principle. *Advances in physiology education*, 33(4):293–296, 2009.

[125] Karl J Åström and Tore Hägglund. Pid control. *IEEE Control Systems Magazine*, 1066:30–31, 2006.

[126] Peter Eaton and Paul West. *Atomic force microscopy*. Oxford university press, 2010.

[127] Stanford Research Systems. *Lock-In Amplifier Basics*. Application Note.

[128] Ricardo Garcıa and Ruben Perez. Dynamic atomic force microscopy methods. *Surface science reports*, 47(6-8):197–301, 2002.

[129] JP Cleveland, B Anczykowski, AE Schmid, and VB Elings. Energy dissipation in tapping-mode atomic force microscopy. *Applied physics letters*, 72(20):2613–2615, 1998.

[130] Franz J Giessibl. Advances in atomic force microscopy. *Reviews of modern physics*, 75(3):949, 2003.

[131] Nicolás D Smith. A technique for continuous measurement of the quality factor of mechanical oscillators. *Review of Scientific Instruments*, 86(5), 2015.

[132] SB Kaemmer. Application note 133: introduction to bruker's scanasyst and peakforce tapping. *AFM Technol*, 2011.

[133] Bruker Corporation. C-afm principles of operation. Bruker AFM Application Module Theory, 2010.

[134] Bruker Corporation. Tuna principles of operation. Bruker AFM Application Module Theory, 2010.

[135] Andrzej Sikora, Krzysztof Gajewski, Dominik Badura, Bartosz Pruchnik, Tomasz Piasecki, Kamil Raczkowski, and Teodor Gotszalk. Conductive atomic force microscopy—ultralow-current measurement systems for nanoscale imaging of a surface's electrical properties. *Sensors (Basel, Switzerland)*, 24(17):5649, 2024.

[136] Behzad Razavi. The transimpedance amplifier [a circuit for all seasons]. *IEEE Solid-State Circuits Magazine*, 11(1):10–97, 2019.

[137] Xintai Wang, Troy LR Bennett, Ali Ismael, Luke A Wilkinson, Joseph Hamill, Andrew JP White, Iain M Grace, Oleg V Kolosov, Tim Albrecht, Benjamin J Robinson, et al. Scale-up of room-temperature constructive quantum interference from single molecules to self-assembled molecular-electronic films. *Journal of the American Chemical Society*, 142(19):8555–8560, 2020.

[138] Frank P Incropera, David P DeWitt, Theodore L Bergman, Adrienne S Lavine, et al. *Fundamentals of heat and mass transfer*, volume 6. Wiley New York, 1996.

[139] Li Shi and Arunava Majumdar. Thermal transport mechanisms at nanoscale point contacts. *J. Heat Transfer*, 124(2):329–337, 2002.

[140] Pramod Reddy, Sung-Yeon Jang, Rachel A Segalman, and Arun Majumdar. Thermoelectricity in molecular junctions. *Science*, 315(5818):1568–1571, 2007.

[141] ODG. What makes differential op amps vital for modern signal processing. Origin-IC blog, September 02 2025.

[142] Tan Yang, Junjie Lu, and Jeremy Holleman. A high input impedance low-noise instrumentaion amplifier with jfet input. In *2013 IEEE 56th International*

Midwest Symposium on Circuits and Systems (MWSCAS), pages 173–176. IEEE, 2013.

[143] Joseane Santos Almeida, Sergio González Casal, Hassan Al Sabea, Valentin Barth, Gautam Mitra, Vincent Delmas, David Guérin, Olivier Galangau, Tiark Tiwary, Thierry Roisnel, et al. Electronic and thermoelectric properties of molecular junctions incorporating organometallic complexes: Implications for thermoelectric energy conversion. *ACS Applied Nano Materials*, 8(28):14261–14280, 2025.

[144] Stephen Whitelam. Examples of molecular self-assembly at surfaces. *Advanced Materials*, 27(38):5720–5725, 2015.

[145] Harrell Sellers, Abraham Ulman, Yitzhak Shnidman, and James E Eilers. Structure and binding of alkanethiolates on gold and silver surfaces: implications for self-assembled monolayers. *Journal of the American Chemical Society*, 115(21):9389–9401, 1993.

[146] Kevin A Peterlinz and R Georgiadis. In situ kinetics of self-assembly by surface plasmon resonance spectroscopy. *Langmuir*, 12(20):4731–4740, 1996.

[147] Abraham Ulman. Formation and structure of self-assembled monolayers. *Chemical reviews*, 96(4):1533–1554, 1996.

[148] Daniel K Schwartz. Mechanisms and kinetics of self-assembled monolayer formation. *Annual review of physical chemistry*, 52(1):107–137, 2001.

[149] Irving Langmuir. The adsorption of gases on plane surfaces of glass, mica and platinum. *Journal of the American Chemical society*, 40(9):1361–1403, 1918.

[150] Irving Langmuir. Vapor pressures, evaporation, condensation and adsorption. *Journal of the American Chemical Society*, 54(7):2798–2832, 1932.

[151] LibreTexts Chemistry. Langmuir isotherm from a kinetics consideration. `https://chem.libretexts.org/Bookshelves/Physical_and_`

Theoretical_Chemistry_Textbook_Maps/Surface_Science_(Nix)/03:_The_Langmuir_Isotherm/3.03:_Langmuir_Isotherm_from_a_Kinetics_Consideration, 2023.

[152] Md Akhtarul Islam, Myisha Ahmed Chowdhury, Md Salatul Islam Mozumder, and Md Tamez Uddin. Langmuir adsorption kinetics in liquid media: interface reaction model. *ACS omega*, 6(22):14481–14492, 2021.

[153] Colin D Bain, E Barry Troughton, Yu Tai Tao, Joseph Evall, George M Whitesides, and Ralph G Nuzzo. Formation of monolayer films by the spontaneous assembly of organic thiols from solution onto gold. *Journal of the American Chemical Society*, 111(1):321–335, 1989.

[154] Marc D Porter, Thomas B Bright, David L Allara, and Christopher ED Chidsey. Spontaneously organized molecular assemblies. 4. structural characterization of n-alkyl thiol monolayers on gold by optical ellipsometry, infrared spectroscopy, and electrochemistry. *Journal of the American Chemical Society*, 109(12):3559–3568, 1987.

[155] HJ Kim, S Kwak, YS Kim, BI Seo, ER Kim, and H Lee. Adsorption kinetics of alkanethiols studied by quartz crystal microbalance. *Thin Solid Films*, 327:191–194, 1998.

[156] Hun-Gi Hong and Wonchoul Park. A study of adsorption kinetics and thermodynamics of ω-mercaptoalkylhydroquinone self-assembled monolayer on a gold electrode. *Electrochimica acta*, 51(4):579–587, 2005.

[157] Peter Maksymovych, Dan C Sorescu, and John T Yates Jr. Gold-adatom-mediated bonding in self-assembled short-chain alkanethiolate species¡? format?¿ on the au (111) surface. *Physical review letters*, 97(14):146103, 2006.

[158] C Vericat, ME Vela, G Benitez, P Carro, and RC Salvarezza. Self-assembled monolayers of thiols and dithiols on gold: new challenges for a well-known system. *Chemical Society Reviews*, 39(5):1805–1834, 2010.

[159] Sicheon Seong, Jin Wook Han, Gayeong Joo, Hyun Sun Sung, Hong Kyu Park, and Jaegeun Noh. Formation, structure, and thermal annealing effects of ordered self-assembled monolayers of 4-fluorobenzeneselenol on au (111). *Molecules*, 30(9):2057, 2025.

[160] Luke J O'Driscoll and Martin R Bryce. A review of oligo (arylene ethynylene) derivatives in molecular junctions. *Nanoscale*, 13(24):10668–10711, 2021.

[161] Masamitsu Tachibana, Kazunari Yoshizawa, Atsushi Ogawa, Hiroshi Fujimoto, and Roald Hoffmann. Sulfur- gold orbital interactions which determine the structure of alkanethiolate/au (111) self-assembled monolayer systems. *The Journal of Physical Chemistry B*, 106(49):12727–12736, 2002.

[162] MJ Ford, RC Hoft, and JD Gale. Adsorption and dimerisation of thiol molecules on au (111) using a z-matrix approach in density functional theory. *Molecular Simulation*, 32(15):1219–1225, 2006.

[163] Xiang He, Feng Cheng, and Zhao-Xu Chen. The effect of the adsorbate layer on the work function reduction of gold substrates under external electric fields. *Applied Surface Science*, 425:776–780, 2017.

[164] Latha Venkataraman, Jennifer E Klare, Iris W Tam, Colin Nuckolls, Mark S Hybertsen, and Michael L Steigerwald. Single-molecule circuits with well-defined molecular conductance. *Nano letters*, 6(3):458–462, 2006.

[165] ZhongYun Ma, Ferdinand Rissner, LinJun Wang, Georg Heimel, QiKai Li, Zhigang Shuai, and Egbert Zojer. Electronic structure of pyridine-based sams on flat au (111) surfaces: extended charge rearrangements and fermi level pinning. *Physical Chemistry Chemical Physics*, 13(20):9747–9760, 2011.

[166] L Stolberg, S Morin, J Lipkowski, and DE Irish. Adsorption of pyridine at the au (111)-solution interface. *Journal of electroanalytical chemistry and interfacial electrochemistry*, 307(1-2):241–262, 1991.

[167] Wen-Bin Cai, Li-Jun Wan, Hiroyuki Noda, Yuichi Hibino, Kenichi Ataka, and Masatoshi Osawa. Orientational phase transition in a pyridine adlayer on gold (111) in aqueous solution studied by in situ infrared spectroscopy and scanning tunneling microscopy. *Langmuir*, 14(24):6992–6998, 1998.

[168] Adam P Hinckley and Anthony J Muscat. Detecting and removing defects in organosilane self-assembled monolayers. *Langmuir*, 36(10):2563–2573, 2020.

[169] Celso I Fornari, Gabriel Fornari, PH Rappl, Eduardo Abramof, and JDS Travelho. Monte carlo simulation of epitaxial growth. *Epitaxy; Zhong, M., Ed.; BoD–Books on Demand: Norderstedt, Germany*, page 113, 2018.

[170] Ali Ismael, Alaa Al-Jobory, Xintai Wang, Abdullah Alshehab, Ahmad Almutlg, Majed Alshammari, Iain Grace, Troy LR Benett, Luke A Wilkinson, Benjamin J Robinson, et al. Molecular-scale thermoelectricity: as simple as 'abc'. *Nanoscale Advances*, 2(11):5329–5334, 2020.

[171] Emily A Weiss, George K Kaufman, Jennah K Kriebel, Zhefeng Li, Richard Schalek, and George M Whitesides. Si/sio2-templated formation of ultraflat metal surfaces on glass, polymer, and solder supports: Their use as substrates for self-assembled monolayers. *Langmuir*, 23(19):9686–9694, 2007.

[172] Mark C Biesinger. Accessing the robustness of adventitious carbon for charge referencing (correction) purposes in xps analysis: Insights from a multi-user facility data review. *Applied Surface Science*, 597:153681, 2022.

[173] Thermo Fisher Scientific. Carbon XPS binding energies. `https://www.thermofisher.com/uk/en/home/materials-science/learning-center/periodic-table/non-metal/carbon.html`.

[174] Mattia Scardamaglia and Carla Bittencourt. Metal-free catalysis based on nitrogen-doped carbon nanomaterials: a photoelectron spectroscopy point of view. *Beilstein Journal of Nanotechnology*, 9(1):2015–2031, 2018.

[175] Krzysztof K Zborowski and Jordi Poater. Pyrrole and pyridine in the water environment—effect of discrete and continuum solvation models. *ACS omega*, 6(38):24693–24699, 2021.

[176] Kateryna Artyushkova. Misconceptions in interpretation of nitrogen chemistry from x-ray photoelectron spectra. *Journal of Vacuum Science & Technology A*, 38(3), 2020.

[177] Ivana Matanovic, Kateryna Artyushkova, Matthew B Strand, Michael J Dzara, Svitlana Pylypenko, and Plamen Atanassov. Core level shifts of hydrogenated pyridinic and pyrrolic nitrogen in the nitrogen-containing graphene-based electrocatalysts: in-plane vs edge defects. *The Journal of Physical Chemistry C*, 120(51):29225–29232, 2016.

[178] Fahrettin Yakuphanoglu, Salih Okur, and Hüseyin Özgener. Modification of metal/semiconductor junctions by self-assembled monolayer organic films. *Microelectronic engineering*, 86(11):2358–2363, 2009.

[179] Alessandro Rospigliosi, Rudolf Ehlich, Heinrich Hoerber, Anton Middelberg, and Geoff Moggridge. Electron transfer of plurimodified dna sams. *Langmuir*, 23(15):8264–8271, 2007.

[180] Edmund Leary, Bart Limburg, Asma Alanazy, Sara Sangtarash, Iain Grace, Katsutoshi Swada, Louisa J Esdaile, Mohammed Noori, M Teresa González, Gabino Rubio-Bollinger, et al. Bias-driven conductance increase with length in porphyrin tapes. *Journal of the American Chemical Society*, 140(40):12877–12883, 2018.

[181] Edmund Leary, Georg Kastlunger, Bart Limburg, Laura Rincón-García, Juan Hurtado-Gallego, M Teresa González, Gabino Rubio Bollinger, Nicolás Agrait, Simon J Higgins, Harry L Anderson, et al. Long-lived charged states of single porphyrin-tape junctions under ambient conditions. *Nanoscale Horizons*, 6(1):49–58, 2021.

[182] Jie-Ren Deng, M Teresa González, He Zhu, Harry L Anderson, and Edmund Leary. Ballistic conductance through porphyrin nanoribbons. *Journal of the American Chemical Society*, 146(6):3651–3659, 2024.

[183] Takayuki Tanaka and Atsuhiro Osuka. Conjugated porphyrin arrays: synthesis, properties and applications for functional materials. *Chemical Society Reviews*, 44(4):943–969, 2015.

[184] Xinkai Qiu, Jie-Ren Deng, G Andrew D Briggs, Harry L Anderson, and James O Thomas. Two-terminal analog memory comprising self-assembled monolayers of edge-fused porphyrin oligomers. *Nanoscale*, 17(38):22315–22321, 2025.

[185] Ryan C Chiechi, Emily A Weiss, Michael D Dickey, and George M Whitesides. Eutectic gallium–indium (egain): a moldable liquid metal for electrical characterization of self-assembled monolayers. *Angewandte Chemie International Edition*, 47(1):142–144, 2008.

[186] Ludovico Cademartiri, Martin M Thuo, Christian A Nijhuis, William F Reus, Simon Tricard, Jabulani R Barber, Rana NS Sodhi, Peter Brodersen, Choongik Kim, Ryan C Chiechi, et al. Electrical resistance of agts–s (ch2) n-1ch3//ga2o3/egain tunneling junctions. *The Journal of Physical Chemistry C*, 116(20):10848–10860, 2012.

[187] Felice C Simeone, Hyo Jae Yoon, Martin M Thuo, Jabulani R Barber, Barbara Smith, and George M Whitesides. Defining the value of injection current and effective electrical contact area for egain-based molecular tunneling junctions. *Journal of the American Chemical Society*, 135(48):18131–18144, 2013.

[188] DH Karweik and N Winograd. Nitrogen charge distributions in free-base porphyrins, metalloporphyrins, and their reduced analogs observed by x-ray photoelectron spectroscopy. *Inorganic Chemistry*, 15(10):2336–2342, 1976.

[189] Guohu Zhang, Ahmed FM El-Mahdy, Lamiaa Reda Ahmed, Babasaheb M Matsagar, Sameerah Al-Saeedi, Shiao-Wei Kuo, and Kevin C-W Wu. Metal complexes of the porphyrin-functionalized polybenzoxazine. *Polymers*, 14(3):449, 2022.

[190] David M Sarno, Luis J Matienzo, and Wayne E Jones. X-ray photoelectron spectroscopy as a probe of intermolecular interactions in porphyrin polymer thin films. *Inorganic chemistry*, 40(24):6308–6315, 2001.

[191] Codruța Varodi, Florina Pogăcean, Alexandra Cioriță, Ovidiu Pană, Cristian Leoștean, Bogdan Cozar, Teodora Radu, Maria Coroș, Raluca Ioana Ștefan-van Staden, and Stela-Maria Pruneanu. Nitrogen and sulfur co-doped graphene as efficient electrode material for l-cysteine detection. *Chemosensors*, 9(6):146, 2021.

[192] Mary M Walczak, Carla A Alves, Brian D Lamp, and Marc D Porter. Electrochemical and x-ray photoelectron spectroscopic evidence for differences in the binding sites of alkanethiolate monolayers chemisorbed at gold. *Journal of Electroanalytical Chemistry*, 396(1-2):103–114, 1995.

[193] Christina DM Trang, Carlos Mora Perez, Jingyi Ran, Oleg V Prezhdo, and Michael S Inkpen. Counterion loss from charged surface-bound complexes drives the formation of loosely packed monolayers. *Journal of the American Chemical Society*, 146(37):25625–25639, 2024.

[194] Chenyang Guo, Philip Benzie, Shu Hu, Bart de Nijs, Ermanno Miele, Eoin Elliott, Rakesh Arul, Helen Benjamin, Grzegorz Dziechciarczyk, Reshma R Rao, et al. Extensive photochemical restructuring of molecule-metal surfaces under room light. *Nature Communications*, 15(1):1928, 2024.

[195] Bingxin Li, Shanglong Ning, Chunyang Miao, Chenyang Guo, Gyu Don Kong, Xintai Wang, Victor I Coldea, Yuqiao Li, Sam Harley, Oleg V Kolosov, et al. Migration of gold atoms into a thiol-bonded molecular self-assembled

monolayer, forming a cluster exhibiting a coulomb staircase. *arXiv preprint arXiv:2512.18931*, 2025.

[196] Chuan-Jian Zhong, Robert C Brush, Jim Anderegg, and Marc D Porter. Organosulfur monolayers at gold surfaces: Reexamination of the case for sulfide adsorption and implications to the formation of monolayers from thiols and disulfides. *Langmuir*, 15(2):518–525, 1999.

[197] Duane E Weisshaar, Mary M Walczak, and Marc D Porter. Electrochemically induced transformations of monolayers formed by self-assembly of mercaptoethanol at gold. *Langmuir*, 9(1):323–329, 1993.

[198] AN Buckley, IC Hamilton, and R Woods. An investigation of the sulphur (- ii)/sulphur (0) system on bold electrodes. *Journal of electroanalytical chemistry and interfacial electrochemistry*, 216(1-2):213–227, 1987.

[199] DR Mullins and PF Lyman. Interaction of methanethiol with sulfur-covered w (001). *Langmuir*, 12(26):6382–6388, 1996.

[200] Brian D Lamp, Daisuke Hobara, Marc D Porter, Katsumi Niki, and Therese M Cotton. Correlation of the structural decomposition and performance of pyridinethiolate surface modifiers at gold electrodes for the facilitation of cytochrome c heterogeneous electron-transfer reactions. *Langmuir*, 13(4):736–741, 1997.

[201] Takao Ishida, Masahiko Hara, Isao Kojima, Satoshi Tsuneda, Naoki Nishida, Hiroyuki Sasabe, and Wolfgang Knoll. High resolution x-ray photoelectron spectroscopy measurements of octadecanethiol self-assembled monolayers on au (111). *Langmuir*, 14(8):2092–2096, 1998.

[202] Robert McHardy, Wolfgang H Haiss, and Richard J Nichols. An stm investigation of surface diffusion on iodine modified au (111). *Physical Chemistry Chemical Physics*, 2(7):1439–1444, 2000.

[203] Young-Jun Yu, Yue Zhao, Sunmin Ryu, Louis E Brus, Kwang S Kim, and Philip Kim. Tuning the graphene work function by electric field effect. *Nano letters*, 9(10):3430–3434, 2009.

[204] Denis Scaini, Fabio Biscarini, Loredana Casalis, and Cristiano Albonetti. Substrate roughness influence on the order of nanografted self-assembled monolayers. *Chemical Physics Letters*, 803:139819, 2022.

[205] Gorachand Dutta, Flavio CB Fernandes, Pedro Estrela, Despina Moschou, and Paulo R Bueno. Impact of surface roughness on the self-assembling of molecular films onto gold electrodes for label-free biosensing applications. *Electrochimica Acta*, 378:138137, 2021.

[206] Supriyo Datta. Exclusion principle and the landauer-büttiker formalism. *Physical Review B*, 45(3):1347, 1992.

[207] Alessio Orbelli Biroli, Alberto Calloni, Alberto Bossi, Madan S Jagadeesh, Guglielmo Albani, Lamberto Duò, Franco Ciccacci, Andrea Goldoni, Alberto Verdini, Luca Schio, et al. Out-of-plane metal coordination for a true solvent-free building with molecular bricks: Dodging the surface ligand effect for on-surface vacuum self-assembly. *Advanced Functional Materials*, 31(20):2011008, 2021.

[208] Aicheng Chen, Zhichao Shi, Dan Bizzotto, Jacek Lipkowski, Bruno Pettinger, and Christoph Bilger. Iodide adsorption at the au (111) electrode surface. *Journal of Electroanalytical Chemistry*, 467(1-2):342–353, 1999.

[209] Sareh Ahmadi, M Nina Shariati, Shun Yu, and Mats Göthelid. Molecular layers of znpc and fepc on au (111) surface: Charge transfer and chemical interaction. *The Journal of Chemical Physics*, 137(8), 2012.

[210] H Yamane, A Gerlach, S Duhm, Y Tanaka, T Hosokai, YY Mi, J Zegenhagen, N Koch, K Seki, and F Schreiber. Site-specific geometric and electronic

relaxations at organic-metal interfaces. *Physical review letters*, 105(4):046103, 2010.

[211] F Petraki, H Peisert, I Biswas, and T Chassé. Electronic structure of cophthalocyanine on gold investigated by photoexcited electron spectroscopies: indication of co ion- metal interaction. *The Journal of Physical Chemistry C*, 114(41):17638–17643, 2010.